

Studies of Physical Properties in Doped Perovskite Based Ruthenates

A thesis submitted to Jawaharlal Nehru University

for the degree of

Doctor of Philosophy

In Physics

by

Renu Gupta

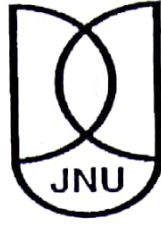


School of Physical Sciences

Jawaharlal Nehru University

New Delhi-110067, India

July 2018



भौतिक विज्ञान संस्थान
SCHOOL OF PHYSICAL SCIENCES
जवाहरलाल नेहरू विश्वविद्यालय
JAWAHARLAL NEHRU UNIVERSITY
नई दिल्ली-110067, भारत
New Delhi-110067, INDIA

Declaration

I hereby declare that the work in this thesis entitled “**Studies of Physical Properties in Doped Perovskite Based Ruthenates**” is entirely original and has been carried out by me in the School of Physical Sciences, Jawaharlal Nehru University, New Delhi-110067 under the supervision of Dr. Ashim Kr. Pramanik. I further declare that it has not formed the basis for the award of any degree, diploma, associateship or similar title of any university or institution.

July 2018

Renu Gupta
Renu Gupta

Certificate

We recommend that this thesis be placed before the examiners for evaluation.

Dr. Ashim Kr. Pramanik

Thesis Supervisor

Prof. S. Patnaik

Dean
School of Physical Sciences

Dedicated

to

my family...

Acknowledgments

It is my pleasure and duty to thank all who have shared their time and helped throughout my doctoral study. First I would like to express my deep and sincere gratitude to my supervisor Dr. Ashim Kumar Pramanik for giving me a great opportunity and for his continuous support, guidance, encouragement, and motivation. There are no words to thank him for the patience he has shown on my frequently made mistakes and giving a chance to the rich learning experience. It would not have been possible to complete my doctoral work without his vast knowledge and innovative ideas. He inspired me through his continuous efforts, enthusiasm and dedication to research. I am greatly benefited from his ready and easy accessibility and willingness to help. I am very much grateful to him for letting me think independently and implemented the ideas.

I would like to express my special gratitude to my seniors Dr. Jitendra Saha, Dr. Vishal Maurya, Dr. Gyaneshwar, Dr. Arun Singh, Dr. Avesh Kumar and Dr. Shruti to enlighten me the basic concept of experiment and theory, essential for my research. I would like to deliver my sincere thanks to Dr. Brijesh Kumar who taught me Advanced Condense Matter Physics. I am very thankful to the faculty at the School of Physical Sciences (SPS), Jawaharlal Nehru University and Inter University Accelerator Centre (IUAC), New Delhi for their teachings during course work. I am also thankful to SPS JNU for providing room temperature XRD and other instrumentation facilities. I also thanks to SPS faculty for their direct or indirect help. I would like to acknowledge Advance Instrumentation Research Facility (AIRF), JNU and their staff members Prabhat Sir and Saroj Sir for magnetization data.

I also express my thanks to all the Scientists and Engineers of the UGC-DAE Consortium for Scientific Research Institute; especially Dr. Alok Banerjee, Dr. R. Rawat, Mr. Kranti Kumar and Mr. Sachin Kumar; for continuous support

during magnetization and transport measurements. I also want to say thanks to UGC DAE for accommodation and travel support.

It is my privilege to thank Dr. Pintu Das (IIT Delhi) for providing magnetization measurement facility and Mr. Shajid (IIT Delhi) who helped in measurements and data collection. I am also thankful to IUAC New Delhi, India for facilitating the furnace for preparing the samples, especially thanks to Dr. Ashokan. It gives me a great pleasure to thank Sachin, Vikram, Saroj, Pampi, Swati, and Vikash for their help and accompany throughout my stay at UGC DAE Indore. It has been my pleasure to work with a team with such a pleasant atmosphere.

I am grateful to the Jawaharlal Nehru University, New Delhi, University Grants Commission, and Department of Science and Technology, India for financial support through non-NET fellowship, Basic Scientific Research (BSR) fellowship, and travel grant support, respectively.

I also thank all my teachers for their efforts to cultivate knowledge and passion in me. Without their perhaps, I would not have reached here. Especially Prof. Chirantan Neogi, University of Kalyani, for introducing about the research and encouraged me to take my step forward. I extend my thanks to Mr. Imtiaz Noor Bhatti for his advice, fruitful discussions and moral support. I would like to thank my other lab members Mr. Harish, Mr. Kishor, Miss. Rachna, Miss. Shobha and Mr. Kamlesh who help me which have possible.

I wish to acknowledge all the non-teaching staff of SPS for their help and assistance in the official work and Santosh bhaiya (Canteen). I would like to express special thanks to my friend Pramod Kumar Gupta for his company and supportive nature, cooperation in my whole Ph.D. duration and also moral support. It would have been hard to complete this journey without his help and cooperation. I also want to express special gratitude to my batchmates Jyoti, Prataya, Panchram, Rohatas, Ramesh, Avanish for their help. I also want to say thanks SPS member for their support and enjoyable moments which we shared together.

Last but not the least; I would like to express my deepest gratitude to my family. I am especially thankful to my father and mother for their unconditional love and blessings that made me stand strong in all circumstances. They gave

me the freedom to choose my future and never ceased to believe in me. I express my gratitude to my brothers, sisters "Mahesh", "Pooja", "Suresh", "Khushboo" and "Ganesh" for their boundless support and love. Eventually, thanks to my friends for all kinds of encouragement, constant love, care and support.

Abstract

The intermediate nature of electron correlation (U) and spin orbit coupling (SOC) makes $4d$ based transition metal oxides (TMOs) an attractive research topic. Ruthenates are of special interest among $4d$ based TMOs where these materials increasing interest with the discovery of superconductivity (SC) of unusual spin triplet in layered Sr_2RuO_4 . The perovskites based SrRuO_3 has been extensively studied in last few decades for its interesting magnetic and electron transport properties, while $4d$ based TM alloys (ZrZn_2 , LaCoAsO) have shown ferromagnetic (FM) behavior but SrRuO_3 is only material among $4d$ based oxides, which shows itinerant type FM with T_c around 160 K. This experimental determines that magnetic moment comes lower than the expected value which constitutes a signature of itinerant FM of SrRuO_3 . SrRuO_3 material further shows metallic behavior through till very high temperature (1000 K). The studies have shown an interrelation between magnetic and transport behavior in SrRuO_3 . A good electronic correlation in SrRuO_3 has been evidenced in experimental measurements such as x-ray photoemission spectroscopy (XPS), and also this material shows Fermi liquid (FL) type behavior at low temperature. In spite of large volume of both experimental and theoretical studies, detail nature of magnetic and transport properties and their correlation is not fully understood, so SrRuO_3 continues to attract scientific attention.

In present thesis work, we have studied the magnetic and electronic transport behavior in SrRuO_3 after inducing nonmagnetic elements at Ru-site, we have used Ti^{4+} ($3d^0$) and Ga^{3+} ($3d^0$) as nonmagnetic doping where the matching ionic radii Ti^{4+} (0.605\AA) and Ga^{3+} (0.62\AA) with Ru^{4+} (0.62\AA) will give minimum structural modification in SrRuO_3 . While both the elements dilute the magnetism and lattice and tune the electronic properties but Ga^{3+} will additionally change the Ru^{4+} charge state accordingly. Further U and density of states (DOS) will modify through both the doping. Hence the stoner criteria for itinerant FM in SrRuO_3 will be influenced by both the doping. The recent study on thin film shows the variation of T_c by the change in DOS.

In Chapter 1, we have given a general introduction of TMOs, ruthenates and the physical phenomenon associated with TMOs and SrRuO₃. We also discuss the objective of the present thesis.

In Chapter 2, the sample preparation and characterization technique along with other experimental technique adopting in the present thesis have been discussed.

Chapter 3 focuses on structural and magnetic properties in SrRu_{1-x}Ti_xO₃ series. We have discussed the sample preparation and characterization techniques of SrRu_{1-x}Ti_xO₃ series and shown the structure evolution of structure parameters with Ti substitution. The evolution of magnetic properties with Ti substitution has been studied through low-temperature demagnetization, critical exponent behavior, Griffiths phase, Curie-Weiss behavior and isothermal magnetization. We obtain that the magnetization decreased up to 70% of Ti doping though the FM-PM transition temperature (T_c) does not affect. The critical exponent close to T_c shows mean field ($\beta = 1/2$) type nature and β increases by Ti doping. The low-temperature demagnetization shows the combined effect of itinerant and localizes nature.

In Chapter 4, we have discussed the critical analysis of SrRu_{1-x}Ti_xO₃ series to understand the nature of unchanged T_c and increasing order of critical exponent (β) by Ti doping, we aim to evaluate the critical behavior study close to phase transition via following technique like modified Arrott plot, Kouvel-Fisher plot and critical isothermal analysis. Surprisingly, the critical study also shows that T_c does not change with Ti doping. However, β connected with spontaneous magnetization (M_s) increases although the other critical exponent γ and δ related to initial inverse susceptibility (χ_0^{-1}) and critical magnetization, respectively decreases by Ti doping. However, these estimated exponents do not match with any established theoretical models of universality classes, apart from this the exponent further obey the Widom relation and the scaling behavior. Interestingly, this particular evolution of exponents of present series has similarity with that in isoelectronic doped Sr_{1-x}Ca_xRuO₃. Our understanding is that site dilution by Ti leads to formation magnetic clusters which causes this specific changes in critical exponents and Ti⁴⁺ ($3d^0$) for Ru⁴⁺ ($4d^4$) would simply dilute the magnetic system apart from modifying the electron correlation effect and the density of states (DOS) at Fermi level.

In Chapter 5 we study the effect of site dilution as well as charge disorder effect in SrRuO_3 , has been chosen to dope at Ru^{4+} site by Ga^{3+} . In this Ga^{3+} also have similar ionic radii to Ru^{4+} so it would not effect on structure, but it modifies the Ru charge state from Ru^{4+} to Ru^{5+} unlike for Ti substitution. The Ga^{3+} substitution does not affect the original orthorhombic- $Pbnm$ structure of SrRuO_3 , but the lattice parameters show a decrease due to smaller ionic radii of generated Ru^{5+} . In this, we report the evolution of structural, magnetic and transport behavior of $\text{SrRu}_{1-x}\text{Ga}_x\text{O}_3$ series ($x \leq 0.2$). The Ga^{3+} has substantial effect on the magnetic behavior including the magnetic moment and magnetic phase transition similar to Ti doping. The SrRuO_3 shows metallic behavior throughout the temperature range and by Ga^{3+} substitution induces an insulating behavior. We have done detail analysis of charge transport mechanism in present series in whole temperature range across the magnetic transition temperature (T_c).

In Chapter 6, we discuss transport behavior in terms of electrical resistivity (presence of zero field and in field) and specific heat study in $\text{SrRu}_{1-x}\text{Ti}_x\text{O}_3$ series ($x \leq 0.7$). The Ti^{4+} substitution is expected to change the electron correlation effect and DOS. The transport behavior has studied in terms of Fermi liquid, non-Fermi liquid, Kondo and modified Mott variable range hopping (VRH) in absence and presence of magnetic field. The specific heat (C_p) study shows an anomalous behavior across the magnetic transition temperature. Further, the correlations between the electrical charge transport and the DOS have been observed through the strong correlation effect at low temperature.

Publications

01. Journal Papers

1. **R. Gupta**, A.K. Pramanik, Site dilution in SrRuO₃: effects on structural and magnetic properties, *J. Phys. Condens. Matter.* 29 (2017) 115801.
2. **R. Gupta**, I.N. Bhatti, A.K. Pramanik, Critical behavior in itinerant ferromagnet SrRu_{1-x}Ti_xO₃, *J. Magn. Magn. Mater.* 465 (2018) 193–200.
3. **R. Gupta**, A.K. Pramanik, Effects of Site dilution and Ru-charge modulation on physical properties in SrRu_{1-x}Ga_xO₃. [in preparation]
4. **R. Gupta**, A.K. Pramanik, Site dilution effect on Electrical Transport Behavior in SrRu_{1-x}Ti_xO₃. [in preparation]

02. Conference Proceedings

1. **R. Gupta**, A.K. Pramanik, Effect of Y substitution in SrRuO₃: Evolution from itinerant to localized type magnetism, *AIP Conf. Proc.* 1832 (2017) 130036.
2. **R. Gupta**, A.K. Pramanik, Electronic and magnetic properties in Sr_{1-x}La_xRuO₃, *AIP Conf. Proc.* 1731 (2016) 130055.
3. **R. Gupta**, A.K. Pramanik, Evolution of structural, magnetic and transport behavior by Pr doping in SrRuO₃, *AIP Conf. Proc.* 1953 (2018) 40006.
4. **R. Gupta**, A.K. Pramanik, Investigation of structural and magnetic properties of SrRuO₃ by Ir doping at Ru site. [Accepted in *AIP Conf. Proc.*]

List of figures

1.1 Periodic table shows d block transition metal elements.	2
1.2 Ruddlesden-Popper series of $\text{Sr}_{n+1}\text{Ru}_n\text{O}_{3n+1}$ with varying n .	3
1.3 Schematic view of anisotropic shape of d orbitals.	4
1.4 The schematic diagram of crystal field splitting.	5
1.5 The two spin sub band of spin up and down spin (a) before splitting and (b) after splitting.	8
1.6 shows schematic diagram of Griffiths phase (GP) of theoretical explanation.	12
1.7 shows a schematic diagram of the Griffiths phase	13
1.8 The site dilution effects by Ti substitution in SrRuO_3 which dilute the Ru-O-Ru chain.	17
2.1 Stepwise procedures to synthesis SrRuO_3 using Solis State Reaction (SSR) method.	23
2.2 Schematic of XRD diffractometer (a), and Bragg's law to determine the interplaner separation (b).	25
2.3 Schematic of Physical Properties Measurement System (PPMS).	29
2.4 Schematic of Superconducting Quantum Interference Device (SQUID).	30
2.5 Schematic diagram of four probe configuration of sample.	31

3.1 Room temperature XRD pattern of $\text{SrRu}_{1-x}\text{Ti}_x\text{O}_3$ series.	40
3.2. The room temperature XRD pattern along with Rietveld refinement taking orthorhombic- $Pbnm$ structure has been shown for (a) SrRuO_3 and (b) $\text{SrRu}_{0.3}\text{Ti}_{0.7}\text{O}_3$. Inset in (b) shows χ^2 value of Rietveld fitting for $\text{SrRu}_{1-x}\text{Ti}_x\text{O}_3$ series with rhombohedral (R), cubic (C), tetragonal (T) and orthorhombic (O) structure.	41
3.3 Unit cell parameters (a) a , (b) b , (c) c and (d) volume V as determined from Rietveld analysis using room temperature XRD data have been shown with Ti concentration (x) for $\text{SrRu}_{1-x}\text{Ti}_x\text{O}_3$. Lines are guide to eyes.	43
3.4 Temperature dependent magnetization data measured in 100 Oe following ZFC and FC protocol have been shown for $\text{SrRu}_{1-x}\text{Ti}_x\text{O}_3$ series with (a) $x = 0.0, 0.1, 0.2, 0.3$ and (b) $x = 0.4, 0.5, 0.7$. Insets show the zero field cooled magnetization data in expanded scale close to T_c .	45
3.5 Spin-wave stiffness constant D as a function of Ti doping concentration. Inset shows fitting of magnetization data using Eq. (3.1) and (3.4).	47
3.6 The evolution of critical exponent β (Eq. 3.5) with x has been shown for $\text{SrRu}_{1-x}\text{Ti}_x\text{O}_3$ series. Inset shows field cooled magnetization data along with fitting due to Eq. (3.5).	49
3.7 (a) Shows temperature dependence of inverse magnetic susceptibility for $\text{SrRu}_{1-x}\text{Ti}_x\text{O}_3$ series with $x = 0.0, 0.3, 0.4, 0.5$ and 0.7 . (b) Inverse susceptibility has been plotted following Eq. (3.6) on $\log_{10} - \log_{10}$ scale with $x = 0.4, 0.5$ and 0.7 . (c) Shows inverse susceptibility for $x = 0.5$ sample in different magnetic fields. (d) Shows same plotting as in (b) for $x = 0.5$ sample with different magnetic fields. The straight lines in (b) and (d) are due to fitting with Eq. (3.6).	52

3.8 (a) The calculated and experimentally determined effective PM moment μ_{eff} have shown with x . Inset shows temperature dependent inverse susceptibility for SrRuO_3 and the straight line is fitting due to Eq. (3.7), (b) shows Curie temperature θ_p against Ti concentration (Eq. 3.7).	54
3.9 The isothermal magnetization data with field at 5 K are shown for $\text{SrRu}_{1-x}\text{Ti}_x\text{O}_3$ series. Inset shows value of moment at 70 kOe obtained from main panel with x .	56
3.10 The $M(H)$ data plotted in form of M^2 vs H/M (Arrott plot) for $\text{SrRu}_{1-x}\text{Ti}_x\text{O}_3$ series. Inset shows spontaneous moment M_s as obtained from Arrott plot with Ti concentration.	57
3.11 Resistivity as a function of temperature have been shown with (a) $x = 0.0, 0.1, 0.2, 0.3, 0.4$ and (b) 0.5 and 0.7 for $\text{SrRu}_{1-x}\text{Ti}_x\text{O}_3$ series.	59
4.1 Temperature dependent field cooled magnetization data measured in presence of 100 Oe applied field have been shown for $\text{SrRu}_{1-x}\text{Ti}_x\text{O}_3$ series. The inset shows zero field cooled magnetization (100 Oe) in expanded temperature range close to T_c .	71
4.2 Field dependent isothermal magnetization data near to the transition temperature $\sim T_c$ are shown for $\text{SrRu}_{1-x}\text{Ti}_x\text{O}_3$ series with (a) $x = 0.0$ (b) $x = 0.1$ (c) $x = 0.3$ (d) $x = 0.4$ (e) $x = 0.5$ and (f) $x = 0.7$ composition. Inset of each figure shows magnetic-field derivative of magnetization (dM/dH) as a function of magnetic field for $M(H)$ plots taken at T_c for respective sample.	73
4.3 Isotherms in Figure 4.2 are plotted in form of Arrott plot (M^2 vs H/M) for $\text{SrRu}_{1-x}\text{Ti}_x\text{O}_3$ series with (a) $x = 0.0$ (b) $x = 0.1$ (c) $x = 0.3$ (d) $x = 0.4$ (e) $x = 0.5$ and (f) $x = 0.7$.	74
4.4 Modified Arrott plot, $M^{1/\beta}$ vs $(H/M)^{1/\gamma}$, constructed out of $M(H)$ data in Figure 4.2 are shown for $\text{SrRu}_{1-x}\text{Ti}_x\text{O}_3$ series with (a) $x = 0.0$ (b) $x = 0.1$ (c) $x = 0.3$ (d) $x = 0.4$ (e) $x = 0.5$ and (f) $x = 0.7$. The solid	76

red line in each figure is due to straight line fitting of modified Arrott plot related to isotherm which passes through origin.

4.5 Temperature dependent spontaneous magnetization M_s (left axis) and initial inverse susceptibility $\chi_0^{-1}(T)$ (right axis) as estimated from modified Arrott plots in Figure 4.4 are shown for $\text{SrRu}_{1-x}\text{Ti}_x\text{O}_3$ series with (a) $x = 0.0$ (b) $x = 0.1$ (c) $x = 0.3$ (d) $x = 0.4$ (e) $x = 0.5$ and (f) $x = 0.7$. The solid red lines are due to fitting with power law behavior as stated in Eq. (4.1) and Eq. (4.2). 78

4.6 Kouvel-Fisher plots for spontaneous magnetization (Eq. 4.6) on left axis and for initial inverse susceptibility (Eq. 4.7) on right have been shown for $\text{SrRu}_{1-x}\text{Ti}_x\text{O}_3$ series with (a) $x = 0.0$ (b) $x = 0.1$ (c) $x = 0.3$ (d) $x = 0.4$ (e) $x = 0.5$ and (f) $x = 0.7$. The solid straight lines are the linear fits following Eq. 4.6 and 4.7. 80

4.7 The $M(H)$ isotherm at T_c has been shown for $\text{SrRu}_{1-x}\text{Ti}_x\text{O}_3$ series with (a) $x = 0.0$ (b) $x = 0.1$ (c) $x = 0.3$ (d) $x = 0.4$ (e) $x = 0.5$ and (f) $x = 0.7$. The inset shows same $M(H)$ data in \log_{10} - \log_{10} scale for respective samples and the solid line is due to linear fit of the data. 82

4.8 Renormalized magnetization $M|t|^{-\beta}$ has been plotted as a function of renormalized field $H|t|^{-(\gamma+\beta)}$ for isotherms both below and above T_c . Data are shown for $\text{SrRu}_{1-x}\text{Ti}_x\text{O}_3$ series with (a) $x = 0.0$ (b) $x = 0.1$ (c) $x = 0.3$ (d) $x = 0.4$ (e) $x = 0.5$ and (f) $x = 0.7$. Inset shows same plot in \log_{10} - \log_{10} scale. Renormalized magnetization is merged into single line with renormalized field for isotherms both below and above T_c . 84

4.9 The critical exponents scaled by its values for $x = 0.0$ compound are shown as a function of composition (x) for $\text{SrRu}_{1-x}\text{Ti}_x\text{O}_3$ series. 86

5.1 (a) The room temperature powder XRD patterns of polycrystalline samples of $\text{SrRu}_{1-x}\text{Ga}_x\text{O}_3$ series with compositions of $x = 0.0, 0.05, 0.1$ and 0.2 (b) The XRD pattern along with Rietveld refinement analysis of $\text{SrRu}_{0.8}\text{Ga}_{0.2}\text{O}_3$ with orthorhombic $Pbnm$ structure at room temperature. 95

<p>5.2 (a) The temperature dependent dc magnetization from 5 K to 300 K in the form of M_{ZFC} and M_{FC} protocol at 100 Oe of magnetic field as function of temperature of $SrRu_{1-x}Ga_xO_3$ series with compositions $x = 0.0, 0.05, 0.1$ and 0.2. The inset shows M_{ZFC} highest peak close to T_c</p> <p>(b) The inverse susceptibility ($\chi^{-1} = H/M$) plot with modified Curie-Weiss Law fitting in the temperature range of 200 K to 300 K of $SrRu_{1-x}Ga_xO_3$ series, the solid line is linear fitting. In inset, left axis shows the Curie temperature (θ_p) variation by Ga doping of $SrRu_{1-x}Ga_xO_3$ series and right axis shows effective PM moment variation by Ga doping of $SrRu_{1-x}Ga_xO_3$ series.</p>	<p>96</p>
<p>5.3 The spin-wave and single particle combined fitting of $SrRuO_3$ and upper inset shows only spin wave fitting while lower inset shows only single particle fitting of $SrRuO_3$.</p>	<p>100</p>
<p>5.4 The critical exponent (β) fitting close to T_c of $SrRu_{1-x}Ga_xO_3$ series and the inset shows variation of β by Ga doping of $SrRu_{1-x}Ga_xO_3$ series.</p>	<p>103</p>
<p>5.5 (a) The χ^{-1} with the variation of temperature of $SrRu_{1-x}Ga_xO_3$ series in PM state close to phase transition (b) The $\log_{10} - \log_{10}$ scale fitting of equation (5.9) of $SrRu_{1-x}Ga_xO_3$ series with $x = 0.1$ and 0.2. This plot of $x = 0.2$ samples has shifted upward by +1 for clarity.</p>	<p>104</p>
<p>5.6 (a) The magnetic field dependent iso-thermal magnetization at 5 K is shown for $SrRu_{1-x}Ga_xO_3$ series with $x = 0.0, 0.05, 0.1$ and 0.2. The inset shows coercive field (H_c) by Ga doping variation in $SrRu_{1-x}Ga_xO_3$ series (b) The Arrott plot (M^2 vs H/M) of magnetization M (H) data at 5 K for $SrRu_{1-x}Ga_xO_3$ series and inset shows the saturation magnetization (μ_H) at 7 T and spontaneous magnetization (M_s) by Ga doping in $SrRu_{1-x}Ga_xO_3$ series.</p>	<p>106</p>
<p>5.7 (a) The temperature dependent variation in electrical resistivity $\rho(T)$ as function of temperature from temperature range of 5 K to 300 K in logarithmic form of $SrRu_{1-x}Ga_xO_3$ series with $x = 0.0, 0.05, 0.1$</p>	<p>108</p>

and 0.2. (b) The linear fitting in FL form in the FM region just below T_c for $x = 0.0$ and $x = 0.05$ of $\text{SrRu}_{1-x}\text{Ga}_x\text{O}_3$ series. (c) The $\rho(T)$ fitting in the high temperature range in the form of Mott-variable range hopping (VRH) of $\text{SrRu}_{1-x}\text{Ga}_x\text{O}_3$ series with $x = 0.0, 0.05$ (d) with $x = 0.1$ and 0.2 .

5.8 (a) The temperature dependent variation in electrical resistivity $\rho(T)$ as function of temperature from temperature range of 5 K to 300 K in zero and 8T applied magnetic field of SrRuO_3 (b) The MR% as function of temperature range of 5 K to 300 K of $x = 0.0$ and $x = 0.1$ (c) $x = 0.2$ of $\text{SrRu}_{1-x}\text{Ga}_x\text{O}_3$ series. (d) The MR% at 5 K of $\text{SrRu}_{1-x}\text{Ga}_x\text{O}_3$ series with $x = 0.0, 0.1$ and 0.2 .

6.1 The left axis shows temperature dependent dc magnetization of SrRuO_3 in the form of ZFC and FC from 5 K to 300 K and the right axis shows temperature dependent electrical resistivity $\rho(T)$ from 5 K to 300 K at 0 and 8T of the magnetic field and the inset shows magnetoresistance (MR) of SrRuO_3 from 5 K to 300 K.

6.2 (a) The temperature dependent resistivity $\rho(T)$ of $\text{SrRu}_{1-x}\text{Ti}_x\text{O}_3$ series with $x = 0.0, 0.1, 0.2, 0.3$ and 0.4 from 5 K to 300 K (b) The temperature dependent resistivity of $\text{SrRu}_{1-x}\text{Ti}_x\text{O}_3$ series with $x = 0.5$ and 0.7 from 5 K to 300 K.

6.3 The modified form of Mott VRH fitting of resistivity $\rho(T)$ in the high temperature range of $\text{SrRu}_{1-x}\text{Ti}_x\text{O}_3$ series with compositions of (a) $x = 0.0, 0.1, 0.2, 0.3$ and 0.4 (b) 0.5 and 0.7 .

6.4 The Fermi liquid (FL) behavior fitting of $\text{SrRu}_{1-x}\text{Ti}_x\text{O}_3$ series of $x = 0.0, 0.1, 0.2,$ and 0.3 with different temperature range below T_c .

6.5 The non-Fermi liquid (NFL) fitting of $\text{SrRu}_{1-x}\text{Ti}_x\text{O}_3$ series of $x = 0.0, 0.1, 0.2,$ and 0.3 with different temperature range below T_c .

6.6 The Kondo effect fitting $\rho(T)$ with logarithmic temperature of $\text{SrRu}_{1-x}\text{Ti}_x\text{O}_3$ series with $x = 0.0, 0.1, 0.2,$ and 0.3 from 5 K to 21 K.

- 6.7 (a) The MR at 5 K with variation of H and (b) shows MR at 200 K with variation of H^2 of composition of $\text{SrRu}_{1-x}\text{Ti}_x\text{O}_3$ series ($x = 0.0, 0.1, 0.4, 0.5$ and 0.7) (c) shows MR at 8T of field with variation of composition of $\text{SrRu}_{1-x}\text{Ti}_x\text{O}_3$ series at 5 K and (d) 200 K. 130
- 6.8 The MR at 5 K of $\text{SrRu}_{1-x}\text{Ti}_x\text{O}_3$ series with (a) $x = 0.0$, (b) $x = 0.1$, (c) $x = 0.3$, (d) $x = 0.4$, (e) $x = 0.5$ and (f) $x = 0.7$. 132
- 6.9 The MR at 5 K, 20 K and 40 K of $\text{SrRu}_{1-x}\text{Ti}_x\text{O}_3$ series with (a) $x = 0.0$, (b) $x = 0.1$, (c) $x = 0.3$, (d) $x = 0.4$, (e) $x = 0.5$ and (f) $x = 0.7$. 133
- 6.10 (a) The temperature dependent specific heat $C_p(T)$ of $\text{SrRu}_{1-x}\text{Ti}_x\text{O}_3$ series with $x = 0.0$ and 0.2 , and the upper and lower inset shows zoomed view of $C_p(T)$ and $M(T)$. (b) The straight line fitting of $C_p(T)$ in the form of equation (6.9) for $x = 0.0, 0.1, 0.2, 0.3, 0.4$ and 0.7 of $\text{SrRu}_{1-x}\text{Ti}_x\text{O}_3$ series. For clarity, the $C_p(T)/T$ data has been shifted by the rate of amount 0.02 upside for $x = 0.1, 0.2, 0.3, 0.4$, and 0.7 of $\text{SrRu}_{1-x}\text{Ti}_x\text{O}_3$ series. 135
- 6.11 The electronic specific heat coefficient (γ) on left axis and right axis shows Debye temperature (Θ_D) with the variation of Ti substitution in $\text{SrRu}_{1-x}\text{Ti}_x\text{O}_3$ series (b) The Kadowaki-Woods ratio with the variation of Ti substitution in $\text{SrRu}_{1-x}\text{Ti}_x\text{O}_3$ series. 137

List of Tables

3.1 The characteristic temperatures T_c , T_c^R and T_G are given for SrRu _{1-x} Ti _x O ₃ series.	44
4.1. Table shows the values of critical exponents β , γ and δ determined using different independent methods such as modifier Arrott plot (MAP), Kouvel-Fisher (KF) plot and critical isotherm analysis for SrRu _{1-x} Ti _x O ₃ series. The values of exponents calculated theoretically following different spin interaction models are also given for comparison.	68
5.1 The structural parameters of SrRu _{1-x} Ga _x O ₃ series with compositions $x = 0.0, 0.05, 0.1$ and 0.2 in terms of structural parameters a, b, c , unit cell volume (V) and basal bond length (Ru-O1), apical bond length (Ru-O2), basal bond angle (Ru-O1-Ru) and apical bond angle (Ru-O2-Ru)	93
5.2 The characteristic random critical temperature T_c^R (K), the inverse susceptibility exponent λ , Griffiths temperature (T_G) and the range of Griffiths temperature defined as $= [(T_G - T_c)/T_c] \times 100$ of SrRu _{1-x} Ga _x O ₃ series by dc magnetization.	101
5.3 Table shows the values of coefficient of modified Mott VRH behavior of SrRu _{1-x} Ga _x O ₃ series.	109
6.1 The table presents the values of ρ_{0M} and T_M by the variation of Ti doping.	121
6.2 This presents the values of FL, NFL and Kondo coefficients and temperature range by the variation of Ti doping.	127

Contents

0.1	Declaration	(ii)
0.2	Acknowledgements	(iii)
0.3	Abstract	(vi)
0.4	Publications.....	(ix)
0.5	List of Figures	(x)
0.6	List of Tables	(xvii)
Chapter 1: Introduction		1
1.1	Transition Metal Oxides	1
1.2	Magnetic materials.....	6
1.2.1	Localized Model	6
1.2.2	Itinerant Model and Stoner criteria	7
1.2.3	Phase Transition	9
1.2.4	Magnetocrystalline Anisotropy (MCA).....	10
1.2.5	Griffiths Phase.....	11
1.3	Transport Study.....	13
1.3.1	Fermi Liquid	13
1.3.2	Non-Fermi liquid.....	13
1.3.3	Metal-Insulator Transition.....	14
1.3.4	Kondo behavior.....	14
1.3.5	Magnetoresistance (MR).....	15
1.3.6	Specific Heat (C_p)	15
1.4	Motivation and goals of thesis work	16
	Bibliography	18
Chapter 2: Experimental Techniques and Apparatus		21
2.1	Sample Preparation and Synthesis techniques.....	21
2.2	Structural analysis and Characterization techniques	24
2.2.1	X-ray diffraction (XRD)	24
2.2.2	Rietveld refinement	25
2.3	Magnetization Measurements.....	27

2.3.1	PPMS	28
2.3.2	SQUID	30
2.4	Electrical Transport Measurement	31
2.4.1	Four Probe Technique	31
2.4.2	Specific Heat measurement	33
2.5	Conclusions	33
	Bibliography.....	34
Chapter 3:	Site dilution in SrRuO₃: Effects on structural and magnetic properties.....	36
3.1	Introduction.....	37
3.2	Experimental Details.....	39
3.3	Results and Discussion.....	39
3.3.1	Structural Study.....	39
3.3.2	Zero Field Cooled and Field Cooled Magnetization Data.....	44
3.3.3	Thermal Demagnetization Study.....	45
3.3.4	Nature of Magnetic State and Critical Exponent for Temperature Dependent Magnetization.....	48
3.3.5	Griffiths Phase Behavior.....	50
3.3.6	High Temperature Paramagnetic State and Curie-Weiss Behavior...	53
3.3.7	Magnetic Field Dependent Magnetization Study.....	55
3.3.8	Analysis of Arrott Plot and Spontaneous Magnetization.....	56
3.3.9	Electronic Transport Study.....	58
3.3.10	Behavior of transition temperature T _c with site dilution.....	60
3.4	Conclusion.....	60
	Bibliography.....	62
Chapter 4:	Critical behavior in itinerant ferromagnet SrRu_{1-x}Ti_xO₃.....	65
4.1	Introduction.....	65
4.2	Experimental Details.....	69
4.3	Results and Discussion.....	70

4.3.1	Scaling analysis.....	70
4.3.2	DC Magnetization Study.....	71
4.3.3	Arrott Plot.....	72
4.3.4	Kouvel-Fisher Plot	79
4.3.5	Critical Isotherm Plot.....	81
4.3.6	Scaling Analysis.....	83
4.3.7	Evolution of Exponents in $\text{SrRu}_{1-x}\text{Ti}_x\text{O}_3$	85
4.4	Conclusion.....	88
	Bibliography	89

Chapter 5: Effects of Site dilution and Ru-charge modulation on physical properties in $\text{SrRu}_{1-x}\text{Ga}_x\text{O}_3$

5.1	Introduction.....	91
5.2	Experimental Details	92
5.3	Results and Discussion.....	93
5.3.1	Structural Study.....	93
5.3.2	Magnetization Study for $\text{SrRu}_{1-x}\text{Ga}_x\text{O}_3$ Series.....	96
5.3.3	Thermal Demagnetization Study.....	98
5.3.4	Critical Exponent Behavior	102
5.3.5	Griffiths Phase Behavior.....	103
5.3.6	Isothermal Magnetization Study.....	105
5.3.7	Electrical Resistivity Study.....	107
5.3.8	Magnetoresistance study.....	110
5.4	Conclusion.....	112
	Bibliography.....	114

Chapter 6: Site dilution effect on Electrical Transport Behavior in $\text{SrRu}_{1-x}\text{Ti}_x\text{O}_3$

6.1	Introduction.....	117
6.2	Experimental Details.....	119
6.3	Results and Discussion.....	119
6.3.1	Electrical Resistivity Study.....	119
6.3.2	Electrical Transport in PM State.....	122
6.3.3	Electrical Transport in FM State.....	124
6.3.4	Kondo Behavior	128

6.3.5	Magnetoresistance (MR).....	129
6.3.6	Specific Heat.....	134
6.3.7	Kadowaki-Woods Ratio (KWR).....	138
6.4	Conclusion.....	138
	Bibliography.....	139

Chapter 7: Conclusion and future plan

7.1	Conclusions.....	141
7.2	Future plan.....	144

Chapter 1

Introduction

In this chapter, we discuss about general introduction of transition metal oxide and have given ruthenium-based perovskite structure. We have further given general description related to the effect of site dilution and structural modification and their effect on magnetic and transport properties in a material. The importance of present chosen sample as well as objectives of present dopant has been discussed. We have also discussed the related physics and phenomena such as exchange interaction and itinerant model of magnetism, critical behavior, Griffiths phase, Curie-Weiss law and Rhodes-Wohlfarth ratio, etc. The transport behavior has also been discussed in terms of Kondo, Fermi-liquid and Non-Fermi liquid behavior, Mott-type variable range hopping, negative magnetoresistance, etc.

1.1 Transition Metal oxides (TMOs)

The compounds formed by transition metals (TM) and oxygens are called transition metal oxides (TMOs). In periodic table, as shown in figure 1.1, the d block elements are known as transition metals in which d orbitals have partially or fully filled subshell. Another interesting point about TM is that it has more than one oxidation state and most of TM orbital shows metallic nature so it works as a platform or bridge between the other block of elements.

The TM in general has strong electron correlation effect (U), and due to that the observed physical properties in TMOs can not be explained with general band structure theory [3, 7-9].

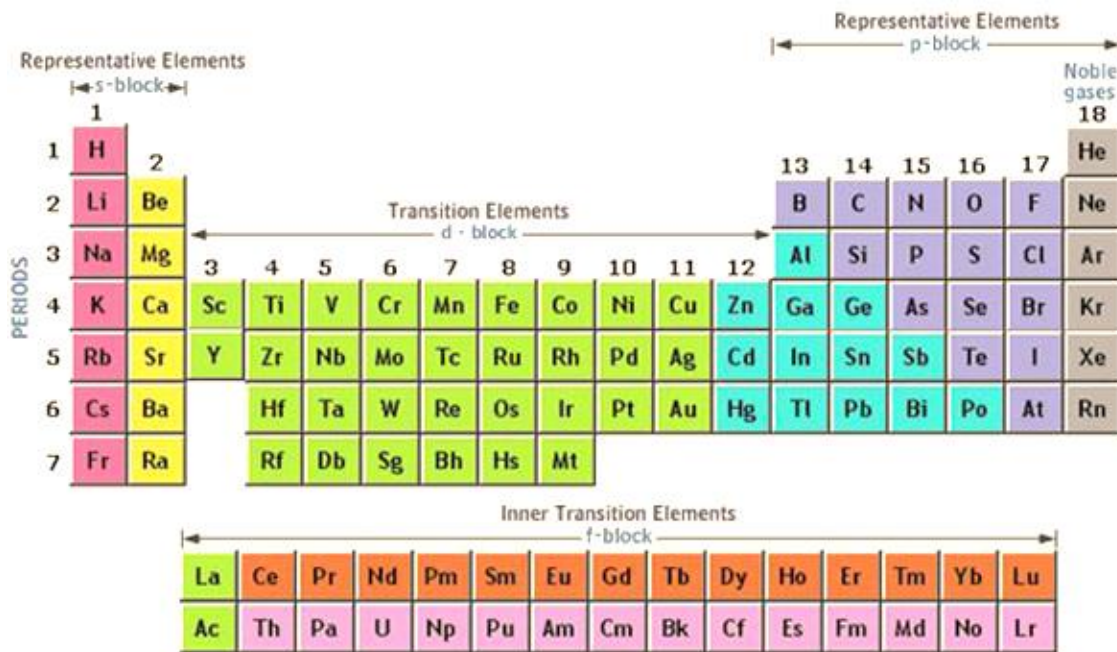


Figure 1.1 Periodic table shows d block transition metal elements.

However, the electronic property largely varies with d character of TMs. For instance, electron correlation effect (U) decreases when one move from $3d$ to $5d$ due to large radial extension of d orbitals. On the other hand the $5d$ based TMOs have heavy atomic nature of elements. The TMOs play an interesting role in showing many exotic phenomena such as metal to insulator transition (MIT), colossal magnetoresistance [10-12], charge and orbital ordering, phase separation, multiferroicity, high- T_c superconductivity [13], etc. The TMOs materials have wide activity in basic as well as applied science with many technological applications [1-3].

The electronic and magnetic properties of TMOs are very unusual where these properties can further be tuned significantly with chemical doping at different crystallographic sites. These complexities mainly arise due to the presence of many competing phenomena such as, charge-spin-orbit-lattice coupling, coulomb interaction, crystal field effect, Hund's

coupling, etc [4-6]. Often, the same material displays both types of transport properties, like MIT obtained by just varying either temperature or pressure. Therefore, subtle changes in material composition, pressure, magnetic field and temperature are expected to perturb the delicate balance between these inter-connected parameters and render new and exotic physics.

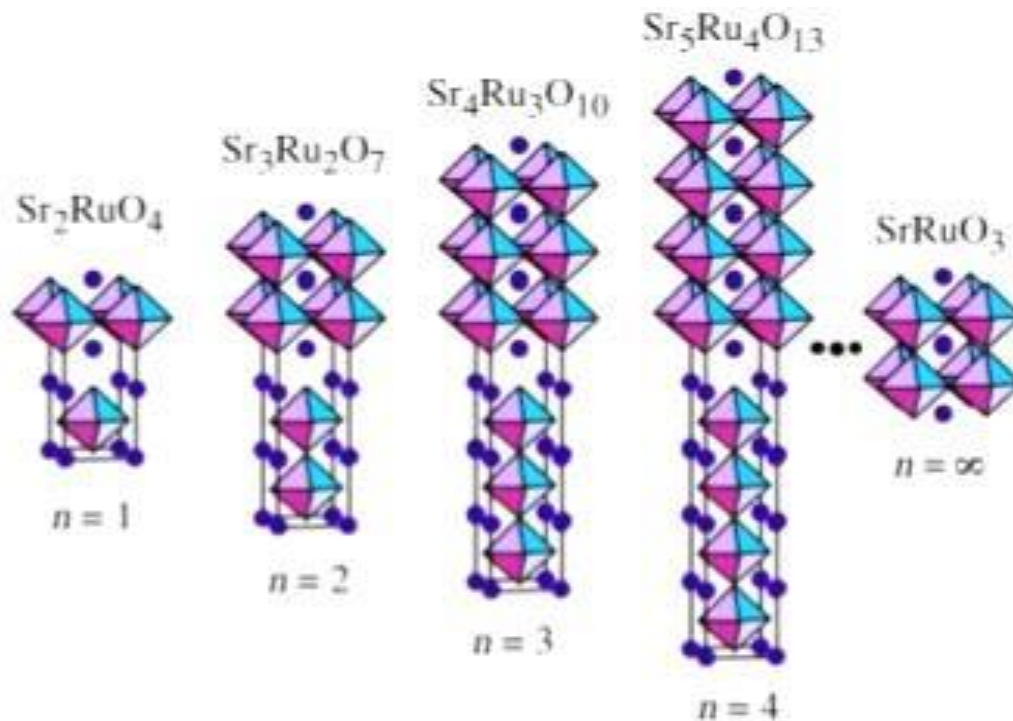


Figure 1.2 Ruddlesden-Popper series of $\text{A}_{n+1}\text{B}_n\text{O}_{3n+1}$ with varying n , where $\text{A}=\text{Sr}$ and $\text{B}=\text{Ru}$. Figure has taken from internet source.

Structural diversity is another important factor in these materials. Structural organization is basically realized with Ruddlesden-Popper phase which is described as $(\text{AO})(\text{ABO}_3)_n$ where A is trivalent or divalent element and B is transition metal. In this structure, successive n number of ABO_3 blocks is separated by AO layer. With $n = \infty$ leads to perovskite (ABO_3) structure where $n = 1$ single layer K_2NiF_4 structure, $n = 2$ bilayer structure and so on. Henceforth, the physical properties are also modified with the structural variation.

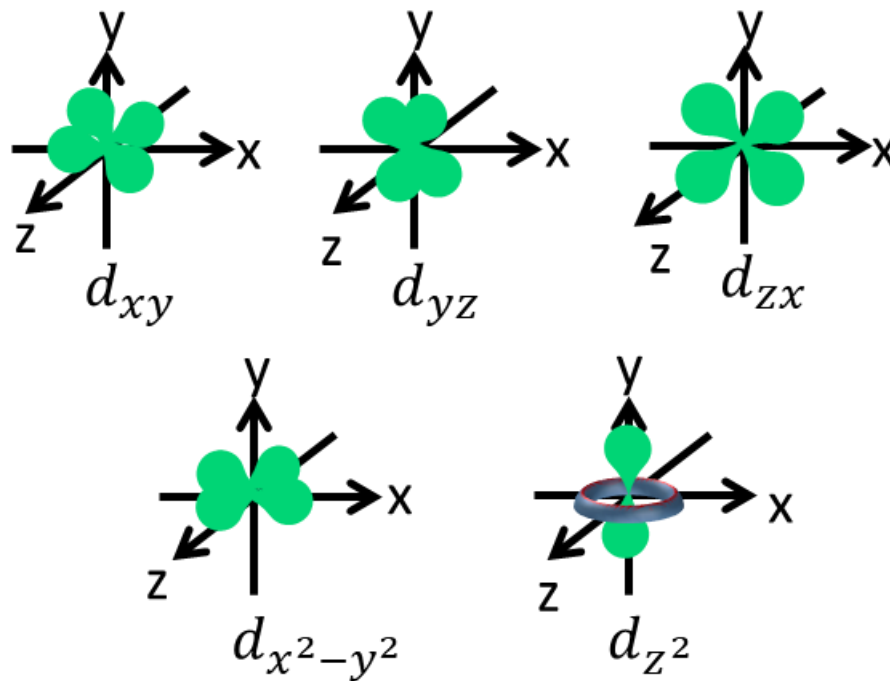


Figure 1.3 Schematic view of anisotropic shape of d orbitals.

Among the $4d$ based TMOs have special interest in TMOs as these materials have intermediate strength of U and SOC. Among the $4d$ TMOs Ru based oxides are an important family of materials showing many intriguing physics which is mostly related to their structural organization. Ru based TMOs offer an ideal system to the researchers. Though there have been plenty of studies in Ru based TMOs still many understandings need to be improved. The ruthenates have come in limelight of research after the discovery of superconductivity (SC) in Sr_2RuO_4 ($T_c \sim 1$ K). The other part of ruthenates is that with varying n , these materials show different interesting phenomenon like Ca_2RuO_4 which shows an antiferromagnetic (AFM) and insulating behavior. Similarly infinite layer perovskite structure SrRuO_3 shows itinerant type FM with metallic nature while similar other isoelectronic CaRuO_3 shows PM state with insulating behavior. Here we take interest in SrRuO_3 which shows itinerant type FM nature with ordering temperature $T_c \sim 160$ K and metallic behavior till high temperature (1000 K).

The TMs have five orbitals which are degenerate. The d orbital degeneracy of TMs is broken [14] when the orbitals come close to ligand atom (oxygen) the five orbitals have different orientations with respect to oxygen anion (due to anisotropic source of d -orbitals as shown in figure 1.3), hence the orbitals have different separation which gives effectively different coulomb energy. The orbitals are split into two energy states e_g ($d_x^2 - y^2$ and d_z^2) and t_{2g} (d_{xy} , d_{yz} and d_{zx}).

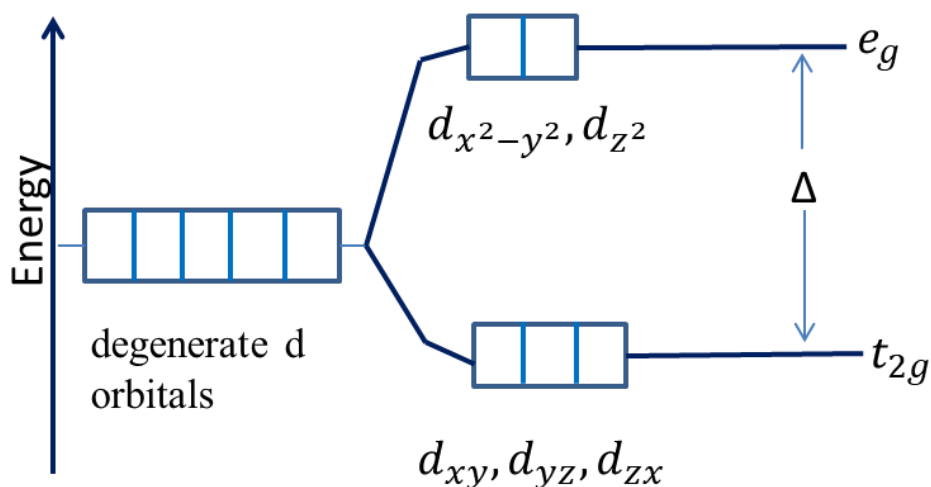


Figure 1.4 The schematic diagram of crystal field splitting.

For octahedral geometry, in which TM connected with six ligands so due to large d orbital axis energy e_g has higher energy than t_{2g} and the energy gap between e_g and t_{2g} is called crystal field energy (CFE) which has symbolized by Δ as shown in figure 1.4. In TM, two energies play vital role such as crystal field energy and Hund energy. When the crystal field energy is larger than the Hund energy, the low-lying t_{2g} is first filled which gives low-spin state. On the other hand, if the Hund energy is larger than the crystal field energy electrons are first singly filled in both e_g and t_{2g} before any pairing occurs according to Hund's rule, this results into high-spin state. In case of $3d$ TMOs, due to low value of CFE the system goes in the high spin state however for $4d$ and $5d$ based TMOs the situation is opposite which gives low spin state.

1.2 Magnetic Materials

Magnetic materials surround us as they play a crucial role in our day to day life and these materials have wide range of applications, such as medical devices, sensors, switches, memory devices etc. The magnetic moment in materials directed by magnetic field. The more common example is ferromagnet which has highly affected by magnetic fields. In condense matter physics, magnetism is a central subject and in solids come from uncompensated spin and orbital moment of electrons. In order to design material with good magnetic properties, basic understanding of magnetism is required. Mostly, in $4d$ TMOs, two models give the origin of magnetism as discussed below,

1.2.1 Localized Model

In localized model, the atom follow the Hund's rule and moment arises due to spin and orbital contributions of d electron from incomplete shells. The d electrons interact by following exchange interactions of direct (via Coulomb interaction) [23-25] or indirect coupling (via oxygen ions called superexchange). In localized system, the ordered saturation moment (μ_H) should be integer multiple of Bohr magneton (μ_B). In localized magnetic system, the individual interaction of moment represented as mean field effect (systems can picturize as average molecular field effect) [21] and also follows the Pauli's exclusion principle which shows quantum mechanical behavior. This mean field effect has been explained by Heisenberg by considering quantum mechanical exchange interaction of neighboring atoms which is further described as Curie Weiss law (CWL). The Heisenberg model gives representation of localized magnetism without the presence of magnetic field and can be written as [16-18]:

$$H = -J_{ij} \sum_{\langle ij \rangle} S_i \cdot S_j \quad (1.1)$$

Where J_{ij} is the exchange coupling constant between spins and $\langle ij \rangle$ [19] symbol imply that interaction possible between nearest neighbor spin pairs. The Hamiltonian equation depends on individual spin interaction in the 3D system.

If $J_{ij} > 0$; shows ferromagnetic (FM) nature and reveal nonzero magnetization below Curie temperature [20]

If $J_{ij} < 0$; shows antiferromagnetic (AFM) nature

The FM/PM/AFM nature can be understood in terms of spontaneous magnetization as well as exchange interaction. The exchange interaction is described as Coulomb repulsion between neighboring electrons in which FM arises due to intra-atomic interaction (stronger effect) than interatomic interaction. So for localized FM system, the Curie temperature (T_c) shows proportionality with exchange constant (J) by like $\left(T_c = \frac{z \times J}{k_B}\right)$, where z is number of first neighbors, k_B is the Boltzmann constant [22]. Further, the Curie Weiss behavior differentiate the criteria of FM, AFM and PM nature and defines as inverse susceptibility (χ^{-1}) variation with temperature and can be written as:

$$\chi = \frac{C}{T - \theta_p} \quad (1.2)$$

Here θ_p and C represent as Curie temperature and Curie constant. This follows the three cases:

When $\theta_p > 0$, the system is FM like,

$\theta_p = 0$, then system sustain Curie law of PM phase, and

$\theta_p < 0$, the system in non FM like

1.2.2 Itinerant Ferromagnetism and Stoner Criteria

When the conduction electrons are no longer localized, then delocalized or itinerant nature system arises in which electrons can move freely [15]. This was discussed by Stoner who figures out the itinerant FM nature. When certain balance occurs between kinetic, exchange and electron correlation energies, then band of spin-up and spin-down split with energy and arises all over non-zero magnetic moment. In these each spin sub-band contain only one type of spin and the magnetic moment arise through shifting of spin-up sub band from spin-down sub band at fermi level (figure 1.5) [27]. When density of states (DOS) is high at Fermi level (E_F) [26] then itinerant ferromagnetism arises and

the Stoner excitations appear by movement of opposite spin bands by following spin flip process. The Stoner criteria of itinerant ferromagnet are given below [28]:

$$U N(\varepsilon_F) > 1 \quad (1.3)$$

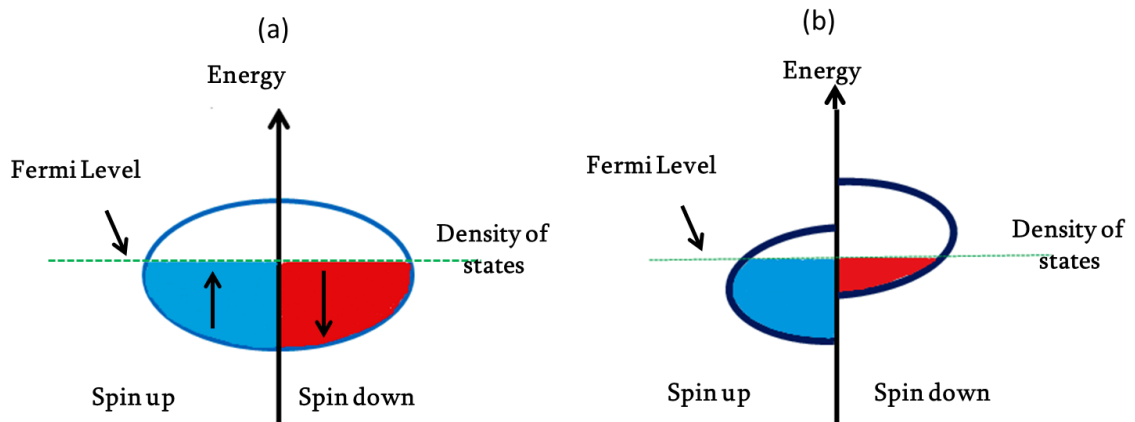


Figure 1.5 The two spin sub band of spin up and down spin (a) before splitting and (b) after splitting.

Where U is the Coulomb energy or electron correlation energy and $N(\varepsilon_F)$ is the density of states (DOS) at Fermi level. The Stoner splitting depends on following three assumptions:

- (i) The d spin bands are unsaturated.
- (ii) It follows Fermi statistics.
- (iii) The exchange effect consider as mean field manner.

The kinetic energy increases by the moment of spin sub band and decide ground state nature of either FM (inequality in number of spin up and down sub band) or PM. In itinerant FM nature, due to rearrangement of spin sub-band the net moment increases in one direction due to polarization of spins spontaneously and gives spontaneous magnetization (M_s) [11, 27]. The Stoner model also explains the non-integer value of saturation moment (μ_H) of metal at zero temperature but it fails to explain the Curie Weiss behavior above T_c .

The difference between localized and itinerant nature is that in localized model the moment arises due to rotation of spin with constant magnitude while in itinerant stoner model, moment arises by electron spin excitations in which single spin excitations change magnitude of magnetization. The criteria to characterize localize and itinerant ferromagnetic nature is known as Rhodes- Wohlfarth ratio (RWR) which can be written as q_c/q_s and follow some valuable range likes [32-34]:

if $q_c/q_s < 1$ then it shows localized magnetic nature and

if $q_c/q_s \gg 1$ then it shows itinerant nature of magnetism

where q_c can calculate by effective paramagnetic moment by using formula of $q_c(q_c + 2) = \mu_{\text{eff}}^2$ in high temperature range [35] and q_s is the saturation magnetic moment (μ_H) in ordered state.

1.2.3 Phase Transition

The phase transition is understood as developing new state from the previous one. The Ising FM state shows second order phase transition in which critical behavior come in terms of mean field behavior [31]. Close to transition temperature (T_c), the mean field behavior is thermodynamic quantities which have characterized by Critical exponents ($\beta = 0.5$, $\gamma = 1$ and $\delta = 1$) behavior in the following form

$$M_s(T) \propto \left(1 - \frac{T}{T_c}\right)^\beta \quad (1.4)$$

$$\chi_0^{-1}(T) \propto \left(\frac{T}{T_c} - 1\right)^\gamma \quad (1.5)$$

$$M(H) \propto H^{1/\delta} \quad (1.6)$$

When moving close to phase transition then behavior of order parameter fluctuations has important factor which is known as critical fluctuations. According to Landau theory, close to phase transition, critical behavior depends on particular order parameter and in case of magnetic phase transition the order parameter is magnetization.

The order parameter is a thermodynamic quantity which will be zero in disordered state and non-zero with unique nature in ordered phase state. Close to phase transition, only one physical relevant parameter is length scale which is correlation length (ξ) and has the following form:

$$\xi \propto \left| \frac{T-T_c}{T_c} \right|^{-\nu} \quad (1.7)$$

Where T_c is the critical temperature at which phase transition appears and ν is represented as exponent of correlation length. In second-order phase transitions correlation length diverges which is known as universal behavior. The results of mean field behavior in the form of Arrott equation [30]

$$M^2 = A + B \frac{H}{M} + \dots \quad (1.8)$$

Equation 8.1 following the isotherm plot of M^2 vs H/M gives spontaneous magnetization (M_s) as an intercept on M^2 axis due to straight line fitting in high temperature regime. The value of M_s will become zero in PM region. In ferromagnetic system, the magnetism originates from unpaired spin electrons which give spontaneous magnetization (M_s) and has permanent magnetic moment in which spin align in parallel direction in the absence of magnetic field and spin direction varies by variation of magnetic field which shows nonlinear transition and curve known as hysteresis loop.

1.2.4 Magnetocrystalline Anisotropy (MCA)

The Magnetocrystalline anisotropy (MCA) arises due to interaction energy of spin orbit and crystal field effect of electrons or due to interatomic dipole-dipole interaction energy which prefers the alignment of spin in some certain crystallographic easy axes direction in ordered crystalline structure. The crystallographic easy axis direction is with respect to lattice plane direction along which magnetization tends to align (in general c -axis). This easy axis is also called uniaxial axis and anisotropy in this known as uniaxial anisotropy which often arises in non-cubic crystal symmetry such as orthorhombic or hexagonal. The magnetic anisotropy of the system represents the internal energy which depends on

spontaneous magnetization direction and intrinsic property of the system. The magneto-crystalline energy (E) of uniaxial FM system can be written in series of power law form:

$$E = K_0 + K_1 \sin^2 \theta + K_2 \sin^4 \theta + \dots \dots \quad (1.9)$$

Where K_0, K_1, K_2, \dots are anisotropy constants which vary with temperature and material. The angle (θ) depends on magnetization vector and easy axis direction. The K_0 can neglect, because it does not depend on angle and when the easy axis is along c-axis direction of the crystal, for small angle the higher power terms has also neglected. So, only K_1 is important for this type of crystal which is known as Magnetocrystalline anisotropy constant [29].

Generally, Magnetocrystalline anisotropy energy is smaller than other compared exchange energy but the direction of moment is examined only by anisotropy because the magnetic moments try to align parallel not depends on which direction.

1.2.5 Griffiths Phase

The phase inhomogeneity and the quench disorder effect in a magnetic material by non-magnetic substitution is understood by Griffiths phase (GP) singularity which has originally proposed (in 1969) for randomly diluted Ising ferromagnetic (FM) system by non-magnetic atom (without spin) which explain as pre-formation of FM clusters. The Griffith singularity is explained due to the magnetic exchange interaction strength J and 0 are distributed randomly with probability p and $(1 - p)$, respectively. As shown in figure (1.6) for the range of $p < p_c$ (long-range FM order does not exist), while however, for $p > p_c$ long-range FM exist at $T_c(p = 1)$ which is known as Griffiths temperature (T_G). The region between $T_c(p) < T < T_G$ is known as GP region where the system neither exhibits pure PM behavior nor long-range FM order (i.e. no spontaneous magnetization) [36]. Experimentally, the Griffiths phase (GP) can be identified as rapid downfall of inverse susceptibility (χ^{-1}) as function of temperature before reaching the actual FM transition from the high temperature side.

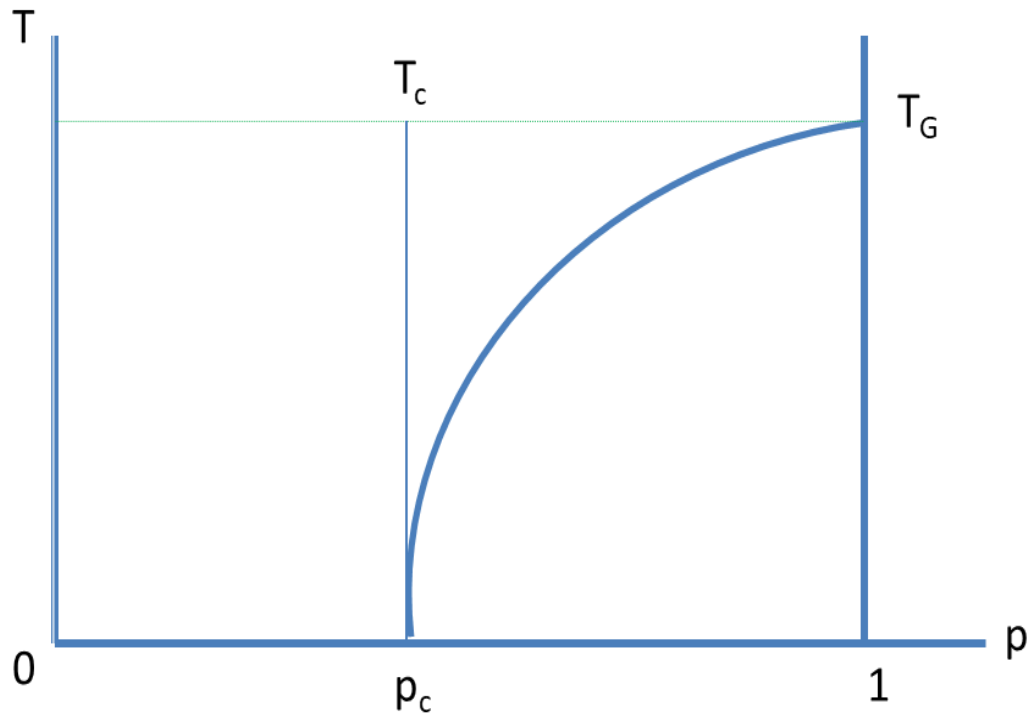


Figure.1.6 shows schematic diagram of Griffiths phase (GP) of theoretical explanation

This down fall in $\chi^{-1}(T)$ is broadened with applying high magnetic field. The Griffiths phase singularity is quantitatively understood as power law behavior:

$$\chi^{-1} \propto (T - T_c^R)^{1-\lambda} \quad (1.10)$$

where T_c^R is the random critical temperature, the exponent parameter $0 \leq \lambda \leq 1$, indicate the deviation from CW law. It shows PM behavior when $\lambda = 0$ from T_G (Griffiths temperature) to high temperature region and GP nature for $\lambda > 0$ between T_c to T_G which are shown in figure 1.7. This equation (Eq. 1.10) is the modified form of Curie Weiss law.

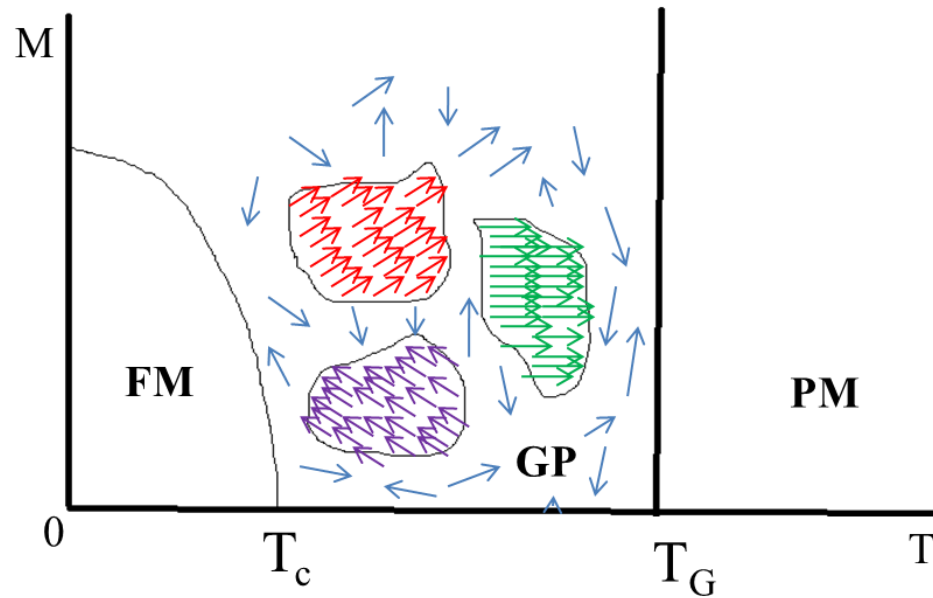


Figure.1.7 shows a schematic diagram of the Griffiths phase

1.3 Transport Study

1.3.1 Fermi Liquid

The Fermi liquid (FL) is a theoretical construction for interacting Fermi gas system. The interaction between the electrons works as adiabatically i.e. one to one mapping between non-interacting and interacting electron states [37]. The quasiparticles are main constituents of FL which have finite lifetime around fermi energy, interacts weakly and have high effective mass. The FL theory predicts many types of functional dependence of physical properties on temperature in which resistivity $\rho(T)$ has given below according to FL theory:

$$\rho(T) = \rho_0 + AT^2 \quad (1.11)$$

Where ρ_0 is the residual resistivity which is due to scattering at impurities and defect and A is FL coefficient ($\sqrt{A} \sim m^*$ in which m^* is the effective mass).

1.3.2 Non-Fermi Liquid

The non-Fermi liquid (NFL) behavior understand by breakdown of FL state due to any type of disorder like reducing dimension, close to quantum critical point or magnetic

instability. In this the effects of electron-electron interactions are more dominant. The NFL behavior can be expressed by the following relation:

$$\rho(T) \propto T^{3/2} \quad (1.12)$$

The NFL behavior has many origins but often observed close to magnetic instability or close to magnetic quantum critical point. The most the heavy fermions due to domination of fluctuations and also transition metals show deviations from Fermi liquid theory and show NFL behavior and FL recover on quantum critical point side [38].

1.3.3 Metal Insulator Transition

The metal insulator transition (MIT) in TMOs has been the big topic in condensed matter physics. In solid, the MIT specify as transition from metallic phase to insulating phase and vice versa. The MIT usually lead large change in resistivity due to some response of excitation like temperature, pressure or doping level [3]. The detailed study of transport properties and resolve the MIT mechanisms are needed for understanding of electron correlation effects in the material. The MIT can be categorized into Mott transition [39, 40], Peierls transition and Anderson localization.

Mott and Peierls analyzed that the insulating behavior should be due to electrons Coulomb repulsion. When the two electrons are on similar site then electrons feel strong Coulomb repulsion and when the interaction is large and valence band is half filled (number of valence electrons per site is one) then electrons cannot hop among neighboring sites and become insulator called as Mott insulator.

1.3.4 Kondo Behavior

In some metals; there is sudden rise in resistivity at low temperature below a certain temperature T_K which has opposite behavior from ordinary metals. This is called Kondo effect which has realized due to scattering of conduction electrons with magnetic impurity [41-42]. This extra scattering behavior of resistivity can be shown in logarithmic temperature dependence by the equation (1.13):

$$\rho(T) = \rho_0 + C \log\left(\frac{T_k}{T}\right) \quad (1.13)$$

Where ρ_0 is the resistivity due to non-magnetic impurities and the last term is caused by magnetic impurities and T_k is the Kondo temperature.

1.3.5 Magnetoresistance (MR)

In magnetic materials, the spin configuration depends on electron motion and the effect of external magnetic field on electrical resistance termed as magnetoresistance (MR). Under the presence of external field, the arrangement of spin inside material changes due to the Lorentz force with resultant change in mobility of electrons so the free electrons under the simultaneous effect of electric and magnetic field form spiral trajectory. The MR is the change in resistivity by applying magnetic field. Mathematically MR is defined as:

$$MR = \frac{\rho(H) - \rho(0)}{\rho(0)} \quad (1.14)$$

where $\rho(H)$ = resistivity under magnetic field

$\rho(0)$ = resistivity at zero applying field or absence of field.

1.3.6 Specific Heat (C_p)

The specific heat under constant pressure (C_p) is defined as the amount of heat that enters (delivered to/emitted) to a system divided by change in temperature of system and can represent by the formula [43]:

$$C_p = \frac{\Delta Q}{\Delta T} \quad (1.15)$$

Where ΔQ is the amount of heat added to the system to raise its temperature by an amount ΔT . The specific heat experiments are an easy way to study the phase transitions in materials. In an ideal metal, electrons can be viewed as non-interacting Fermi gas therefore Fermi-Dirac statistics play an important role in finding the temperature dependence of electronic contribution to specific heat. At temperature much below the

Debye and Fermi temperature ($T < T_F$), the heat capacity of metals can be written as sum of electron (C_e) and phonon or lattice (C_l) contributions [44]:

$$C_p = C_e + C_l = \gamma T + \beta T^3 \quad (1.16)$$

Where γ is Sommerfield constant and β is the lattice coefficient. So the electronic contribution can be written as [45]:

$$C_e = \frac{\pi^2}{3} N(\epsilon_F) k_B^2 T \equiv \gamma T \quad (1.17)$$

This can find by straight line fitting of C/T vs T^2 and taking intercept which gives information about density of states, $N(\epsilon_F)$ at Fermi surface. The slope of fitting gives Debye temperature (θ_D) by the formula:

$$\beta = \frac{12}{5} \pi^4 N k_B \left(\frac{T}{\theta_D} \right)^3 \quad (1.18)$$

1.4 Motivation and goals of thesis work

In present thesis, we have focused on the study of ruthenium based perovskite oxides structure (SrRuO_3) which is the end member in RP series with $n = \infty$. SrRuO_3 shows paramagnetic to ferromagnetic second-order phase transition at $T_c \sim 163$ K and also shows metallic nature over the whole temperature range [46]. There is some inter-correlation between electronic transport and magnetic behavior at T_c because resistivity $\rho(T)$ shows a change in slope across T_c . However, there is large volume of theoretical and experimental investigations but there magnetic and electronic properties and their inter-correlation is not fully understood. In this thesis, we have focused on SrRuO_3 and used route of chemical doping at Ru site to understand its evolution of magnetic and electronic properties. We have used two non-magnetic elements, namely Ti^{4+} ($3d^0$) and Ga^{3+} ($3d^{10}$). Both of these elements are non-magnetic in nature and they have matching ionic radii to Ru^{4+} (0.62 Å). Therefore, this substitution causes a minimum structural modification. This is important because structure plays a vital role in modifying the physical properties in case of TMOs.

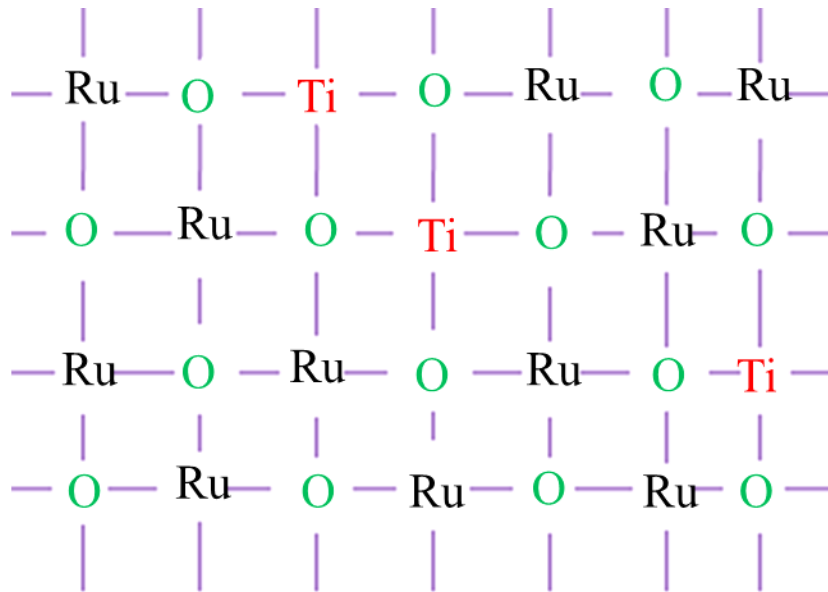


Figure 1.8 The site dilution effects by Ti substitution in SrRuO_3 which dilute the Ru-O-Ru chain.

In case of Ti doping, the Ti^{4+} will simply dilute the magnetic network formed by Ru-O-Ru channel as shown figure 1.8. In addition its $3d^0$ character will tune the electron correlation (U) and electron density which will effectively modified density of states (DOS) in material. In case of Ga^{3+} , it will again act for site dilution and modification in U though its $3d$ character. However, it will further alter the Ru charge state by converting Ru^{4+} to Ru^{5+} . Therefore mixed ionic states will be realized which will modify magnetic interaction and electronic charge accordingly.

Considering the SrRuO_3 has itinerant type FM, therefore, it is important to understand how the natures of magnetic interaction evolved in present substitution work. Here, it can be mentioned that in case of $\text{Sr}_{1-x}\text{Ca}_x\text{RuO}_3$ where Ca^{2+} substitution in SrRuO_3 weakens the magnetism and gives quantum phase transition (QPT) around $x = 0.7$, the critical exponents are shown to evolve interestingly [47]. Here, following this motivation critical behavior is required to be investigate in these series ($\text{SrRu}_{1-x}\text{Ti}_x\text{O}_3$ and $\text{SrRu}_{1-x}\text{Ga}_x\text{O}_3$). Following that both Ti^{4+} and Ga^{3+} dilutes the system with its non-magnetic nature so it requires to understanding the evolution of electronic properties with doping elements as well as with applying the magnetic fields.

Bibliography

- [1]. U Mizutani, Introduction to the electron theory of metals, Cambridge University Press, UK, 2001.
- [2]. Z. Yang, C. Y. Ko, and S. Ramanathan, Oxide Electronics Utilizing Ultrafast Metal-Insulator Transitions. *Annu Rev Mater Res* **41**, 337 (2011).
- [3]. M. Imada, A. Fujimori, and Y. Tokura, Metal-Insulator Transitions. *Rev. Mod. Phys.* **70**, 1039 (1998).
- [4]. L. Degiorgi, “The electrodynamic response of heavy-electron compounds,” *Reviews of Modern Physics*, **71**, 687 (1999).
- [5]. E. Dagotto, *Science* 309 (5732), 257 (2005).
- [6]. Stenger, C. G. F.; Burggraaf, A. *J. Phys. Status Solidi. A*, **61**, 653–664 (1980).
- [7]. N. F. Mott, Metal-Insulator Transitions (*Taylor and Francis, London*, 1974).
- [8]. P. Cox, Transition Metal Oxides (*Clarendon, Oxford*, 1992).
- [9]. P. Fulde, Electron Correlations in Molecules and Solids (*SpringerVerlag, Berlin*, 1991).
- [10]. D. Louca, T. Egami, E. L. Brosha, H. Röder, A. R. Bishop, *Phys. Rev. B*, **56**, 8475–8478 (1997).
- [11]. A. J. Millis, *Nature*, **392**, 147–150 (1998).
- [12]. A. J. Millis, B. I. Shraiman, R. Mueller, *Phys. Rev. Lett.* **77**, 175–178 (1996).
- [13]. J. R. Schrieffer and J. S. Brooks. Handbook of high-temperature superconductivity. Springer Science + Business Media, LLC (2007).

- [14]. Atkins, P. W.; Overton, T.; Rourke, J.; Weller, M.; Armstrong, F. Shriver and Atkins' Inorganic Chemistry, 5th ed.; *Oxford University Press, Oxford*, 2010.
- [15]. D.C.Mattis. *The theory of magnetism*. Springer-Verlag, Berlin, 1981.
- [16]. W. Heisenberg, Theory of the fermion liquid, *Z. Phys.* **49**, 619 (1928).
- [17]. P. A. M. Dirac. *The Principles of Quantum Mechanics*. Oxford University Press, New York, 1935. second edition.
- [18]. Chapter X., J. H. Van Vleck. *Rev. Mod. Phys.*, **17**, 27 (1945).
- [19]. C. Kittel. *Introduction to Solid State Physics*. Wiley, New York, 2005.
- [20]. S. Blundell, Magnetism in condensed matter (Oxford University Press, Oxford; New York, 2001), Oxford master series in condensed matter physics.
- [21]. J. M. D. Coey, *Magnetism and magnetic materials* (Cambridge University Press, Cambridge, 2009), 1st edn.
- [22]. R. Y. Díaz, Modeling of macroscopic anisotropies, <http://www.fgarciasanchez.es/thesisrocio/node1.html>.
- [23]. J. Hubbard, *Proc. R. Soc. London A* **276**, 238 (1963); **281**, 401 (1964).
- [24]. J. Kanamori, *Prog. Theor. Phys.* **30**, 275 (1963).
- [25]. M.C. Gutzwiller, *Phys. Rev. Lett.* **10**, 159 (1963)., E. C. Stoner. *Proc. Roy. Soc. London A*, 165:372, 1938.
- [26]. Shatruk, M. Chemical Aspects of Itinerant Magnetism. In review. 2017.
- [27]. E. C. Stoner, *Proc. Roy. Soc. (London)* **A165**, 372 (1938).
- [28]. Stoner, E. *Reports on Progress in Physics*, **11**, 43 (1947).
- [29]. B. D. Cullity, *Introduction to magnetic materials* (Addison-Wesley Pub. Co., Reading, Mass., 1972), Addison-Wesley series in metallurgy and materials.
- [30]. A. Arrott, *Phys. Rev.*, **108**, 1394 (1957).
- [31]. R. Krasnow and H. E. Stanley, *Phys. Rev. B*. 332 (1973).
- [32]. P. Rhodes and E. P. Wohlfarth, *Proc. Roy. Soc. (London)* **A273**, 247 (1963).
- [33]. T. Moriya, *J. Magn. Magn. Mater.*, **10**, 31-34 (1983).
- [34]. E.P. Wohlfarth, *J. Magn. Magn. Mater.*, **7**, 113 (1978).
- [35]. Y. Takahashi, *J. Phys.: Condens. Matter*, **13**, 6323-6358 (2001).

- [36]. R. B. Griffiths, *Phys. Rev. Lett.*, **23**, 17 (1969).
- [37]. L. Landau, “The theory of a fermi-liquid,” *Journal of Experimental and Theoretical Physics (U.S.S.R)*, **30**, 1058–1064 (1956).
- [38]. G.R. Stewart, *Rev. Mod. Phys.*, **73**, 797 (2001).
- [39]. N. F. Mott, *The Basis of the Electron Theory of Metals, with Special Reference to the Transition Metals. Proc. Phys. Soc. London, Sect. A* **62**, 416 (1949).
- [40]. N. F. Mott, *Metal-Insulator Transitions*, 2nd ed. (Taylor and Francis, London, 1990).
- [41]. A. C. Hewson. *The Kondo problem to heavy fermions. Cambridge studies in magnetism; 2.* Cambridge Univ. Press. ISBN 0-521-36382-9. XXI, 436 S: Ill., graph. Darst (1993).
- [42]. J. Kondo. Resistance Minimum in Dilute Magnetic Alloys. *Progress of Theoretical Physics*, **32**, 37-49 (1964).
- [43]. M W Zemansky, *Heat and Thermodynamics, McGraw-Hill, NewYork, 1957.*
- [44]. M. P. Marder, *Condensed matter physics. John Wiley & Sons, 2010.*
- [45]. C Kittel, *Thermal Physics, John Wiley and Sons Inc., NewYork, 1969.*
- [46]. P. B. Allen, H. Berger, O. Chauvet, L. Forro, T. Jarlborg, A. Junod, B. Revaz, and G. Santi, *Phys. Rev. B* **53**, 4393 (1996).
- [47]. D. Fuchs, M. Wissinger, J. Schmalian, C. L. Huang, R. Fromknecht, R. Schneider and H. v. Lohneysen, *Phys. Rev. B.*, **89**, 174405 (2014).

CHAPTER – 2

Experimental Techniques and Apparatus

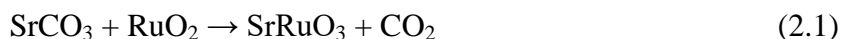
This chapter emphasizes the sample preparation and characterization techniques along with the experimental which have been used in the present thesis. All the polycrystalline samples studied in this thesis are synthesized by the solid-state reaction method. Further, the phase purity of samples has been checked with x-ray diffraction (XRD) measurements and the analysis of XRD data using Rietveld refinement [1]. The temperature dependent dc magnetization $M(T)$ and the field dependent isothermal magnetization $M(H)$ measurements have been performed using Superconducting Quantum Interference Device (SQUID) magnetometer and Physical Properties Measurement System (PPMS) system. The transport measurements such as resistivity $\rho(T)$, magnetoresistance (MR) and specific heat (C_p) have been carried out using homemade setup attached with superconducting magnet from Oxford Instruments, U.K.

2.1 Sample Preparation and Synthesis techniques

The solid materials can be divided into two categories: crystalline and non-crystalline which depends on their crystal structure [2]. A crystalline material can further be subdivided into single crystal and polycrystal where in former case the crystallographic axis orientation is the same throughout the sample where in latter one the individual grains crystallographic axis is independently oriented. Here we discuss the sample preparation and characterization technique related to polycrystalline sample. There are numerous synthesis methods to prepare the polycrystalline materials; among those, the solid-state reaction method is widely used [3]. This procedure is connected with the reactivity of raw materials in solid form in terms of physical diffusion of ions, so this

need method requires a high-temperature treatment. The final reaction depends on the kinetic and thermodynamic factors [4].

The kinetic factor decides the rate at which a reaction occurs while the thermodynamic factor decides the particular temperature at which reaction would take place. The solid-state reaction method offers a wide range of selection of starting materials such as oxides, carbonates, etc. In this method, two or more starting materials are taken in stoichiometric ratio then mixed and grounded properly. Moreover, the reactants react chemically without the presence of any solvent and provide stable final product, since this reaction does not occur at ambient room temperature [5]. The SSR method is also known as environment-friendly and does not involve the evolution of any toxic or waste material. A typical procedure for the synthesis of SrRuO₃ using Solid State Reaction (SSR) method is presented in Figure 2.1, where SrCO₃ and RuO₂ are used as starting materials.



We have followed the stepwise procedure to synthesize the polycrystalline materials using SSR method as briefly discussed below:

- (i) **Grinding:** The raw chemicals with stoichiometric ratio are mixed in an agate mortar and pestle, and grounded for homogeneous and uniform mixing [6]. The grinding of reagents increases the contact area which increases the rate of reaction.
- (ii) **Calcination:** Sample is calcined at high temperature to remove the CO₂ and H₂O and to achieve diffused constituent atoms [7].
- (iii) **Pelletization:** After the calcination, the powder is again ground and pressed into pellets using a pelletizer by applying pressure of few tons. When the powder is pressed to form a pellet, it maximizes the surface contact between the grains which increase the reaction rate and homogeneity of the sample.
- (iv) **Sintering:** It is the method for making a final product by heating of material below the melting point but more than the calcination temperature. These steps provide a high level of purity in sample [8].

In the present research work parent compound SrRuO_3 and their doped series have been synthesized using the solid-state reaction method.

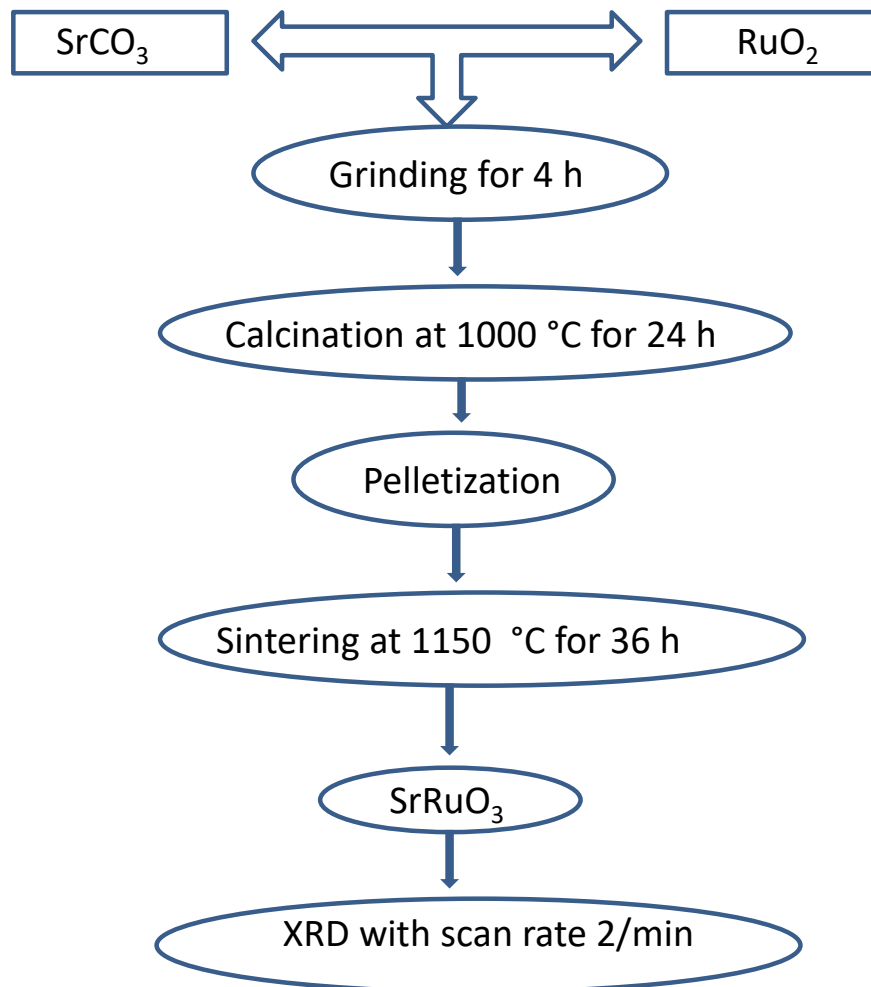
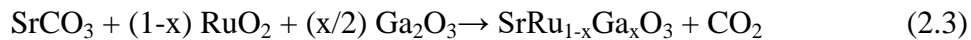


Figure 2.1 Stepwise procedures to synthesis SrRuO_3 using Solis State Reaction (SSR) method.

Preparation of polycrystalline samples series of $\text{SrRu}_{1-x}\text{Ti}_x\text{O}_3$ and $\text{SrRu}_{1-x}\text{Ga}_x\text{O}_3$

The polycrystalline samples series of $\text{SrRu}_{1-x}\text{Ti}_x\text{O}_3$ ($x = 0.0, 0.1, 0.2, 0.3, 0.4, 0.5$ and 0.7) and $\text{SrRu}_{1-x}\text{Ga}_x\text{O}_3$ ($x = 0.0, 0.05, 0.1, \text{ and } 0.2$) have been prepared by solid-state reaction method where the ingredient materials of SrCO_3 , RuO_2 , TiO_2 and Ga_2O_3 with phase purity 99.999% (Sigma-Aldrich) are taken in stoichiometric ratio. The reactions related to samples are following



The starting raw materials have been measured using high precision weighing machine. Then the mixture has been thoroughly grounded for 4 – 5 hours in agate mortar and pestle. After this, the powder has kept in the furnace at 1000 °C for calcination with the ramp rate of 2 degree per minute. This step is followed twice with an intermediate grinding. After the calcination process, powders are made into pellet and transferred in the furnace at 1150 °C with intermediate grindings. A small portion of the sample is ground into fine powders to investigate its crystallinity using XRD.

2.2 Structural analysis and Characterization techniques

X-ray diffraction has been used to check the purity and compositions of the polycrystalline samples the XRD data are with Rietveld refinement to obtain crystallographic parameters.

2.2.1 X-ray diffraction (XRD)

Similar to light, the x-ray is an electromagnetic wave which can travel in a straight line with a short wavelength of the order of few Angstroms (between 0.02 to 100 Å) which has a similar length scale of atomic bonds in solids [9]. The x-ray diffractometer (XRD) is a powerful technique to examine the crystallinity of the material which has been discovered by German physicist Wilhelm Roentgen in the year 1885. The XRD is based on the Bragg's law which balances a definite relation between the wavelength of x-ray (λ), incident angle (θ) and inter-planner distance (d) which yields intense reflection [9]. The Bragg's equation is given below

$$2d \sin \theta = n\lambda \quad (2.4)$$

where n is an integer.

In powder XRD measurement, either the wavelength (λ) or the incident angle (θ) need to vary for constructive interference. The XRD peaks are directly related to the atomic distance or plane. The block diagram of XRD arrangement and the different sets of plane is shown in Figure 2.2 (a) & (b). In the present case, λ is kept fixed and the sample is

rotated. The XRD is considered as a useful and popular tool to check the phase as well as purity of the samples which is much required for the physical properties of materials mostly depends on atomic arrangements.

The XRD gives the following informations:

- (i) The phase and quality of the sample
- (ii) Interplaner spacing

In the present research work, XRD data has taken by using a Rigaku MiniFlex diffractometer with CuK_α radiation ($\lambda = 1.5406 \text{ \AA}$) at room temperature. In this instrument both the x-ray source and the detector, move at different angles to fulfill the Bragg's condition and the corresponding intensity has been recorded. The XRD spectrum for samples is recorded in the range of 10 - 90 degree with a step size of 0.02° and rate of 2 deg per minute. The accurate values of lattice parameters of material calculated using the Rietveld refinement method of XRD data [10].

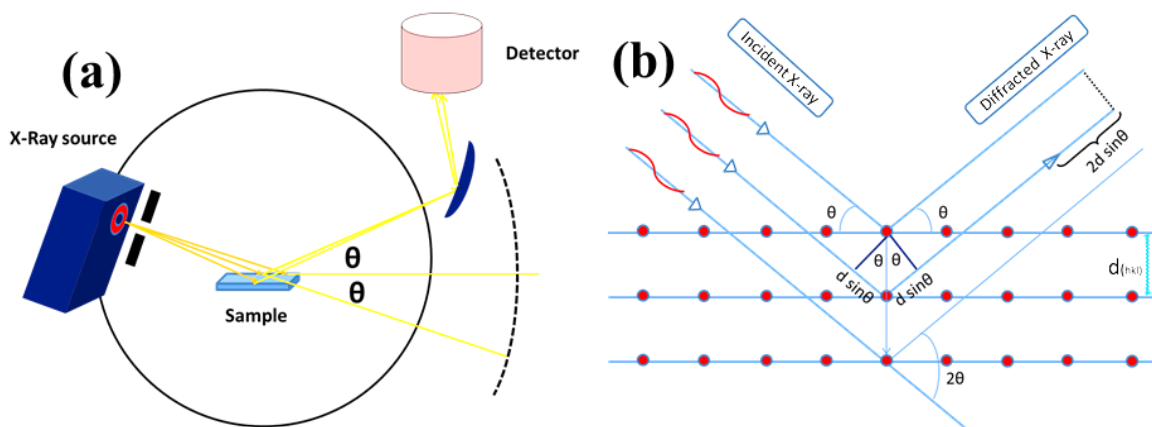


Figure 2.2 Schematic of XRD diffractometer (a), and Bragg's law to determine the interplaner separation (b).

2.2.2 Rietveld Refinement

Rietveld refinement is used to analyze or refine the XRD data to this method gives phase purity and accurate values of crystallographic parameters such as unit cell parameters, site occupancies and atomic positions etc. of the materials. The Rietveld refinement analysis of powder XRD was first proposed in 1967. It is a very useful tool for structural characterization of solids materials [11]. In this method, the least square refinement

fitting is carried out until the best fitting is realized which has in terms of measured and calculated diffraction patterns. The calculated pattern compares the detail information of crystal structure. The powder diffraction pattern of crystalline material has the definite reflection pattern with combination profiles of peak height, peak position and integrated area that is in proportionality with Bragg intensity I_{hkl} (where h, k, and l are the Miller indices). Since many Bragg reflections are observed, the intensity pattern at an arbitrary point, is determined by structure factor with absolute value ($|F_K|^2$), where $|F_K|^2 =$ sum of all contributions of neighbors Bragg reflections and background. The calculated intensity (y_{ci}) is given by

$$y_{ci} = s \sum_K L_K |F_K|^2 \phi(2\theta_i - 2\theta_K) P_K A + y_{bi} \quad (2.5)$$

where $s =$ the scale factor,

$L_K =$ composed of Lorentz, polarization and multiplicity factors

$\Phi =$ reflection profile function

$P_K =$ preferred orientation function

$A =$ absorption factor

$Y_{bi} =$ background intensity at i^{th} step

The least squares fitting has represented by the residue (S_y) which can define as

$$S_y = \sum_i w_i (y_i - y_{ci})^2 \quad (2.6)$$

Where $w_i = 1/y_i$,

$y_i =$ measured intensity at i^{th} step

$y_{ci} =$ calculated intensity at i^{th} step and the sum is over all data points.

The various numerical factors are used which judge that the fitting that has reached global minimum. The criteria of factors are:

R-structure factor

$$R_F = \frac{\sum |(I_K(obs))^{1/2} - (I_K(cal))^{1/2}|}{\sum (I_K(obs))^{1/2}} \quad (2.7)$$

R-Bragg factor

$$R_B = \frac{\sum |I_K(obs) - I_K(cal)|}{\sum I_K(obs)} \quad (2.8)$$

Here $I_K = K^{\text{th}}$ intensity of Bragg reflection of the end of refinement cycles. The fitting criteria can be quantified by several residual (R) minimum values like residual pattern (R_p) and residual weighted pattern (R_{wp}):

$$R_p = \frac{\sum |y_i(obs) - y_i(cal)|}{\sum y_i(obs)} \quad (2.9)$$

and

$$R_{wp} = \left\{ \frac{\sum w_i (y_i(obs) - y_i(cal))^2}{\sum w_i (y_i(obs))^2} \right\}^{1/2} \quad (2.10)$$

The ratio of R_{wp} and R_p decide the quality of the sample and most common achieved minimum value. Where $y_i(obs)$ and $y_i(cal)$ are the observed and calculated intensities of i th step respectively.

R -expected

$$R_{EXP} = \left[\frac{N_{obs} - N_{var}}{\sum w_i y_{oi}} \right]^{1/2} \quad (2.11)$$

where N_{obs} is the total number of observation and N_{var} is the variable of the least squares of refinement.

One another useful numerical criteria is goodness of fit ($GOF = \chi^2$) which is given in equation below and its value 1.3 or less is usually considered as satisfied fitting [12].

$$\chi^2 = \frac{M}{(N_{obs} - N_{var})} \quad (2.12)$$

In the present study, the modified version of the refinement program has been used which has given by Young et al. [13] and the pseudo-Voigt function has been used to fit the observed patterns.

2.3 Magnetization measurements

The magnetization measurements as a variation of temperature and magnetic field provide valuable information about the magnetic state in materials. The dc magnetization

of the magnetic sample can be measured in several ways such as force method, the torque method, induction method, etc. Among these methods, induction method is the most commonly used method in which sample is vibrated in middle of two opposite wound pickup coils, where the magnetic field is generated with the primary coil. At the constant magnetic field, the voltage induced in the pick-up coils is directly proportional to the magnetic flux through the coils. The dc magnetization measurements $M(T)$ are measured as in zero fields cooled (ZFC), and field cooled (FC) protocol. The $M(T)$ data has been taken by following procedure in which first sample is cooled from room temperature to low temperature. After applying the magnetic field, the data has been measured while warming is called ZFC. In field cool way, the system again cool down to low temperature in presence of applied field and again data has taken while warming is called FC. The hysteresis cycle can measure by different orientations of sample w.r.t. the vertical magnetic field. So by varying magnitude of the uniform field, the $M(H)$ has measured at a constant temperature. To study the critical behavior, $M(H)$ data has been measured at different temperatures across T_c . To measure each $M(H)$ curve sample is warmed above T_c then cooled down to particular temperature for $M(H)$ measurement. This procedure is repeated for each $M(H)$ curve.

The dc and isothermal magnetization measurements have been measured by using commercial vibrating sample magnetometer (VSM) in Quantum Design Physical Properties Measurement System (PPMS) and also by Superconducting Quantum Interference Device (SQUID). Here the working principle of these two measurement systems is briefly discussed below.

2.3.1 Physical Property Measurement System (PPMS)

The Quantum Design Physical Property Measurement System (PPMS) is attached with a temperature controlling system and superconducting magnets [14]. In the PPMS, the vibrating sample magnetometry (VSM) technique is used. The VSM is a sensitive method to measure the magnetic properties and is based on change of flux in the coil when the sample vibrates near to it [15, 16]. In this system, the sinusoidal oscillation of sample induces an alternating voltage in the static pickup coils which is directly

proportional to magnetization. According to Maxwell's law, the time-varying magnetic flux induces a voltage in a pickup coil. The magnetic flux changes in the area of coil set due to vibration of the sample which induce an electromotive force (emf) following Faraday's law [17, 18]. The sample is mounted equidistant between two pick-up coils which wound in opposite senses (to filter the homogeneous external magnetic field and measure inhomogeneous magnetic) and vibrated about this central position with a known sinusoidal frequency. In this, movement of the sample at the center of the pick-up coil induces voltage signal which is measured by a lock-in amplifier. This lock-in amplifier increases the signal to noise ratio (S/N) and the calibration of voltage gives magnetization. Figure 2.3 shows the schematic view of VSM in which magnetic field (H) supplied by the superconducting magnet and the sample is vibrated between the two signal pick-up coils has shown.

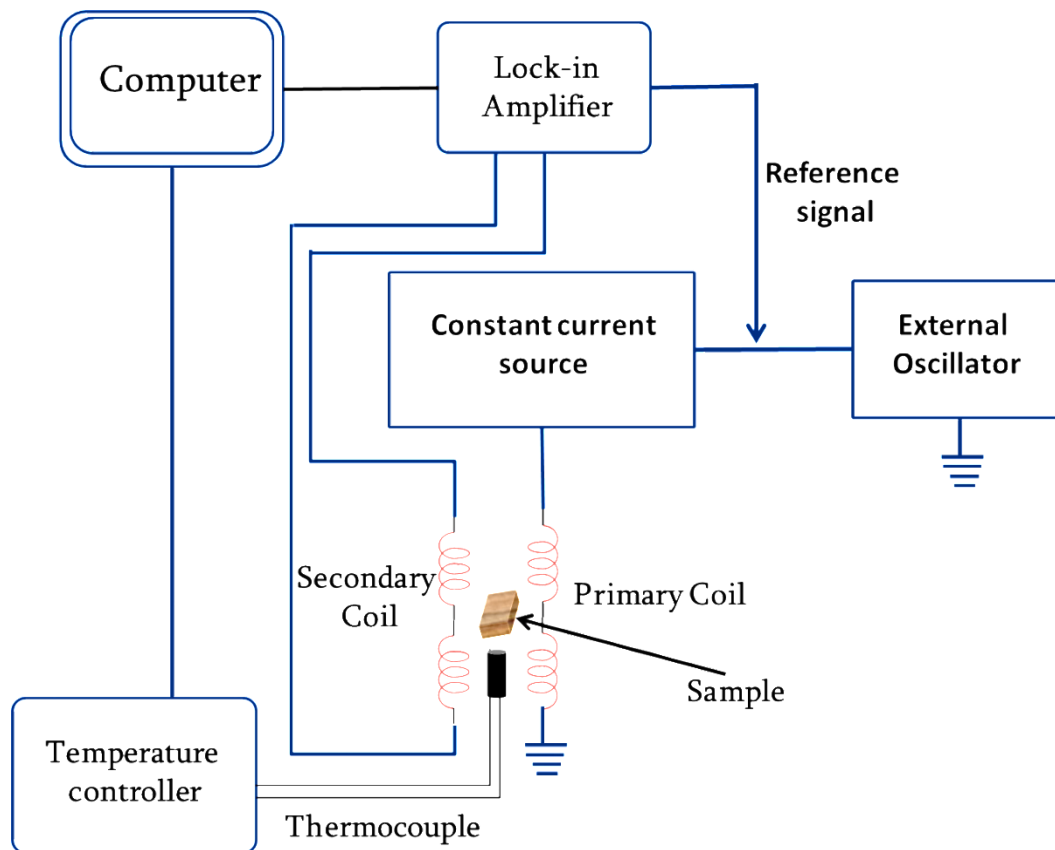


Figure 2.3 Schematic of Physical Properties Measurement System (PPMS).

2.3.2 Superconducting Quantum Interference Device (SQUID)

The Superconducting Quantum Interference Device (SQUID) has two superconducting rings of Josephson junctions (separated by an insulating layer) in two arms (at different phases), in which the Cooper pairs with different phases can tunnel and produce a current flow and the Josephson ring are placed in the vertical magnetic field [19].

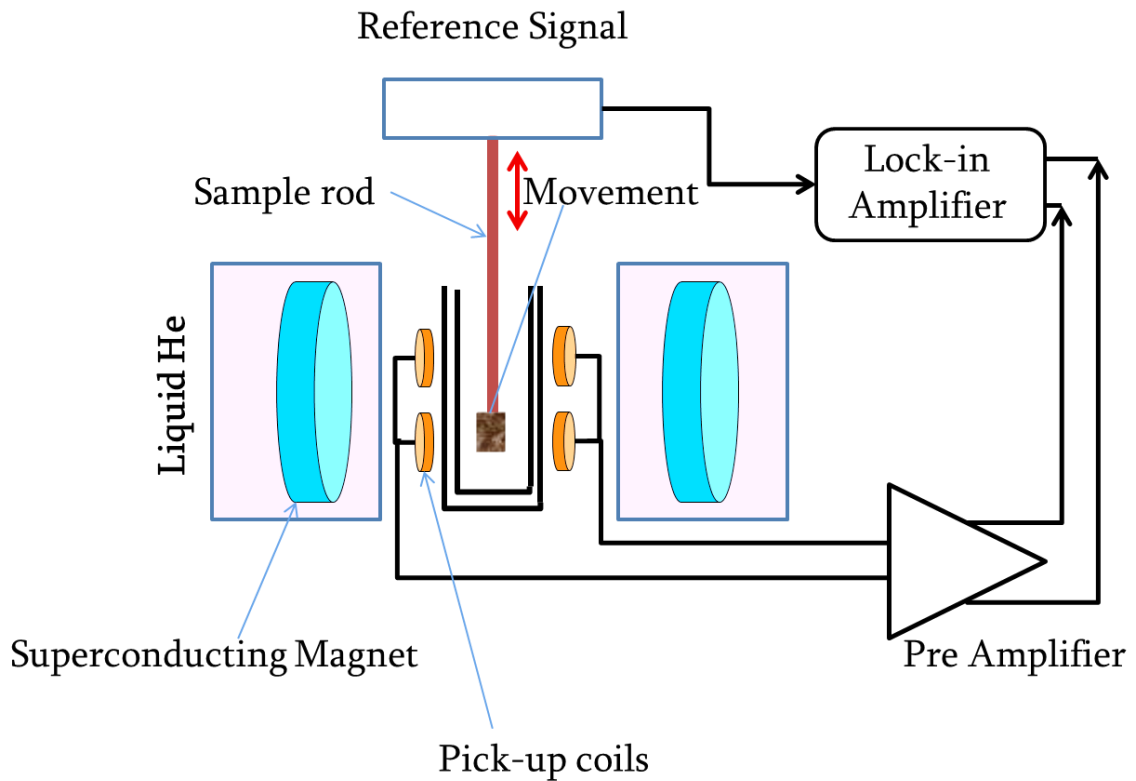


Figure 2.4 Schematic of Superconducting Quantum Interference Device (SQUID).

The main components of SQUID are superconducting magnet, a superconducting detecting coil or pickup coil, and the superconducting magnetic shield. The special superconducting detection coil is used for filter out the homogeneous magnetic field because it will induce opposite electric field which cancels each other and so that sample can be measured in the inhomogeneous magnetic field. The detection coil is placed at the center of the magnet arranged as (wound opposite) to form second-order gradiometer and connected to the SQUID by superconducting wires [20]. The sample is step scanned at a

constant rate through the gradiometer ring in the uniform magnetic field and the change of flux associated with this movement produce change in the induced persistent current through the ring. The induced persistent current proportional to frequency and voltage of the junction and thus its calibration gives magnetization. A schematic of the SQUID system is presented in Figure 2.4 [21]. One oscillation in ring belongs to increase of field by one quantum flux [$\phi_0 = h/2e$, where h is the Planck's constant and e is electronic charge].

2.4 Electrical Transport Measurement

Four probe technique has measured the electrical transport behavior such as, electrical resistivity $\rho(T)$ and magnetoresistance (MR) by using a home-built insert which has fitted with an Oxford superconducting magnet and closed cycle refrigerator (CCR). The specific heat measurements are done by using semi adiabatic technique.

2.4.1 Four Probe Technique

The electrical resistivity $\rho(T)$ has been measured by the standard four-probe method. This method has four leads (two outer and two inner) which are connected by silver paint on the sample as shown in Figure 2.5.

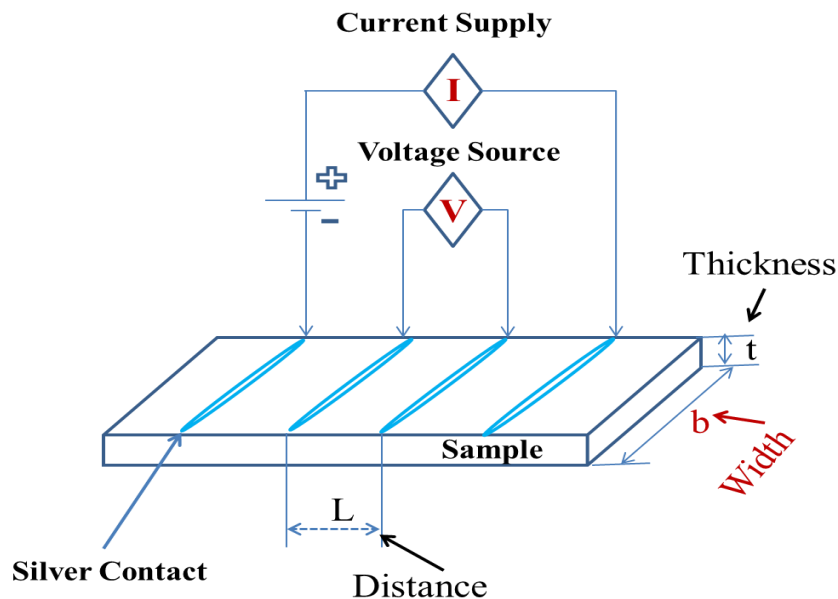


Figure 2.5 Schematic diagram of four probe configuration of the sample.

In this configuration, the current (I) passes through the outer two contacts and the voltage drops (V) is measured across the inner two contacts. The resistance (R) depends on sample geometry so for the intrinsic property $\rho(T)$ is more appropriate when comparing various systems. The $\rho(T)$ is calculated by taking the dimensions of cross-section area ($A = b \times t$, where b and t are the dimensions of the sample) and length (L) between two inner wire as given in below equation.

$$\rho = R \frac{A}{L} \quad (2.13)$$

In the present research work, $\rho(T)$ measurements have been done from low temperature to room temperature. The $\rho(T)$ measurements in the presence of a magnetic field (80 kOe) have been done by using superconducting magnetic system (Spectromag 2000) from Oxford Instruments, UK.

Magnetoresistance (MR)

The magnetoresistance (MR) is the change in resistivity in the presence of magnetic field. The following relation can calculate the MR,

$$MR = \frac{\rho(H) - \rho(0)}{\rho(0)} \quad (2.14)$$

where $\rho(H)$ = resistivity under magnetic field and $\rho(0)$ = resistivity at zero fields or absence of field.

If the applied magnetic field (H) is parallel to the direction of current (I), then it is called the longitudinal MR and if the magnetic field is applied perpendicular to the direction of the current, then it is called the transverse MR. The MR data presented in this thesis is the longitudinal MR.

MR can be measured in two different modes:

- (i) MR by varying temperature (T) in the constant magnetic field (H).
- (ii) MR by varying magnetic field (H) at constant temperature (T).

2.4.2 Specific Heat measurements

The specific heat is an important tool to study the magnetic phase transition and electronic properties. The specific heat (C_p) measurements have been carried out using a home-made set-up which is based on semi (or quasi)-adiabatic heat pulse method. The $C_p(T)$ has been measured in the temperature range of 5 to 200 K. Using this set-up, measurements of four samples can be performed simultaneously [15]. In this method, few hundred milligrams of is placed on the microcalorimeter platform (sample holder) using glue N -grease has used to avoid uncontrolled heat exchanger. In this method, “First thermalized the sample at particular temperature by heating by which heater heats the sample platform for a fixed time and after that heater is switching off the heater and the system relaxes adiabatically back to initial temperature and relaxation time constant has estimated”. The specific heat (C_p) can be obtained by relaxation time constant [22]. Repeating the same measurement at different temperature ranges has yield temperature-dependent specific heat. In short, the specific heat is the adding and removing a certain amount of heat from the system and monitoring the change in temperature at constant pressure [$C_p = (dQ/dT)_p$].

2.5 Conclusions

The series polycrystalline samples with perovskite structure of $\text{SrRu}_{1-x}\text{Ti}_x\text{O}_3$ ($x = 0.0, 0.1, 0.2, 0.3, 0.4, 0.5$ and 0.7) and $\text{SrRu}_{1-x}\text{Ga}_x\text{O}_3$ ($x = 0.0, 0.05, 0.1$ and 0.2) have been prepared by solid-state reaction procedure. The XRD data show single-phase behavior for the whole series where the samples and crystallize in the orthorhombic structure of $Pbnm$ space group. The XRD data have been analyzed by Rietveld refinement method and show no change in structure by doping. Magnetization measurements have been done with SQUID and PPMS magnetometer. Electrical transport behaviors of samples have been measured following four probe techniques.

Bibliography

- [1]. FullProf Suite, comprehensive set of crystallographic tools for Rietveld, profile matching & integrated intensity refinement of x-ray and/or neutron data. <http://www.ill.eu/sites/fullprof>.
- [2]. J. Solyom. Fundamentals of the Physics of Solids, *Springer-Verlag, Berlin, Heidelberg*, 2007.
- [3]. A.J. Moulson, J.M. Herbert, Electroceramics: Materials, Properties, Applications, *John Wiley & Sons*, 2003.
- [4]. A. R. West, Solid State Chemistry and Its Applications, *John Wiley & Sons*, Singapore (1987).
- [5]. G.C.C. da Costa, A.Z. Simões, A. Ries, C.R. Foschini, M.A. Zaghete, J.A. Varela, Phase formation and characterization of BaBi₂Ta₂O₉ obtained by mixed oxide procedure, *Mater. Lett.* **58** (11) (2004) 1709-1714.
- [6]. J.K. Beddow, Particle Characterization in Technology: Applications and *Microanalysis*, *CRC Press*, 1984.
- [7]. Y. Xu, Ferroelectric Materials and Their Applications, *North-Holland*, 1991.
- [8]. Schultz, M. Jerold, Properties of Solid Polymeric Materials: Treatise on Materials Science and Technology. **10**. *Elsevier*, 2017.
- [9]. B.D. Cullity and S.R. Stock. Elements of X-ray Diffraction, Prentice Hall, *Upper Saddle River*, NJ, 2001.
- [10]. H. M. Rietveld: *J. Appl. Crystallogr.* **2** (1969), 65.
- [11]. H. M. Rietveld, *Acta Cryst. A* **49**, 151 (1967).

- [12]. R. A. Young, The Rietveld Method, *International Union of Crystallography and Oxford University Press*. (1993).
- [13]. A. Young, A. Sakthivel, T. S. Moss, C. O. Paivasantos, Users Guide to program DBWS-9411, *Georgia Institute of Technology* (1994).
- [14]. Brochure for Physical Property Measurement System. *Technical report, Quantum Design*, www.qdusa.com, 2003.
- [15]. S. Foner, Versatile and Sensitive Vibrating-Sample Magnetometer, *Review of Scientific Instruments* **30**, 548 (1959).
- [16]. S. Foner, *Review of Scientific Instruments*, **27**, 578 (1955).
- [17]. Stephen Blundell. Magnetism in Condensed Matter, *Oxford University Press*, 2008.
- [18]. David Jiles. Introduction to Magnetism and Magnetic Materials, *Chapman and Hall*, 1998.
- [19]. B. D. Josephson, Possible new effects in superconductive tunneling, *Physics Letters* **1**, **7** (1962): 251-253.
- [20]. Casa Software, Casa XPS Manual, *Casa Ltd.* 2009.
- [21]. F. Palacio, E. Ressouche and J. Schweizer, Introduction to Physical Techniques in Molecular Magnetism, *University of Zaragoza Press* (2001).
- [22]. J. S. Hwang, K. J. Lin, and C. Tien, *Review of Scientific Instruments* **68**, 94 (1997).

Chapter 3

Site dilution in SrRuO₃: Effects on structural and magnetic properties

This chapter discusses the effect of site dilution with the substitution of nonmagnetic element in SrRu_{1-x}Ti_xO₃ ($x \leq 0.7$) series. The nature of the ferromagnetic state in SrRuO₃ is believed to be of the itinerant type with transition temperature $T_c \sim 162$ K. Crystallographically, SrRuO₃ has a distorted orthorhombic structure. Substitution of Ti⁺⁴ ($3d^0$) for Ru⁺⁴ ($4d^4$), however, does not introduce significant structural modification due to their matching ionic radii. This substitution, on the other hand, is expected to tune the electronic correlation effect and the d electron density in the system. With Ti substitution, we find that magnetic moment and Curie temperature decreases but T_c remains unchanged which has been attributed to opposite tuning of electron correlation effect and density of states within the framework of itinerant ferromagnetism. The estimated critical exponent (β) related to magnetization implies a mean-field type of magnetic nature in SrRuO₃. The value of β further increases with x which is understood from the dilution effect of magnetic lattice. The system evolves to exhibit Griffiths phase like behavior above T_c which is usually realized in diluted ferromagnet following local moment model of magnetism. Our detail analysis of magnetization data indicates that magnetic state in SrRuO₃ has contribution from both itinerant and local moment model of magnetism.

3.1 Introduction

Understanding the effect of disorder on ferromagnet (FM) is a long-standing issue in condensed matter physics. Of particular interest is itinerant ferromagnet which is realized in the framework of Stoner criterion, i.e., $UN(\epsilon_F) > 1$, where U is the intra-site Coulomb repulsion or electronic correlation energy, and $N(\epsilon_F)$ is the density of states (DOS) at Fermi level [1]. In fact, based on U the itinerant FMs are classified into weak and strong limit where the correlation effect is weak and strong, respectively. The prototype examples for weak itinerant FMs are ZrZn₂ [2], Ni₃Al [3], etc. while Fe is a well-known itinerant FM with strong correlation effect [4]. There are, however, many itinerant FMs where the strength of U falls in intermediate range. Therefore, introducing disorder in the form of chemical impurity, which is expected to tune either or both the U and $N(\epsilon_F)$ parameters, appears to be an effective route to understand the magnetism of original system.

The $4d$ based transition metal oxide SrRuO₃ is a commonly believed itinerant FM which has shown many interesting properties [5]. Usually, $4d$ transition metals have an intermediate strength of U and spin-orbit coupling (SOC) effect compared to its $3d$ and $5d$ counterparts which show prominent U and SOC, respectively. The SrRuO₃ crystallizes in orthorhombic symmetry with distorted perovskite structure (GdFeO₃ - type) where RuO₆ octahedra exhibit both tilt and rotation [6]. In spite of the large volume of studies, the nature of magnetism, as well as strength of U in this material, remains highly debated. This material has long-range ferromagnetic transition temperature $T_c \sim 162$ K. However, the magnetic moment even measured in the high magnetic field ($1.4 \mu_B/\text{f.u.}$) turns out lower than its calculated spin-only value $2 \mu_B/\text{f.u.}$ [6]. Electrical transport data show throughout metallic behavior though there is a slope change in resistivity around T_c due to reduced spin fluctuation [7]. The x-ray photoemission spectroscopy (XPS) study reports U is significantly weak in SrRuO₃ [8]. On the other hand, experimental studies, for instance, photoemission spectroscopy (PES) [9, 10], angle-resolved photo emission spectroscopy (ARPES) [11], optical spectroscopy [12] have shown non-negligible strength of U which is in favor of local moment behavior. A recent band theory calculation employing combination of density functional theory (DFT) and dynamical

mean-field theory (DMFT) has shown weak itinerant type FM behavior below T_c and local residual magnetic moment behavior above T_c , indicating a dual presence of weak itinerant and local moment behavior in SrRuO₃ [13]. With this picture, it is required to understand the nature of magnetism in SrRuO₃ more clearly, and introducing the chemical impurity to tune $N(\epsilon_F)$ and U would be an efficient route in this regard. Recently, a drastic variation of T_c with film thickness has been shown for SrRuO₃ which has been attributed to the change in $N(\epsilon_F)$ in ultrathin films of this material [19].

In this study, we report an evolution of structural and magnetic properties in SrRu_{1-x}Ti_xO₃ ($x \leq 0.7$) where the substitution of nonmagnetic Ti⁺⁴ (3d⁰) for Ru⁺⁴ (4d⁴) amounts to dilution of the magnetic network (Ru-O-Ru) in the original system. There have been several experimental and theoretical studies [8, 10, 14-18] investigating transport and electronic properties in SrRu_{1-x}Ti_xO₃ but the evolution magnetic properties have not been looked yet in details. The introduction of Ti⁺⁴, on the other hand, is less likely to induce any major structural modification as both the elements have very close ionic radii (Ru⁺⁴ = 0.62 Å and Ti⁺⁴ = 0.605 Å). Following this substitution of Ti⁺⁴, one can expect an increase in U and depletion of electrons in the original system due to its 3d⁰ character. These changes in U and $N(\epsilon_F)$ will definitely influence the magnetic behavior according to the itinerant model of FM. In fact, PES study has shown that along with a coherent peak there is a presence of incoherent peak below the Fermi level in SrRuO₃, which implies a presence of non-negligible U [10]. This study further shows that, with increasing x , the ratio between incoherent and coherent peaks increases and the DOS at Fermi level $N(\epsilon_F)$ depletes. Band structure calculation employing $GGA + U$ technique has also shown an increase of U with Ti substitution [17]. On the other hand, following the picture of a local spin model of FM the dilution of spin interaction along Ru-O-Ru bond would modify the T_c as well as magnetic moment. This dilution may further induce Griffiths phase [20] behavior above T_c as has been observed in Sr_{1-x}Ca_xRuO₃ where the dilution is realized due to suppression of Ru-O-Ru bond angle with Ca doping [21].

Our studies show that the original orthorhombic structure is retained with Ti substitution in SrRu_{1-x}Ti_xO₃ (x up to 0.7) though structural parameters modify with x . While the T_c remains almost unchanged in this series, we find both magnetic moment and

Curie temperature decrease with x . For undoped SrRuO₃, the critical exponent (β) related to magnetization shows value close to the mean-field model which increases with Ti reaching about 1 for the highest doped sample ($x = 0.7$). Furthermore, the doped samples exhibit GP like behavior above T_c where the behavior is prominently observed for $x \geq 0.4$. The analysis of thermal demagnetization data both itinerant and local-moment type of magnetism is present in SrRuO₃.

3.2 Experimental Details

Polycrystalline samples of SrRu_{1-x}Ti_xO₃ with $x = 0.0, 0.1, 0.2, 0.3, 0.4, 0.5$ and 0.7 have been prepared using solid-state route. The ingredient powder materials of SrCO₃, RuO₂ and TiO₂ with phase purity greater than 99.99 % (Sigma-Aldrich) are taken in stoichiometric ratio and ground well. The mixed powders are heated in air at 1000 °C for 24 h with for two times with an intermediate grinding. The calcined powders are then palletized and sintered at 1100 °C and 1150 °C for 36 h each time with an intermediate grinding. The phase purity of the samples is checked using powder x-ray diffraction (XRD) with a Rigaku MiniFlex diffractometer with CuK α radiation. The data have been collected in 2θ range of 10–90° at a step of 0.02°. To understand the structural evolution in this series, XRD data have been analyzed with Rietveld refinement program. DC magnetization (M) measurement is done using a superconducting quantum interference device (SQUID) magnetometer (Quantum Design).

3.3 Results and Discussions

3.3.1 Structural study

Figure 3.1 shows room temperature XRD pattern for SrRu_{1-x}Ti_xO₃ series with $x = 0.0, 0.1, 0.2, 0.3, 0.4, 0.5$ and 0.7 . The XRD pattern with diffraction peaks for the parent material ($x = 0.0$) matches well with the reported study [21]. With this substitution of Ti for Ru, major structural modification is not expected considering their matching ionic radii (Ru⁺⁴ = 0.62 Å and Ti⁺⁴ = 0.605 Å). Indeed, Figure. 3.1 shows XRD pattern does not modify significantly with x except a peak at $2\theta \sim 40^\circ$, which is minimally present in $x = 0$ compound, its intensity gradually increases with Ti. The XRD pattern has been analyzed using Rietveld refinement program [22].

Figure 3.2 shows representative XRD data along with Rietveld refinement for two end members of this series i.e., $x = 0.0$ and 0.7 . The refinement shows material with $x = 0$ (SrRuO₃) crystallizes in orthorhombic structure with $Pbnm$ symmetry [Figure 3.2(a)]. For the present SrRu_{1-x}Ti_xO₃ series, earlier studies have shown different evolution of structural phase with increasing amount of Ti. For instance, Cuffini *et al.* [23] have shown that crystallographic structure changes from orthorhombic ($x = 0$) to cubic phase with x between 0.4 and 0.5.

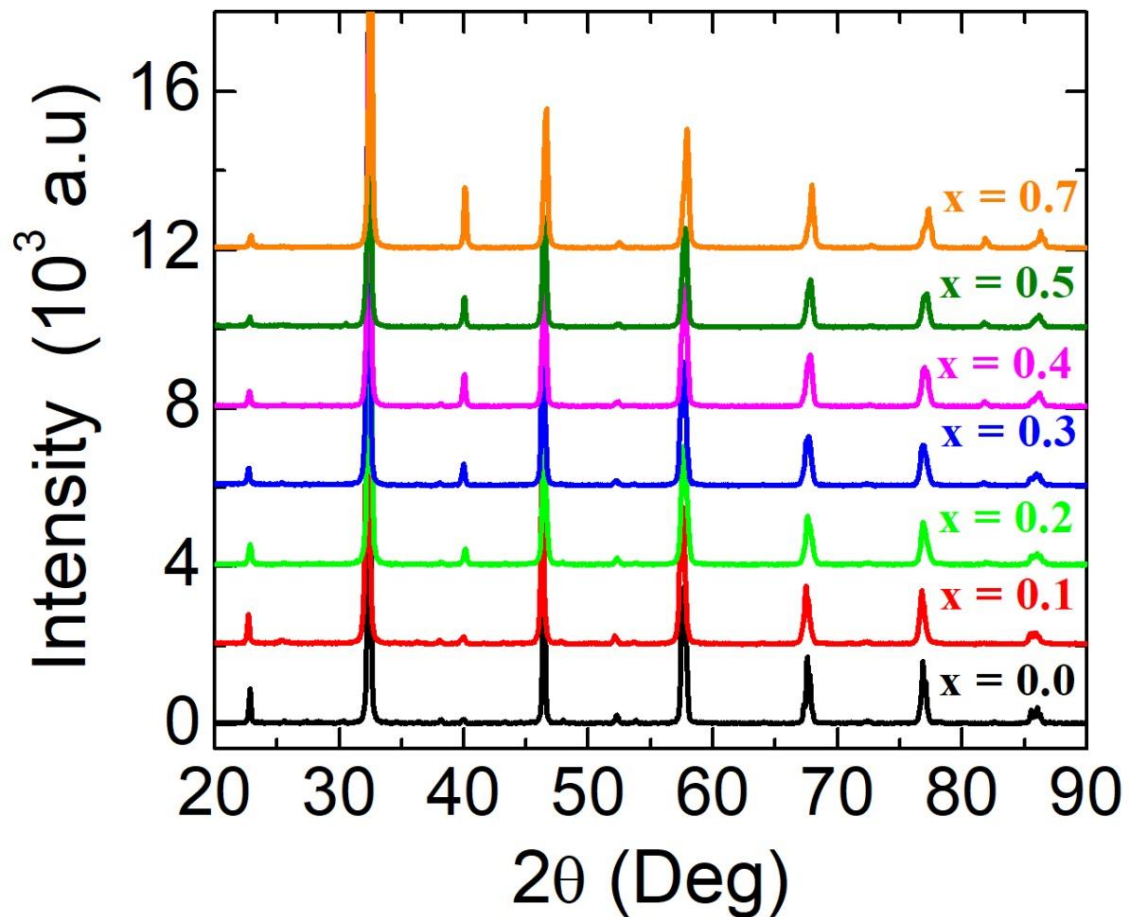


Figure 3.1 Room temperature XRD pattern of SrRu_{1-x}Ti_xO₃ series.

Bianchi *et al.* [16] have shown that the system retains its orthorhombic structure till $x = 0.6$ and above this, it changes to the tetragonal structure and finally changes to cubic structure for $x > 0.7$. Recently, Jang *et al.* [24] has reported a single-phase orthorhombic structure up to $x = 0.1$, then double-phase structure (orthorhombic and cubic) till $x = 0.5$

and after that a single-phase cubic structure for $x > 0.5$. A single-phase orthorhombic structure has also been shown for x up to 0.6 [8].

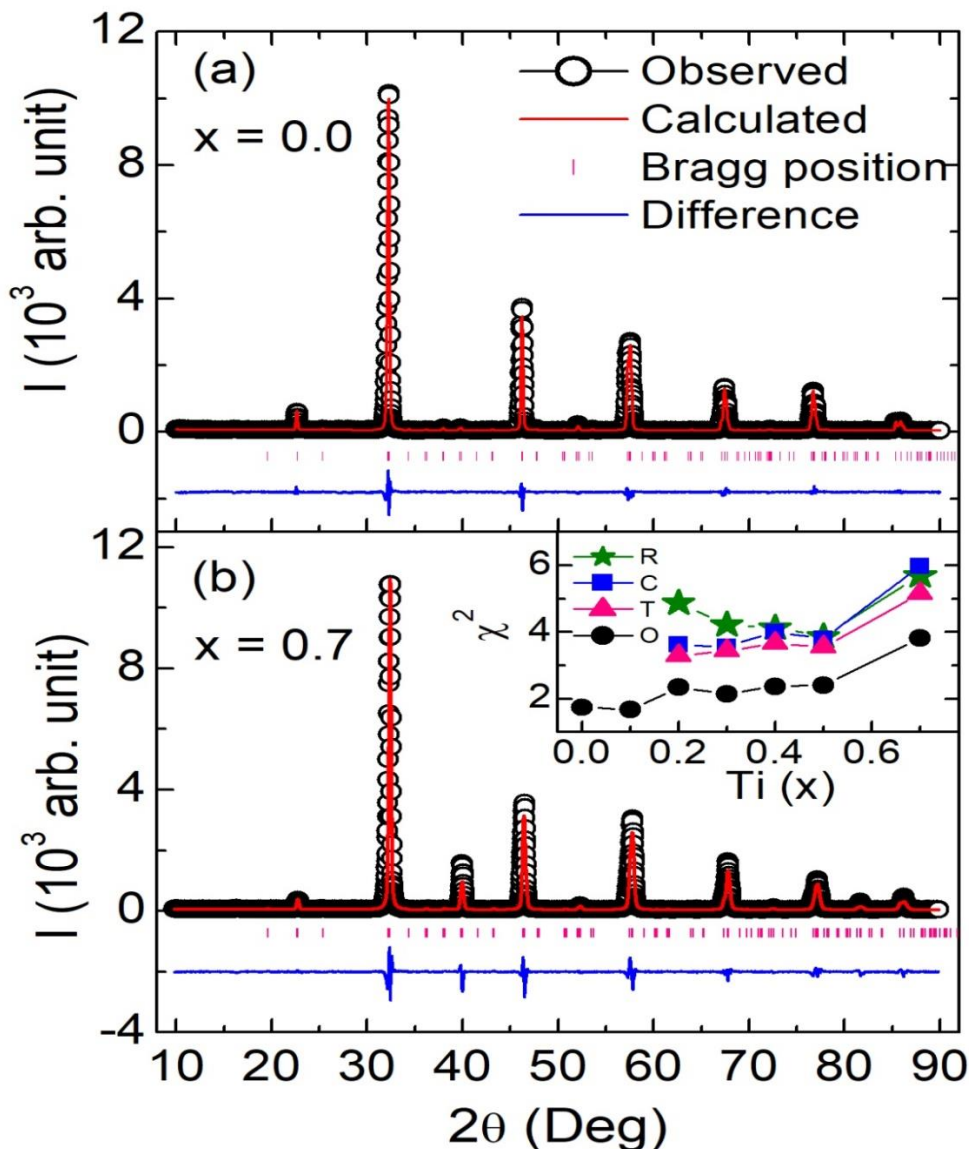


Figure 3.2 The room temperature XRD pattern along with Rietveld refinement taking orthorhombic- $Pbnm$ structure has been shown for (a) SrRuO₃ and (b) SrRu_{0.3}Ti_{0.7}O₃. Inset in (b) shows χ^2 value of Rietveld fitting for SrRu_{1-x}Ti_xO₃ series with rhombohedral (R), cubic (C), tetragonal (T) and orthorhombic (O) structure.

For all the materials in the present SrRu_{1-x}Ti_xO₃ series with $x \leq 0.7$, we have tried to analyze the XRD data with all possible orthorhombic ($Pbnm$), tetragonal ($I4/mcm$), rhombohedral ($R\bar{3}c$) and cubic ($Pm\bar{3}m$) structure using Rietveld refine program. For

SrRuO₃ [Figure 3.2(a)], we find an orthorhombic structure with *Pbnm* symmetry which is in agreement with majority of earlier studies [6, 7, 16, 23, 24]. With Ti substitution (x up to 0.7), we find the same orthorhombic-*Pbnm* structure is the best fitted one for whole series. While it has been previously shown that there is a phase transition from orthorhombic structure to more symmetric tetragonal or cubic structure above x in range of 0.5 or 0.7 [16, 23], but we observe that original orthorhombic structure continues to be the best fitted structural phase till $x = 0.7$ in this series.

For completeness, statistical goodness of fit, which is gauged by χ^2 value in Rietveld refinement, has been given for whole series as found with orthorhombic, tetragonal, rhombohedral and cubic structure in inset of Figure 3.2(b). As evident in figure, Rietveld refinement with orthorhombic structure gives the lowest χ^2 value for whole series with x up to 0.7. Figure 3.2(b) displays XRD pattern with Rietveld refinement with orthorhombic-*Pbnm* structure for SrRu_{0.3}Ti_{0.7}O₃ showing reasonably good fitting of data. Here it can be mentioned that where other studies have reported structural phase transition from original orthorhombic structure around 50 to 70% of Ti substitution in SrRu_{1-x}Ti_xO₃ series [16, 23], our results demonstrating continuity of orthorhombic structure till 70% of Ti concentration is in conformity with earlier results. Moreover, considering the matching ionic radii as well as the ionic state of Ru and Ti, it is more likely that doped SrRu_{1-x}Ti_xO₃ materials will produce single and homogeneous structural phase rather than a situation of phase coexistence.

Figure 3.3 shows composition dependent evolution of lattice parameters i.e., a , b , c and volume V related to orthorhombic-*Pbnm* phase for the present SrRu_{1-x}Ti_xO₃ series. It is seen in the figure that lattice parameters as well as volume decrease with Ti concentration, except the parameter c which initially increases with x . The decrease of volume with Ti concentration can be explained with reduced ionic size of Ti⁴⁺ compared to Ru⁴⁺, and the similar behavior has also been observed by Cuffini *et al.* [23]. As expected, Ti substitution has not occurred any major structural modification as for the maximum doped ($x = 0.7$) sample structural parameters (Figure 3.3) modify only in the range of (0.2 - 0.5%).

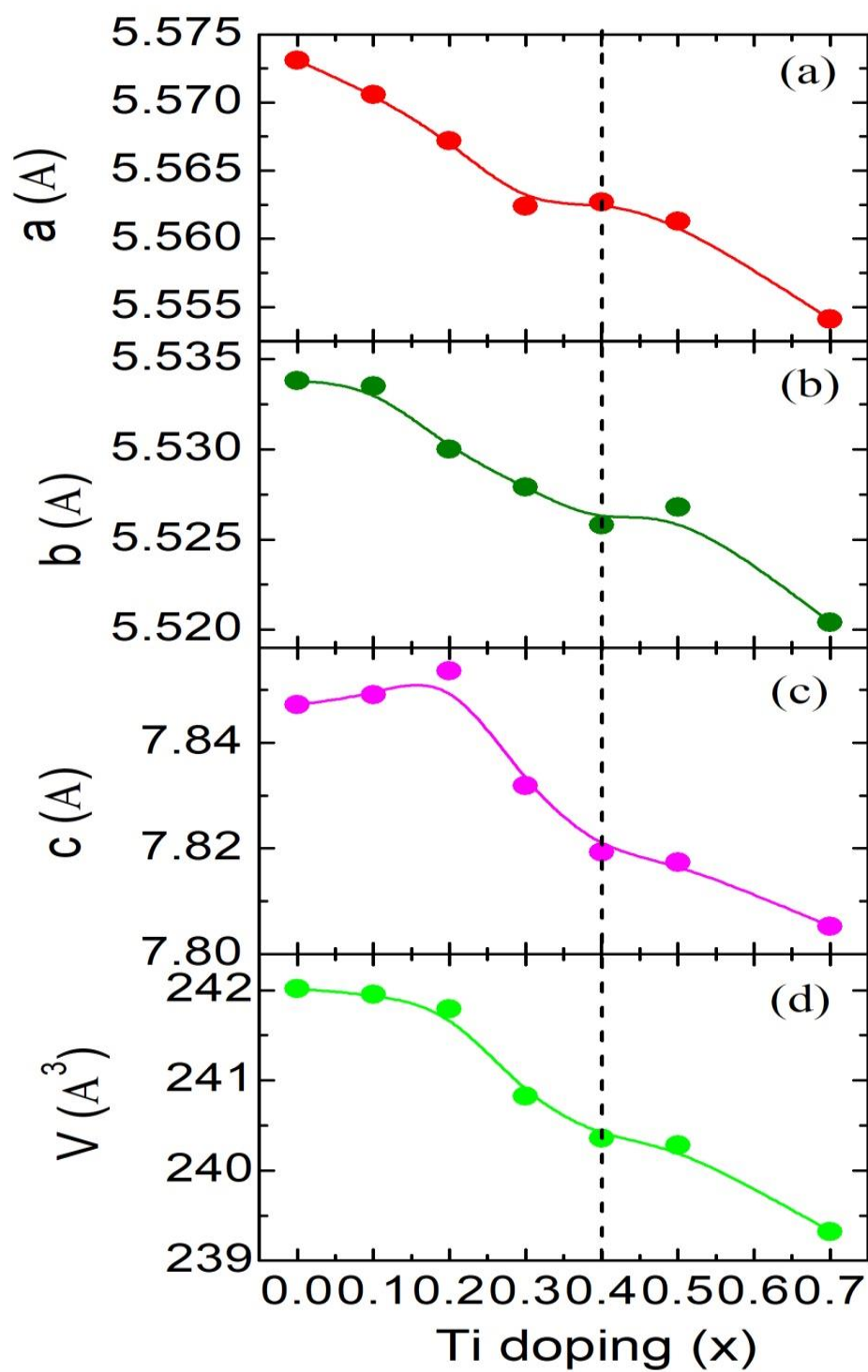


Figure 3.3 Unit cell parameters (a) a , (b) b , (c) c and (d) volume V as determined from Rietveld analysis using room temperature XRD data have been shown with Ti concentration (x) for SrRu_{1-x}Ti_xO₃. Lines are guided to eyes.

3.3.2 Zero field cooled and field cooled magnetization data

Temperature dependent magnetization data measured in 100 Oe magnetic field following zero field cooled (ZFC) and field cooled (FC) protocol for series SrRu_{1-x}Ti_xO₃ have been shown in figure 3.4. Figure 3.4(a) shows $M(T)$ for samples with $x = 0.0, 0.1, 0.2$ and 0.3 and the Figure 3.4(b) shows the same for $x = 0.4, 0.5,$ and 0.7 . The insets of both the figures show ZFC magnetization data in the limited temperature range. It is seen in Figure 3.4(a) that ZFC and FC branches of magnetization data for parent compound with $x = 0.0$ bifurcates at temperature ~ 162 K.

The inset of Figure 3.4(a) shows M_{ZFC} for $x = 0.0$ shows a peak around this temperature which is believed to be the ferromagnetic ordering temperature T_c in this material. The large bifurcation between M_{FC} and M_{ZFC} indicates the material SrRuO₃ has large anisotropy. With dilution of magnetic lattice in SrRuO₃ by substitution of nonmagnetic Ti⁴⁺, the magnetization data in Figure 3.4 is quite interesting. For samples with $x = 0.0, 0.1, 0.2$ and 0.3 , the bifurcation temperature between M_{ZFC} and M_{FC} as well as peak temperature in M_{ZFC} remains almost same though the value of M_{FC} decreases. The similar features are also observed for higher doped samples ($x = 0.4, 0.5$ and 0.7) as evident in Figure 3.4(b). It is rather intriguing that site dilution in terms of substitution of Ti⁴⁺ at Ru⁴⁺ site decreases the moment but the ferromagnetic ordering temperature T_c appears to remain unchanged.

Table 3.1 The characteristic temperatures T_c , T_c^R and T_G are given for SrRu_{1-x}Ti_xO₃ series.

Samples (x)	T_c (K)	T_c^R (K)	T_G (K)
0.0	162.7		
0.1	162.6		
0.2	162.9		
0.3	162.6		
0.4	162.6	162.7	170.6
0.5	162.9	160.7	169.4
0.7	162.9	161.3	169.9

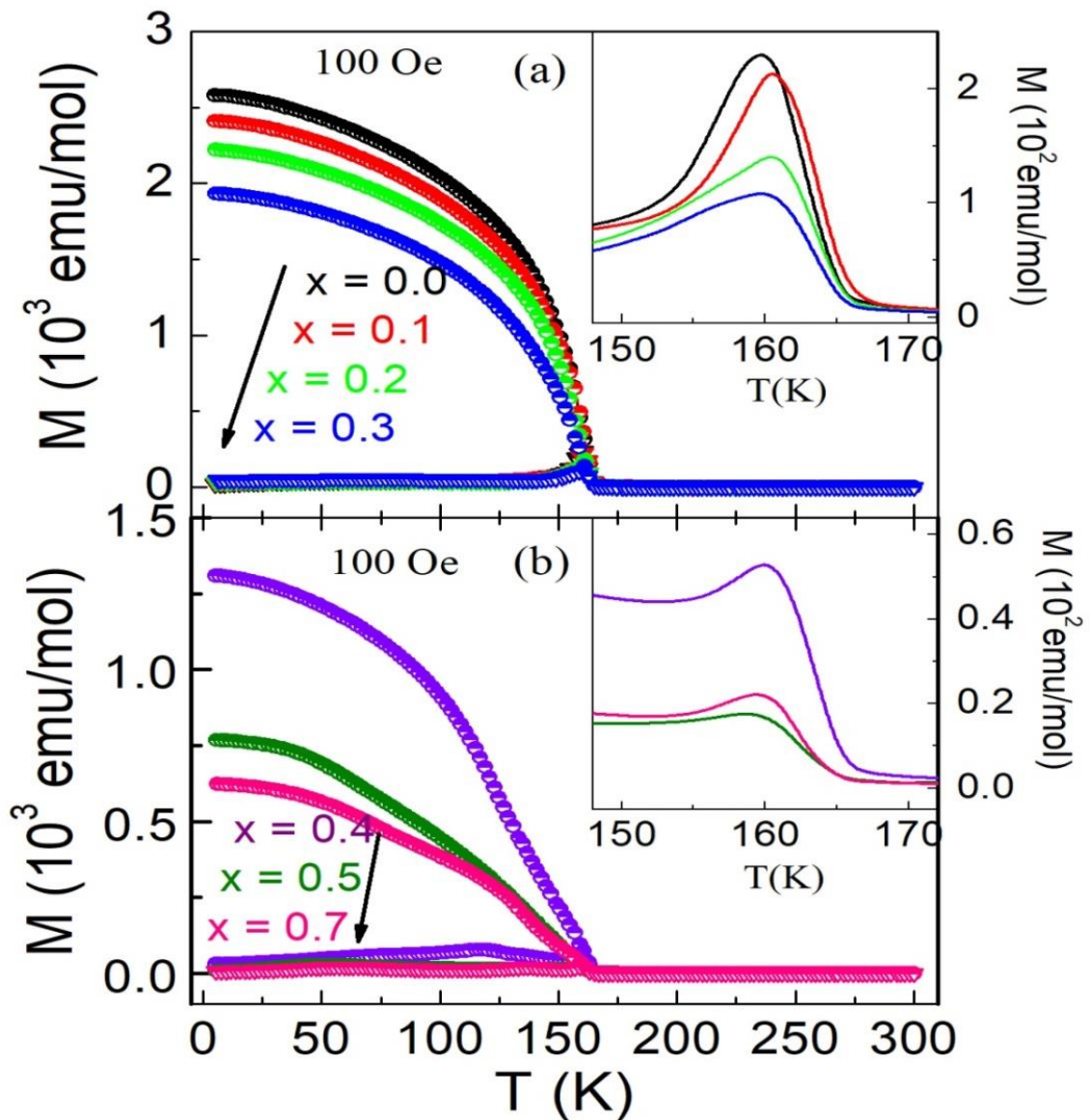


Figure 3.4 Temperature dependent magnetization data measured in 100 Oe following ZFC and FC protocol have been shown for $\text{SrRu}_{1-x}\text{Ti}_x\text{O}_3$ series with (a) $x = 0.0, 0.1, 0.2, 0.3$ and (b) $x = 0.4, 0.5, 0.7$. Insets show the zero field cooled magnetization data in expanded scale close to T_c .

3.3.3 Thermal demagnetization study

To understand the magnetic nature of SrRuO_3 in further detail, we have analyzed the low temperature magnetization rather demagnetization data. Figure 3.4 shows at low temperature $M_{\text{FC}}(T)$ continuously decreases with temperature. This thermal

demagnetization can be explained both within the scenario of localized as well as itinerant model of spin interaction. In the localized model, the thermal demagnetization of $M(T)$ occurs due to excitation of spin-wave (SW) where the magnetization decreases following Bloch law as [31];

$$M(T) = M(0)[1 - BT^{3/2}] \quad (3.1)$$

where $M(0)$ is the magnetization at 0 K, and B is the coefficients. The spin-wave stiffness constant D can be calculated as;

$$D = \frac{k_B}{4\pi} \left[\frac{2.612g \mu_B}{M(0)\rho B} \right]^{2/3} \quad (3.2)$$

where k_B is the Boltzmann constant and ρ is the density of material.

On the other hand, in itinerant or band model of magnetism, the origin of magnetization is considered to arise due to the displacement between spin-up and spin-down sub-band. The thermal demagnetization in this model is explained with the excitation of electron from one sub-band to another one. For strong itinerant type of FM, where one sub-band is completely filled and another one is partially filled, the single-particle excitation or thermal demagnetization is described as;

$$M(T) = M(0) \left[A T^{3/2} e^{\left(-\frac{\Delta}{k_B T} \right)} \right] \quad (3.3)$$

where A is the coefficient, k_B is the Boltzmann constant and Δ is the energy gap between the top of full sub-band and Fermi level. For the weak itinerant, where both the sub-bands are partially filled and have empty states at Fermi level, the single-particle excitation follows as;

$$M(T) = M(0)[A T^2] \quad (3.4)$$

where A is the coefficient. However, the simultaneous presence of both localized and itinerant model in same material is possible.

In an aim to understand the nature of magnetism vis-à-vis thermal demagnetization process in SrRu_{1-x}Ti_xO₃, we have analyzed the $M_{FC}(T)$ data (Figure 3.4) with the above discussed models. The fitting with only Eq. (3.1) for the spin-wave model has not given good fitting. Regarding single-particle model, the Eq. (3.3) cannot be a valid model for thermal demagnetization as the spin polarization for SrRuO₃ is much lower than

100% [32, 33]. Similarly, Eq. (3.4) alone did not give good result. Therefore, we have tried to fit the magnetization data taking combination of Eq. (3.1) and (3.4). The inset of Figure 3.5 shows $M_{FC}(T)$ data along with fitting with combination of Eq. (3.1) and (3.4) i.e., with $M(T) = M(0) [1 - BT^{3/2} - AT^2]$ up to temperature range $0.4 T_c$ for SrRuO₃. We obtain fitting parameters as, $M(0) = 0.463 \mu_B/\text{f.u.}$, $B = 9.0 \times 10^{-5} \text{ K}^{-3/2}$ and $A = 1.17 \times 10^{-5} \text{ K}^{-2}$. These obtained values of coefficient B and A match well with the earlier reported values [34]. Using Eq. (3.2), we have calculated spin wave stiffness constant $D = 264.9 \text{ meV}\text{\AA}^2$. Furthermore, exchange coupling constant (J) between nearest-neighbor magnetic atoms has been calculated to be $37.6 k_B\text{K}$ following $B = (0.0587/S)[(k_B)/(2SJ)]^{3/2}$ where $S (=1)$ is the localized atomic spin [31].

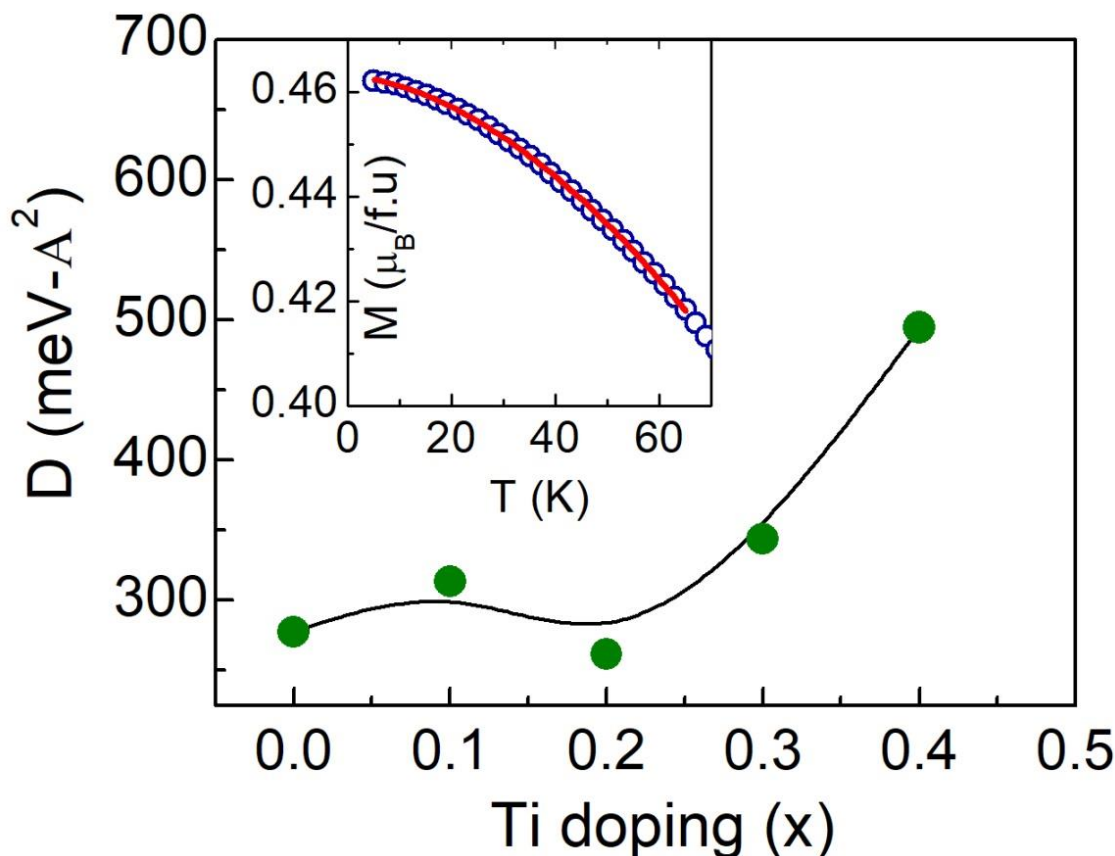


Figure 3.5 Spin-wave stiffness constant D as a function of Ti doping concentration. Inset shows fitting of magnetization data using Eq. (3.1) and (3.4).

For the doped materials, we have analyzed demagnetization data and estimated stiffness constant D following the above mentioned procedure for x up to 0.4. For the materials with $x > 0.4$, the magnetic lattice is so diluted that analysis did not yield good result. The estimated D has been shown in main panel of Figure 3.5 which shows its value increases with x . Given that T_c remains constant and also the number of nearest neighbor magnetic atoms decreases with replacing magnetic Ru⁺⁴ by nonmagnetic Ti⁺⁴, this increase of D is quite interesting. Though it needs further investigation, we explain this increase of D primarily due to the fact that Ti severs the Ru-O-Ru magnetic channel for the propagation of spin-waves; hence the stiffness constant value increases.

3.3.4 Nature of magnetic state and critical exponent for temperature dependent magnetization

The nature of magnetic interaction in FM is usually characterized by set of critical exponents associated with different universality classes [28]. These universality classes are decided by the dimensionality of lattice (d) and the dimensionality of the spin system (n) where they do not depend on the microscopic details of the system. For the present series of samples, we have extracted the critical exponent β which is related with the temperature dependent magnetization near T_c as following,

$$M = M_0(T_c - T)^\beta \quad (3.5)$$

The inset of Figure 3.6 shows representative fitting of M_{FC} data of SrRuO₃ near T_c (up to $\sim 0.8T_c$) using Eq. (3.5), where M_0 , T_c and β have been kept as free fitting parameters. This fitting gives exponent $\beta = 0.48(2)$. This value of β is very close to the theoretically predicted value (0.5) for mean-field spin interaction model. Moreover, this value is consistent with the other report showing spin interaction in SrRuO₃ follows mean-field model [29]. The obtained T_c is also close to the value estimated from temperature derivative of ZFC magnetization (table 3.1).

The main panel of Figure 3.6 shows composition dependent evolution of β . The figure shows that value of β increases with Ti substitution reaching close to 1.0 in highest doped material ($x = 0.7$). These values of β above 0.5, however, cannot be ascribed to any of the

known universality classes related to standard models. Nonetheless, this systematic evolution of exponent β with Ti substitution is quite intriguing. The similar evolution of β has also been observed for isovalent doped Sr_{1-x}Ca_xRuO₃ [29].

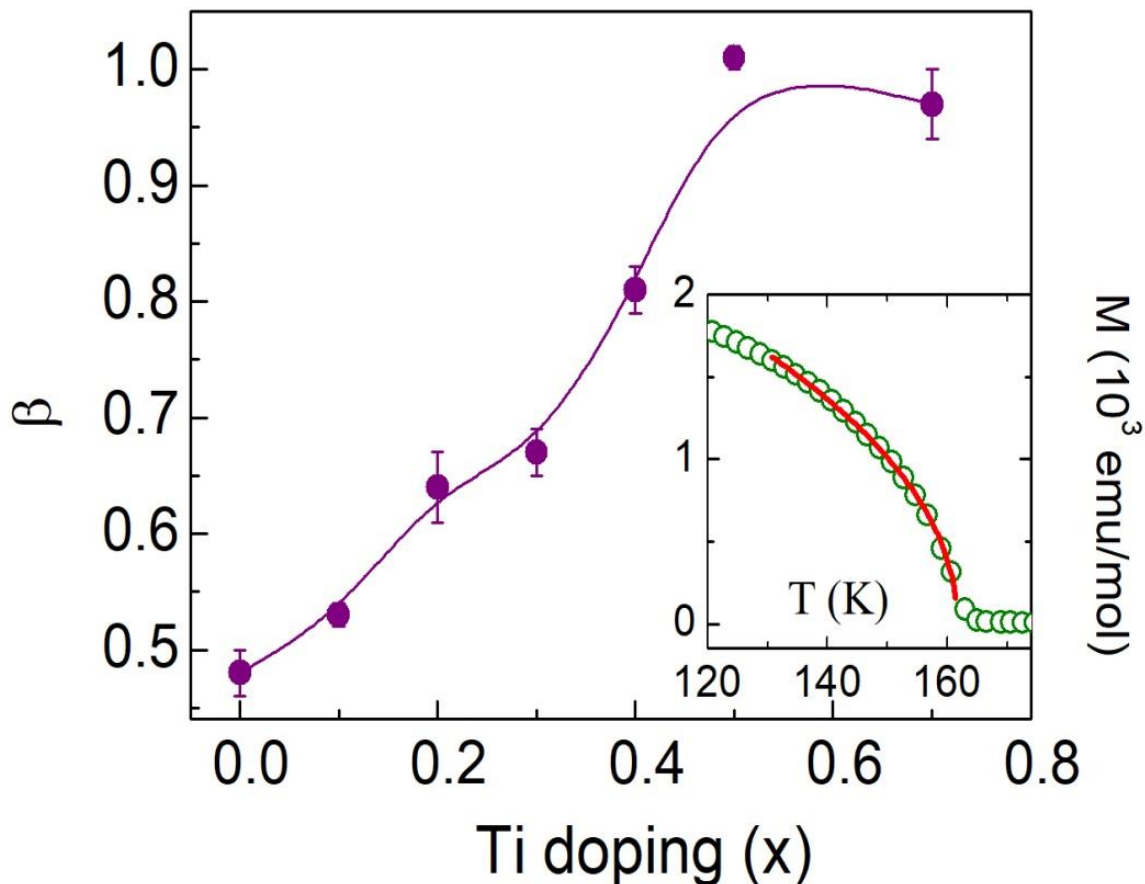


Figure 3.6 The evolution of critical exponent β (Eq. 3.5) with x has been shown for SrRu_{1-x}Ti_xO₃ series. Inset shows field cooled magnetization data along with fitting due to Eq. (3.5).

In case of Sr_{1-x}Ca_xRuO₃, FM is weakened with Ca substitution and T_c is completely suppressed at $x \sim 0.7$ [6, 29]. This increase of exponent β has been related to phase segregation between strongly coupled regimes surrounded by regimes with diluted FM spin-spin interaction [29]. This is supported by the fact that $\chi^{-1}(T)$ above T_c in Sr_{1-x}Ca_xRuO₃ exhibit anomalous behavior showing Griffiths singularity which is characterized by preformed FM clusters in PM state [21]. It is worthy to note that with substitution of another isovalent ion Ba²⁺, which has higher ionic radii than Sr²⁺, in Sr_{1-x}Ba_xRuO₃ the exponent β decreases and the end member BaRuO₃ shows exponents in

agreement with 3D Heisenberg interaction where $\chi^{-1}(T)$ shows conventional Curie-Weiss type behavior ($T_c \sim 60$ K) [21, 30]. In present SrRu_{1-x}Ti_xO₃, however, site dilution by Ti substitution results in a situation where the ferromagnetically aligned clusters surrounded by nonmagnetic matrix evolves and the size of those clusters increasingly decreases with substitution. This is evident within Figure 3.5 where the GP behavior is strengthened with x . It is interesting to see the similar type of evolution of critical exponent β with the chemical substitution both at Sr- and Ru-site.

3.3.5 Griffiths phase behavior

Figure 3.7 shows temperature dependence of inverse susceptibility [$\chi^{-1} = (M/H)^{-1}$] for the selected samples with $x = 0.0, 0.3, 0.4, 0.5$ and 0.7 for SrRu_{1-x}Ti_xO₃ series. The figure shows that $\chi^{-1}(T)$ shows fairly linear behavior at high temperature above T_c following Curie-Weiss (CW) behavior (discussed later). However, the $\chi^{-1}(T)$ shows a sharp downfall immediately above T_c for higher doped samples which indicates CW behavior is exactly not followed in this temperature regime. This sudden and sharp downfall in $\chi^{-1}(T)$ in the vicinity of T_c is understood with the scenario of the Griffiths phase (GP) behavior which is caused by phase inhomogeneity above T_c [20]. The GP was originally discussed for the diluted using ferromagnet with random distribution of nearest-neighbor exchange constant J and 0 having probability p and $1-p$, respectively. It has been shown that for p less than critical value p_c , long-range FM ordering cannot survive in the system. For $1 \geq p \geq p_c$, system can have long-range magnetic ordering although transition temperature $T_c(p)$ is lower than that $T_c(p = 1)$ of undiluted system. Conventionally, the $T_c(p = 1)$ is called the Griffiths temperature T_G which is determined as the temperature where $\chi^{-1}(T)$ starts to deviate from linear behavior in high temperature PM state. The temperature range between T_G and $T_c(p)$ is called Griffiths phase regime where the system exhibit neither perfect FM ordering nor PM behavior. Rather, there exist ferromagnetically ordered finite size clusters embedded in PM background. Due to the presence of clusters, magnetization shows nonanalytic behavior. As a result, susceptibility diverges which is demonstrated by sharp downturn in $\chi^{-1}(T)$ [25, 26].

The $\chi^{-1}(T)$ data in Figure 3.7(a) shows a sudden and sharp downturn immediately above T_c for higher doped samples which is prominent for $x > 0.3$. This behavior qualitatively shows GP like behavior which is reinforced with site dilution. In a quantitative manner, Griffiths singularity is characterized by the following relation [27];

$$\chi^{-1} = (T - T_c^R)^{1-\lambda} \quad (3.6)$$

where λ is the exponent ($0 < \lambda \leq 1$) and T_c^R is the random critical temperature at which the magnetic susceptibility tend to diverge. This Eq. (3.6) is a modified form of Curie-Weiss law for which $\lambda = 0$. The finite value of λ arises due to the formation of FM clusters in PM regime, therefore, higher the value of λ stronger is the GP behavior. Figure 3.7(b) shows \log_{10} - \log_{10} plot of Eq. (3.6) for samples with $x = 0.4, 0.5$ and 0.7 where the GP behavior is prominently observed in Figure 3.7(a). The straight lines in low temperature GP regime [Figure 3.7(b)] are due to fitting following Eq. (3.6) which is an indicative of Griffiths singularity in these materials. These straight line fittings give values of exponent λ as 0.46, 0.72 and 0.75 and values of T_c^R as 162.7, 160.8 and 161.3 K for $x = 0.4, 0.5$ and 0.7 , respectively. The obtained T_c^R values are quite close to respective T_c (~ 163 K) of these three materials. The T_G which is usually determined as an onset temperature for downturn in $\chi^{-1}(T)$ [26], interestingly, has been found to be ~ 166.8 K for all the samples, in that sense GP regime ($T_G - T_c$) is relatively narrow in present samples. The increasing value of exponent λ with x implies GP behavior is strengthened with site dilution effect.

We have further examined the GP behavior in varying magnetic fields. Figure 3.7(c) shows $\chi^{-1}(T)$ for representative $x = 0.5$ sample in magnetic field 100 and 1000 Oe. It is seen in figure that downturn in χ^{-1} across T_c is reduced with increasing field. This can be explained as in higher fields the magnetic response from paramagnetic background becomes substantial to dominate over that from magnetic clusters. This leads to weakening of divergence of susceptibility and the $\chi^{-1}(T)$ tends to be linear. The similar behavior has also been observed in many other materials [25, 26]. Figure 3.7(d) shows fitting of susceptibility data using Eq. (3.6) for $x = 0.5$ sample with 100 and 1000 Oe magnetic field similar to Figure 3.7(b). From straight line fitting, we obtain exponent $\lambda =$

0.72 and 0.78, and $T_c^R = 160.8$ and 161.4 K for field 100 and 1000 Oe, respectively. The T_c^R values are close to its T_c (~ 163 K), and increase with magnetic field.

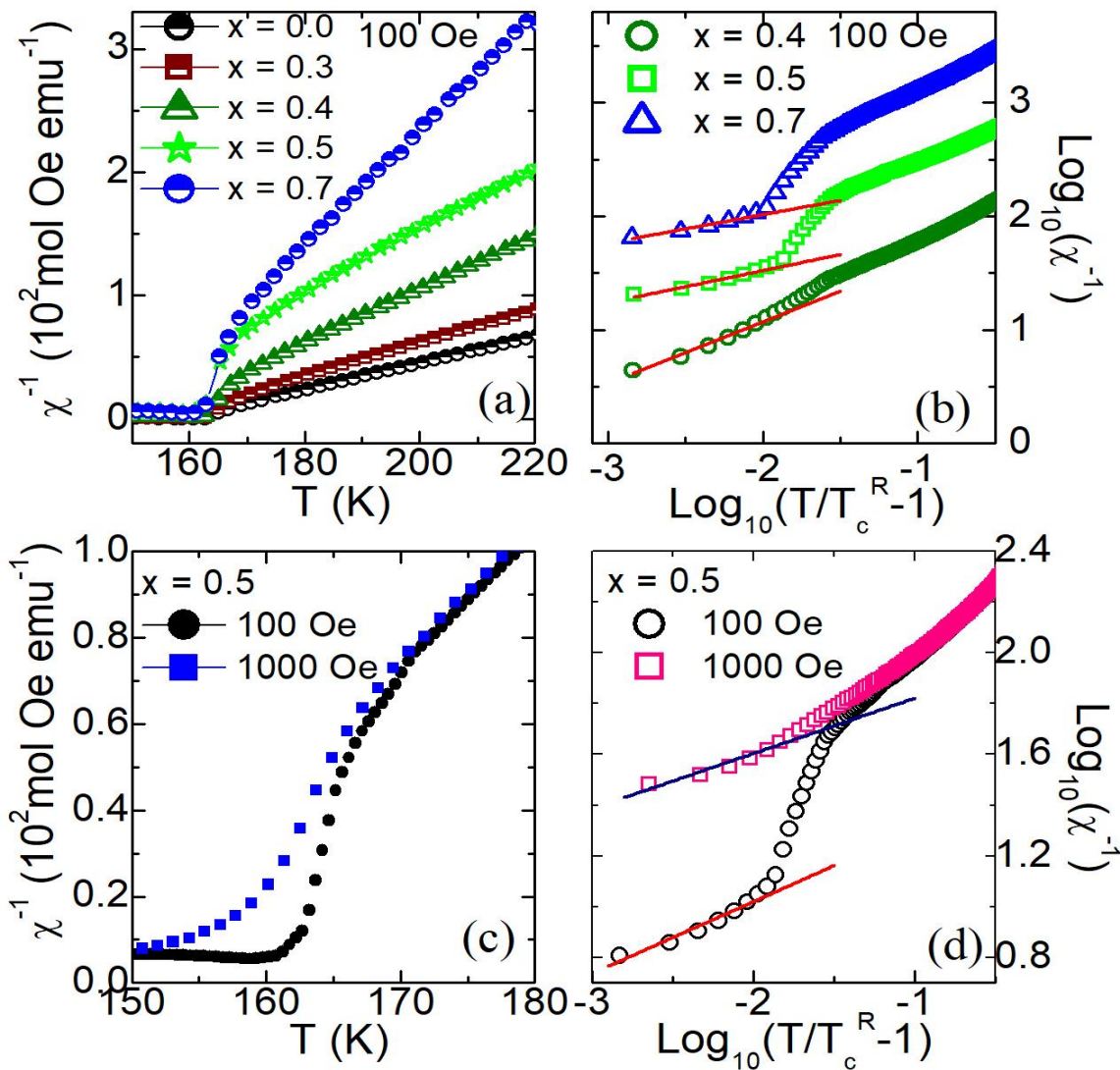


Figure 3.7 (a) Shows temperature dependence of inverse magnetic susceptibility for SrRu_{1-x}Ti_xO₃ series with $x = 0.0, 0.3, 0.4, 0.5$ and 0.7 . (b) Inverse susceptibility has been plotted following Eq. (3.6) on \log_{10} - \log_{10} scale with $x = 0.4, 0.5$ and 0.7 . (c) Shows inverse susceptibility for $x = 0.5$ sample in different magnetic fields. (d) Shows same plotting as in (b) for $x = 0.5$ sample with different magnetic fields. The straight lines in (b) and (d) are due to fitting with Eq. (3.6).

Here we mention that a close inspection in figure 3.7(a) reveals χ^{-1} for parent SrRuO₃ as well as for low doped samples (x up to 0.3) show a weak downturn across T_c which becomes more prominent above $x = 0.3$. While this downturn in χ^{-1} for these low doped

samples starts almost at the same temperature of higher doped samples ($T_G \sim 170$ K, see table 3.1), the fitting with Eq. (3.6) for χ^{-1} data, however, does not give good result, probably due to weak nature of GP behavior. For this reason, we have not reported GP characteristic temperatures i.e. T_c^R and T_G for low doped samples in table 3.1. While T_G is considered to be the FM ordering temperature of undiluted original system, the present T_G (~ 170 K) being slightly higher than the T_c (~ 163 K) of SrRuO₃ is not unusual as many parent materials are seen to show GP behavior where the essential disorder is realized coming from structural disorder or ionic mismatch [26]. For SrRuO₃, we observe very weak downturn in χ^{-1} because measurements are done in very low field (100 Oe) but the measurements done in high field (1000 Oe) do not show such behavior [21], as the effect of magnetic field on GP behavior is seen in figure 3.7(c). The appearance of GP behavior in present series is quite intriguing as the original SrRuO₃ is believed to be an itinerant type FM. However, signature of GP has been evidenced in isovalent doped Sr_{1-x}Ca_xRuO₃ which the authors have ascribed to the fact that suppression of Ru-O-Ru bond angle with Ca substitution dilutes FM interaction through Ru-O-Ru bonds, hence GP behavior is induced [21]. The GP picture is further supported by a recent band calculation using *DFT* and *DMFT* approach showing presence of both itinerant and local moment model of magnetism in SrRuO₃, particularly local type magnetic moment persists above T_c [13]. In this scenario, we believe that GP behavior arises as a consequence of site dilution which renders small size ferromagnetically aligned clusters above T_c . The sizes of clusters are further reduced with Ti substitution which is evident from increasing value of exponent λ . Nonetheless, observed GP behavior brings out the local moment aspect of SrRuO₃.

3.3.6 High temperature paramagnetic state and Curie-Weiss behavior

To understand the high temperature magnetic state, we have analyzed the magnetization data in terms of modified Curie-Weiss law;

$$\chi = \chi_0 + \frac{C}{T - \theta_P} \quad (3.7)$$

where χ is the magnetic susceptibility, χ_0 is the temperature independent susceptibility, C is the Curie constant and θ_P is the Curie temperature. The inset of Figure 3.8(a) shows

temperature dependence of inverse susceptibility χ^{-1} for SrRuO₃ in high temperature regime above T_c . The $\chi^{-1}(T)$ rather shows linear behavior in PM state.

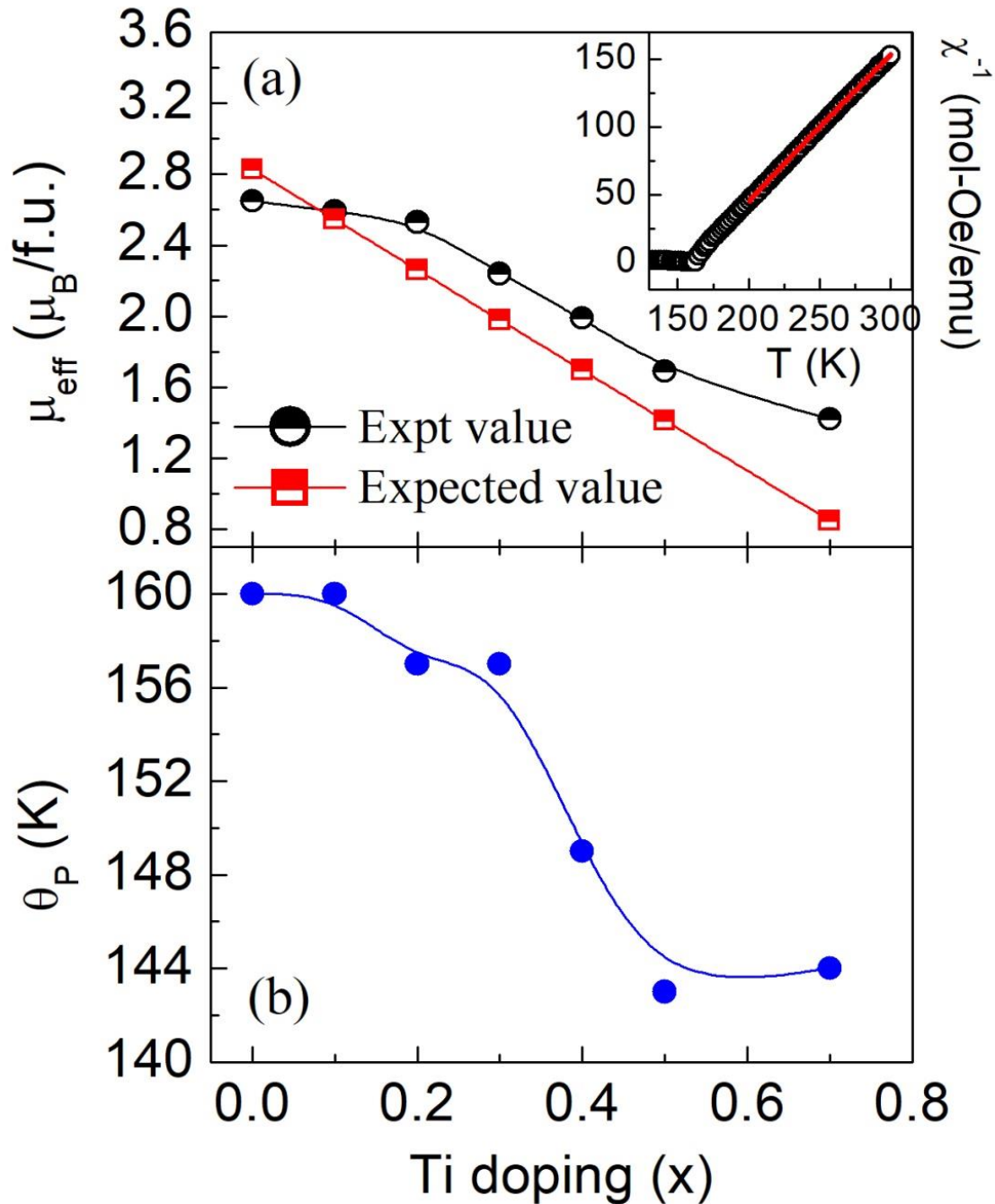


Figure 3.8 (a) The calculated and experimentally determined effective PM moment μ_{eff} have shown with x . The inset shows temperature dependent inverse susceptibility for SrRuO₃ and the straight line fitting due to Eq. (3.7), (b) shows Curie temperature θ_P against Ti concentration (Eq. 3.7).

The Eq. (3.7) has been fitted with $\chi^{-1}(T)$ data in temperature range between 200 to 300 K as shown in figure. The reasonably good fitting suggests magnetic susceptibility follows Curie-Weiss behavior. The fitting yields $\chi_0 = 2.56 \times 10^{-4}$ emu mole⁻¹ Oe⁻¹, $C = 0.88$ emu K mole⁻¹ Oe⁻¹ and $\theta_p = 160$ K. Using this obtained Curie constant C , the effective PM moment μ_{eff} has been calculated to be $2.65 \mu_B/\text{f.u.}$ This experimentally obtained value for μ_{eff} is close to the expected value $2.83 \mu_B/\text{f.u.}$ which has been calculated for spin-only moment $g\sqrt{S(S+1)} \mu_B$ with $S = 1$. These values of θ_p and μ_{eff} reasonably agree with other studies [6, 8]. We find Curie-Weiss behavior is followed for whole series of samples at high temperatures [Figure 3.7(a)]. Figure 3.8(a) shows composition dependent both experimentally observed and expected values of μ_{eff} for SrRu_{1-x}Ti_xO₃ series. As evident in figure, both values of μ_{eff} decreases with Ti substitution. While the expected value of μ_{eff} decreases linearly the observed μ_{eff} is not linear with x . Interestingly, the observed μ_{eff} is lower than the expected one for $x = 0$, but it crosses over around $x = 0.1$ and shows higher value with further increase of x . This can be explained from preformed FM clusters above T_c giving a higher value of μ_{eff} which is also corroborated with the GP behavior as seen in Figure 3.7. The value (160 K) of θ_p for SrRuO₃ turns out to be close to the bifurcation temperature (162 K) between M_{ZFC} and M_{FC} (Figure 3.4). Moreover, the positive value of θ_p shows spin interaction is of ferromagnetic in nature. The θ_p as a function of Ti concentration is plotted in Figure 3.8(b) which shows θ_p does not decrease significantly and remains positive with x up to 0.7. This underlines the fact that though FM ordering is weakened but it survives with nonmagnetic Ti⁺⁴ substitution as high as 70% which is in sharp contrast with isovalent doped Sr_{1-x}Ca_xRuO₃ where FM ceases to exist beyond 70% of Ca doping [6].

3.3.7 Magnetic field dependent magnetization study

The magnetic field dependent magnetization data collected at 5 K up to field 70 kOe have been shown in Figure 3.9. The undoped material SrRuO₃ shows a large hysteresis with coercive field~ 4800 Oe which matches with previous data [34]. At 70 kOe, the $M(H)$ data, however, do not saturate and continue to increase with smaller slope.

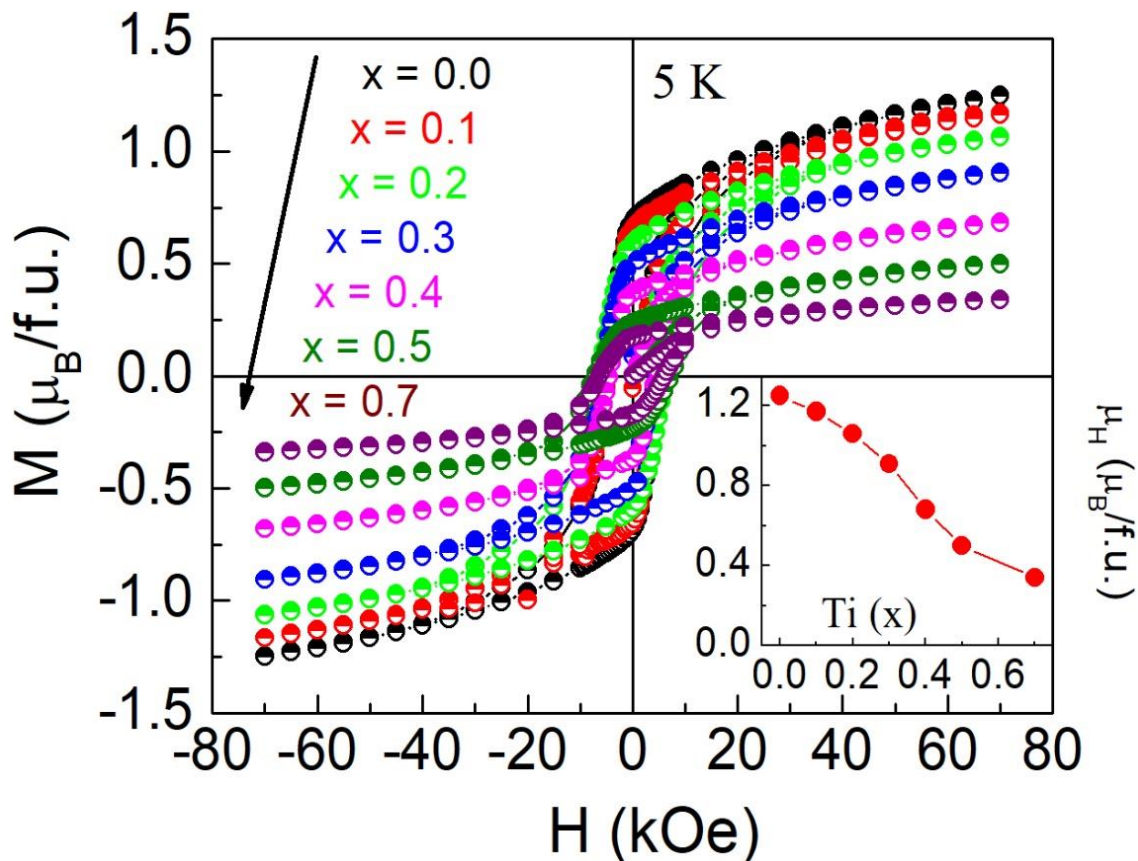


Figure 3.9 The isothermal magnetization data with field at 5 K are shown for SrRu_{1-x}Ti_xO₃ series. Inset shows value of moment at 70 kOe obtained from main panel with x .

At 70 kOe, we get moment μ_H about $1.25 \mu_B/\text{f.u.}$ which turns out smaller than the spin-only expected value $2 \mu_B/\text{f.u.}$ for total spin $S = 1$. Here, it can be mentioned that moment in SrRuO₃ does not attain its expected full value in magnetic field as high as 30 Tesla [6]. This low value of moment is believed to arise due to the itinerant magnetic character of SrRuO₃. With increasing substitution of Ti, the moment decreases (inset of Figure 3.9) though not linearly as expected from site dilution with nonmagnetic atom.

3.3.8 Analysis of Arrott plot and spontaneous magnetization

We have further analyzed the $M(H)$ data in terms of Arrott plot which is plotting of M^2 vs H/M [35]. The intercept of the slope in the Arrott plot, which basically gives moment at $H = 0$ and amounts to a spontaneous moment (M_s), is very useful to understand the magnetic nature of a material. While negative intercept implies a non-ferromagnetic

nature the positive value of intercept straightforwardly shows a ferromagnetic nature of material. Figure 3.10 shows Arrott plot of $M(H)$ data taken at 5 K for whole series. As evident in the figure, the intercept of slopes taken in high field regime gives positive values for all the samples which suggest ferromagnetic ordering survives till highest concentration of Ti substitution (70 %). Inset of Figure 3.10 shows estimated M_s against material composition (x) showing M_s decreases with Ti following a similar trend of μ_H in Figure 3.9.

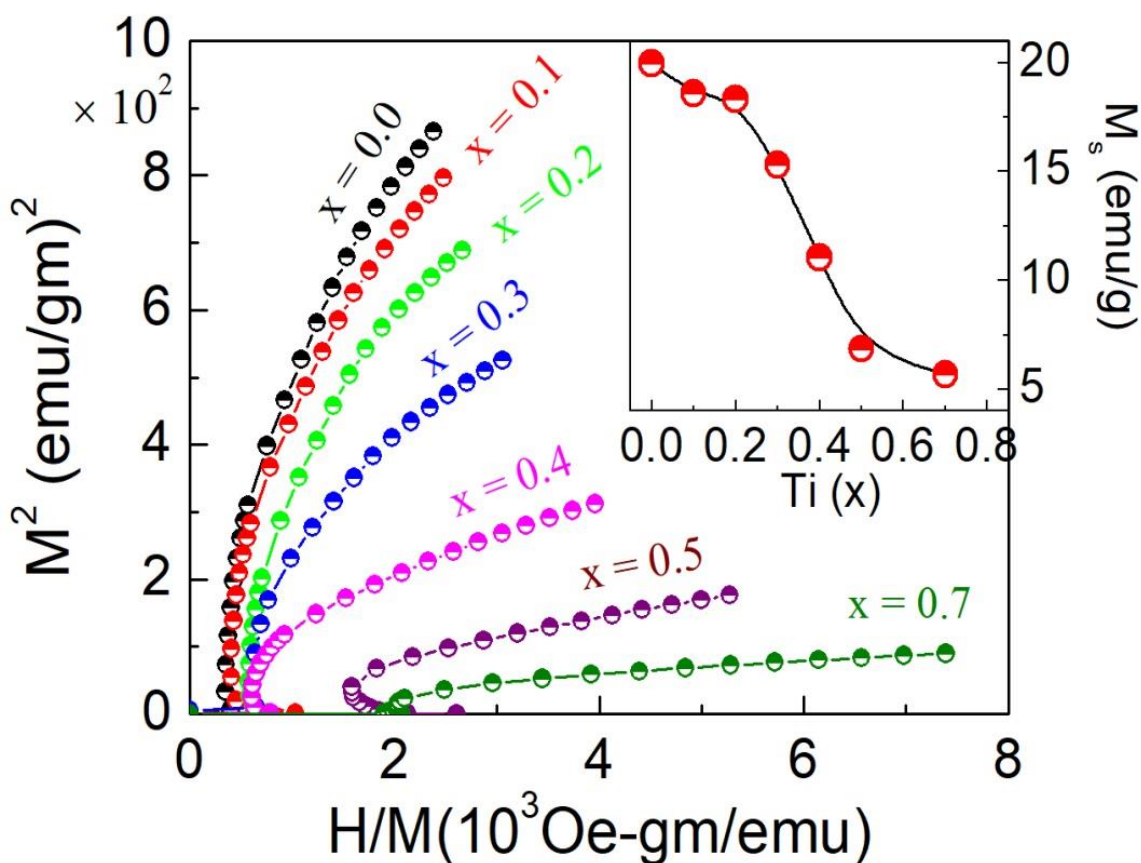


Figure 3.10 The $M(H)$ data plotted in the form of M^2 vs H/M (Arrott plot) for SrRu_{1-x}Ti_xO₃ series. Inset shows spontaneous moment M_s as obtained from Arrott plot with Ti concentration.

Now we check the Rhodes-Wohlfarth criterion [36] which is usually used to distinguish between the localized and itinerant model of magnetization based on a number of magnetic carriers per atom q_c and q_s . The q_c is estimated from effective PM moment μ_{eff}

following $\mu_{eff} = g \sqrt{S(S + 1)}$, where S is the effective spin per atom giving $S = q_c/2$. The q_s is obtained from low temperature saturation moment which is basically equals to μ_H . In case of localized moment, q_s or μ_H is realized from fully aligned moment, hence $q_c/q_s \sim 1$. For itinerant magnetism, μ_H is always lower than the fully aligned moment which results in $q_c/q_s > 1$. We calculate q_c [from Figure 3.7(a)] and q_s (from Figure 3.9) to be 1.82 and 1.25, respectively giving q_c/q_s ratio 1.46. This ratio being higher than 1 obviously implies itinerant nature of magnetism in SrRuO₃, though based on all other studies it is inferred that magnetic state in SrRuO₃ is best explained by both itinerant and localized model of magnetism.

3.3.9 Electronic transport study

SrRuO₃ is known to show metallic behavior and the Ti substitution is reported to lead the increase in resistivity $\rho(T)$ value showing metal to insulator transition around (30 – 40 %) of substitution. [7, 14, 18] With an interest to understand the evolution of electronic transport in SrRu_{1-x}Ti_xO₃ series we have measured the resistivity as a function of temperature for whole series. The $\rho(T)$ data have been shown in Figure 3.11 for whole series. The parent SrRuO₃ shows metallic behavior where the value and the behavior of $\rho(T)$, particularly that $\rho(T)$ exhibits sudden change in slope across T_c , agree with the reported study. With Ti substitution, resistivity increases in all temperatures and the series show a transition from metallic to insulating behavior around $x = 0.4$. This evolution of $\rho(T)$ with Ti substitution agrees very much with the reported studies. This further establishes that good quality of samples has been used in the present study (detail study in chapter 6).

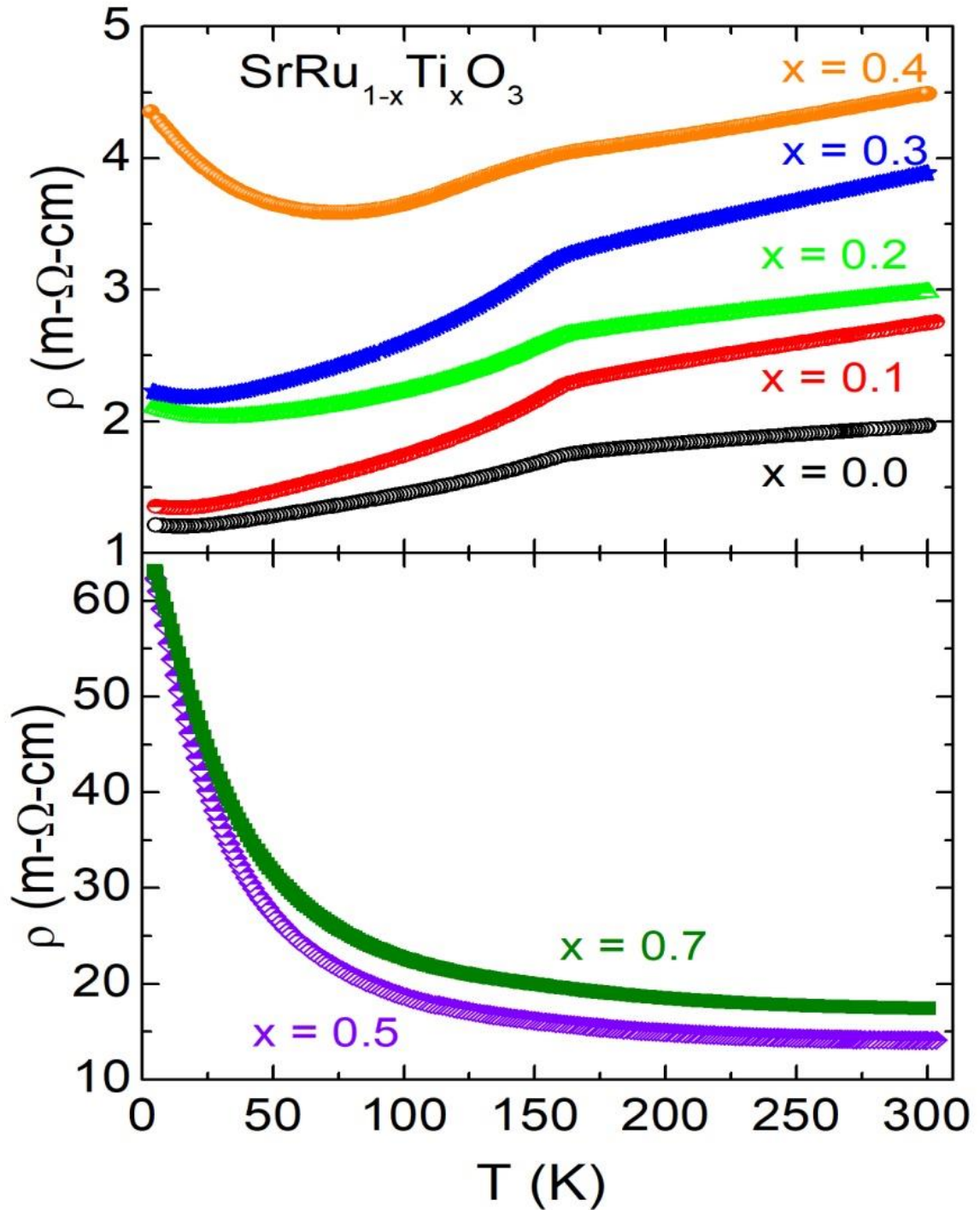


Figure 3.11 Resistivity as a function of temperature have been shown with (a) $x = 0.0, 0.1, 0.2, 0.3, 0.4$ and (b) 0.5 and 0.7 for $\text{SrRu}_{1-x}\text{Ti}_x\text{O}_3$ series.

3.3.10 Behavior of transition temperature T_c with site dilution

So far we have seen that SrRuO₃ has both itinerant and local type of magnetism. With Ti substitution, magnetic moment and Curie temperature θ_p decreases but surprisingly T_c is found remain unchanged. Following local moment model the magnetic moment, θ_p and T_c are subjected to site dilution as it will weaken the FM state [31]. In the itinerant magnetism model, T_c shows following functional dependence,

$$T_c \propto \left[1 - \frac{1}{UN(\epsilon_F)}\right]^{1/2} \quad (3.8)$$

In the present series of SrRu_{1-x}Ti_xO₃ materials, the replacement of Ru⁺⁴ ($4d^4$) by Ti⁺⁴ ($3d^0$) is expected to strengthen U and weaken $N(\epsilon_F)$ owing to its $3d^0$ character. Indeed, depletion of $N(\epsilon_F)$ and an increase of U has been theoretically calculated and experimentally verified by using photoemission spectroscopy and x-ray absorption spectroscopy with an increase in Ti substitution [10, 17]. We speculate that these opposite changes of U and $N(\epsilon_F)$ will keep the $UN(\epsilon_F)$ term in Eq. (3.8) nearly constant which has resulted in T_c without modification. While some of the experimental results such as Curie-Weiss behavior, Griffiths phase behavior, spin-wave excitation can be explained with local model magnetism, on the other hand, the low moment, single-particle excitation and unmodified T_c can be understood from itinerant aspect magnetism in SrRuO₃. The findings in our present work are in conformity with recent theoretical calculations [13]. We hope that our results will inspire further theoretical and experimental investigations using different kind of doping elements to understand this intriguing physics of itinerant ferromagnetism.

3.4 Conclusion

In summary, polycrystalline samples of SrRu_{1-x}Ti_xO₃ series with x up to 0.7 have been prepared to understand the effect of site dilution on structural and magnetic properties. The parent material SrRuO₃ crystallizes in orthorhombic- $Pbnm$ structure having GdFeO₃ type crystallographic distortion where RuO₆ octahedra exhibit both tilt and rotation. With progressive Ti substitution, structural symmetry is retained though

evolution of structural parameters has been observed. Magnetic moment and Curie temperature (θ_p) are observed to decrease with this dilution work. However, long-range magnetic ordering temperature T_c remains unchanged which is understood from the opposite tuning of electron correlation effect and DOS with Ti substitution within model of itinerant magnetism. The estimated critical exponent β (0.48) shows nature of magnetism in SrRuO₃ is of mean-field type, and an increase of β with x has been ascribed to development of FM clusters with Ti substitution. Interestingly, similar to isovalent doped Sr_{1-x}Ca_xRuO₃, these materials exhibit Griffiths phase like behavior in higher doped samples which is again believed to arise from clustering effect above T_c and represents the local moment picture of magnetism in SrRuO₃. Analysis of low temperature thermal demagnetization data is in favor of dual presence of itinerant and local moment in SrRuO₃ in conformity with recent theoretical calculation.

Bibliography

- [1]. T. Moriya, Spin Fluctuations in Itinerant Electron Magnetism, *Springer, Berlin* (1985).
- [2]. E. P. Wohlfarth, *J. Appl. Phys.*, **39**, 1061 (1968).
- [3]. F. R. de Boer, C. J. Schinkel, J. Biesterbos and S. Proost, *J. Appl. Phys.*, **40**, 1049 (1969).
- [4]. M. Uhl and J. K. Ubler, *Phys. Rev. Lett.*, **77**, 334 (1996).
- [5]. G. Koster, L. Klein, W. Siemons, G. Rijnders, J. S. Dodge, C. B. Eom, D. H. A. Blank and M. R. Beasley, *Rev. Mod. Phys.*, **84**, 253 (2012).
- [6]. G. Cao, S. McCall, M. Shepard, J. E. Crow and R. P. Guertin, *Phys. Rev. B*, **56**, 321 (1997).
- [7]. P. B. Allen, H. Berger, O. Chauvet, L. Forro, T. Jarlborg, A. Junod, B. Revaz, G. Santi, *Phys. Rev. B*, **53**, 4393 (1996).
- [8]. K. Maiti and R. S. Singh, *Phys. Rev. B*, **71**, 161102 (2005).
- [9]. M. Takizawa, D. Toyota, H. Wadati, A. Chikamatsu, H. Kumigashira, A. Fujimori, M. Oshima, Z. Fang, M. Lippmaa, M. Kawasaki and H. Koinuma, *Phys. Rev. B*, **72**, 060404 (2005).
- [10]. J. Kim, J. Y. Kim, B. G. Park and S. J. Oh Kim, *Physical Review B* **73**.23 (2006): 235109.
- [11]. D. E. Shai, C. Adamo, D. W. Shen, C. M. Brooks, J. W. Harter, E. J. Monkman, B. Burganov, D. G. Schlom and K. M. Shen, *Phys. Rev. Lett.*, **110**, 087004 (2013).

- [12]. D. W. Jeong, H. C. Choi, C. H. Kim, S. H. Chang, C. H. Sohn, H. J. Park, T. D. Kang, D. Y. Cho, S. H. Baek, C. B. Eom, J. H. Shim, J. Yu, K. W. Kim, S. J. Moon and T. W. Noh, *Phys. Rev. Lett.*, **110**, 247202 (2013).
- [13]. M. Kim and B. I. Min, *Physical Review B*, **91**, 205116 (2015).
- [14]. K. W. Kim, J. S. Lee, T. W. Noh, S. R. Lee and K. Char, *Phys. Rev. B*, **71**, 125104 (2005).
- [15]. K. Maiti, *Phys. Rev. B*, **77**, 212407 (2008).
- [16]. R. F. Bianchi, J. A. G. Carrio, S. L. Cuffini, Y. P. Mascarenhas and R. M. Faria, *Phys. Rev. B.*, **62**, 10 785 (2000).
- [17]. Pao-An Lin, Horng-Tay Jeng and Chen-Shiung Hsue, *Phys. Rev. B*, **77**, 085118 (2008).
- [18]. M. Abbate, J. A. Guevara, S. L. Cuffini, Y. P. Mascarenhas and E. Morikawa, *Eur. Phys. J. B*, **25**, 203 (2002).
- [19]. Y. J. Chang, C. H. Kim, S. H. Phark, Y. S. Kim, J. Yu and T. W. Noh, *Phys. Rev. Lett.*, **103**, 057201 (2009).
- [20]. R. B. Griffiths, *Phys. Rev. Lett.*, **23**, 17 (1969).
- [21]. C. Q. Jin, J. S. Zhou, J. B. Goodenough, Q. Q. Liu, J. G. Zhao, L. X. Yang, Y. Yu, R. C. Yu, T. Katsura, A. Shatskiy and E. Ito, *Proc. Natl. Acad. Sci., USA*, **105**, 7115 (2008).
- [22]. R. A. Young, A. Sakthivel, T. S. Moss and C. O. Paiva-Santos, Users Guide to Program DBWS-941, *Georgia Institute of Technology, Atlant* (1994).
- [23]. S. L. Cuffini, V. A. Macagno and R. E. Carbonio, *J. Solid State Chem.*, **105**, 161-170 (1993).
- [24]. H. Jang, J. Brendt, L. N. Patro, M. Martin and H. Ill Yoo, *Phys. Rev. B.*, **89**, 144107 (2014).
- [25]. C. Magen, P. A. Algarabel, L. Morellon, J. P. Araújo, C. Ritter, M. R. Ibarra, A. M. Pereira and J. B. Sousa, *Phys. Rev. Lett.*, **96**, 167201 (2006).
- [26]. A. K. Pramanik and A. Banerjee, *Phys. Rev. B*, **81**, 024431 (2010).
- [27]. A. H. Castro Neto, G. Castilla and B. A. Jones, *Phys. Rev. Lett.*, **81**, 3531 (1998).

- [28]. H. E. Stanley, *Introduction to Phase Transitions and Critical Phenomena*, Oxford University Press (1971).
- [29]. D. Fuchs, M. Wissinger, J. Schmalian, C. L. Huang, R. Fromknecht, R. Schneider and H. v. Lohneysen, *Phys. Rev. B.*, **89**, 174405 (2014).
- [30]. J. S. Zhou, K. Matsubayashi, Y. Uwatoko, C. Q. Jin, J. G. Cheng, J. B. Goodenough, Q. Q. Liu, T. Katsura, A. Shatskiy and E. Ito, *Phys. Rev. Lett.*, **101**, 077206 (2008).
- [31]. C. Kittel, *Introduction to Solid State Physics*, Wiley, New Delhi (2012).
- [32]. B. Nadgorny, M. S. Osofsky, D. J. Singh, G. T. Woods, R. J. Soulen Jr., M. K. Lee, S. D. Bu and C. B. Eom, *Appl. Phys. Lett.*, **82**, 427 (2003).
- [33]. P. Raychaudhuri, A. P. Mackenzie, J. W. Reiner and M. R. Beasley, *Phys. Rev. B*, **67**, 020411 (2003).
- [34]. C. Sow, D. Samal, P. S. Anil Kumar, A. K. Bera, and S. M. Yusuf, *Phys. Rev. B*, **85**, 224426 (2012).
- [35]. A. Arrott, *Phys. Rev.*, **108**, 1394 (1957).
- [36]. P. Rhodes and E. P. Wohlfarth, *Proc. R. Soc. London*, **273**, 247 (1963).

Chapter 4

Critical behavior in itinerant ferromagnet $\text{SrRu}_{1-x}\text{Ti}_x\text{O}_3$

In this chapter, we discuss the evolution of magnetic state in doped $\text{SrRu}_{1-x}\text{Ti}_x\text{O}_3$ through studying the critical behavior using standard techniques such as modified Arrott plot, Kouvel-Fisher plot and critical isotherm analysis across the magnetic transition temperature T_c . The substitution of nonmagnetic Ti^{4+} ($3d^0$) for Ru^{4+} ($4d^4$) simply dilute the magnetic system apart from modifying the electron correlation effect and the density of states at Fermi level. Surprisingly, T_c does not change with x . Moreover, our analysis shows the exponent β related to spontaneous magnetization increases while the exponents γ and δ related to initial inverse susceptibility and critical magnetization, respectively decrease with Ti substitution. The estimated exponents do not match with any established theoretical models for universality classes, however, the exponent obeys the Widom relation and the scaling behavior. Interestingly, this particular evolution of exponents in the present series has similarity with that in isoelectronic doped $\text{Sr}_{1-x}\text{Ca}_x\text{RuO}_3$. We believe that site dilution by Ti leads to formation magnetic clusters which cause these specific changes in critical exponents.

4.1 Introduction

The $4d$ based perovskite SrRuO_3 continues to attract large deal of scientific attention which includes both fundamental as well as technological interest. This material is commonly believed to be an itinerant type ferromagnet with transition temperature around 160 K, while offering a rare example of $4d$ based oxide having ferromagnetic (FM) ordering [1–7]. The itinerant nature of the magnetic state is manifested in the fact that measured moment shows a lower value, $\sim 1.4 \mu_B/\text{f.u.}$ in the magnetic field as high as

30 Tesla compared to expected spin-only value, $2 \mu_B/\text{f.u.}$ for $S = 1$ [2]. Interestingly, a recent theoretical study [5] has predicted the coexistence of both itinerant and localized nature of magnetism in SrRuO_3 which has also been experimentally discussed in chapter 3 [6]. Furthermore, the debate continues about the nature of magnetism in SrRuO_3 . While the majority of studies report mean-field like magnetic state in SrRuO_3 [3, 7, 8], there are several studies which imply 3D Heisenberg- or Ising-type spin interaction in this material [9-11, 13]. Interestingly, one recent study shows that linearity in Arrott plot (signature for mean-field model) in SrRuO_3 is mainly realized due to continuous curvature evolution from $\text{Ca}_{0.5}\text{Sr}_{0.5}\text{RuO}_3$ to BaRuO_3 via SrRuO_3 as lattice distortions and spin-orbit coupling changes, and it is less likely due to itinerant type ferromagnetism in SrRuO_3 [7]. Similarly, the influence of anisotropy on critical behavior where the exponent values change with crystal axis has also been shown for SrRuO_3 [11, 12]. This underlines the fact that even after large volume of study, the detail nature of magnetic state in SrRuO_3 is still debated.

There have been several attempts to understand the nature of magnetism using route of chemical substitution. The most prominent one is the isoelectronic substitution at Sr-site. The Ca^{2+} substitution in $\text{Sr}_{1-x}\text{Ca}_x\text{RuO}_3$ shows a total suppression of FM ordering at about 70% of doping concentration, a phenomenon which has been associated with the FM quantum phase transition (QPT) phenomenon [2, 3]. Band structure calculations show that substitution of Ca causes further distortion in RuO_6 octahedra and in Ru-O-Ru bond angle which effectively decreases the density of states at Fermi level $N(\epsilon_F)$. Hence the necessary Stoner criterion for itinerant ferromagnet is no more satisfied [4]. The critical behavior in $\text{Sr}_{1-x}\text{Ca}_x\text{RuO}_3$ shows an interesting evolution where the exponent β increases, and both γ and δ decreases with Ca doping which has been attributed to the effect of disorder arising from quantum fluctuation close to QPT point and phase segregation effect [3, 7]. On the other hand, Ba^{2+} substitution in $\text{Sr}_{1-x}\text{Ba}_x\text{RuO}_3$ lowers the T_c down to about 60 K and the nature of magnetism is found to follow the 3D Heisenberg model [14] closely.

In present work, we have investigated the magnetic state in SrRu_{1-x}Ti_xO₃ by studying evolution of critical behavior as the related critical exponents and critical temperature represent an intrinsic nature of the magnetic behavior of a material. From structure wise, ionic radii of Ru⁴⁺ (0.62 Å) and Ti⁴⁺ (0.605 Å) closely match which implies this substitution will introduce minimum structural modification, hence the structural disorder induced modification in the magnetic state is least expected. Rather, nonmagnetic Ti⁴⁺ would simply dilute the magnetic structure formed by transition metal and oxygen network. Further, substitution of Ti⁴⁺ ($3d^0$) for Ru⁴⁺ ($4d^4$) would oppositely tune the electron correlation U and $N(\epsilon_F)$ which will have wide ramification on Stoner criteria of itinerant FM i.e., $UN(\epsilon_F) > 1$ [15]. Even, a large change of T_c has been observed with variation of $N(\epsilon_F)$ in the ultra-thin film of SrRuO₃ [16]. In fact, recently we have shown while effective magnetic moment and the Curie-Weiss temperature decreases in SrRu_{1-x}Ti_xO₃ with x , the FM transition temperature T_c appears to remain unchanged [6]. This unchanged behavior of T_c has been understood through an opposite tuning of U and $N(\epsilon_F)$ in the picture of itinerant ferromagnet where the combined term $UN(\epsilon_F)$ effectively remains constant with Ti doping. Indeed, photoemission spectroscopy measurements as well as band structure calculations have shown a gradual increase of U and depletion of $N(\epsilon_F)$ with Ti substitution in SrRuO₃ [17, 18]. With Ti substitution, SrRuO₃ further develops Griffiths-phase like behavior which arises due to disorder coming from formation of magnetic clusters above T_c which has similarly been evidenced in Sr_{1-x}Ca_xRuO₃ [14]. This present series of samples share some of the properties with isoelectronic doped Sr_{1-x}Ca_xRuO₃, therefore it would be interesting to understand the critical behavior in SrRu_{1-x}Ti_xO₃.

Here, we have studied the critical behavior in SrRu_{1-x}Ti_xO₃ series with $x = 0.0, 0.1, 0.3, 0.4, 0.5$ and 0.7 . We have estimated the critical exponents (β , γ , and δ) and T_c following various independent methods such as modified Arrott plot, Kouvel-Fisher method and critical isotherm analysis. The estimated exponent β for SrRuO₃ is close to the value for the mean-field model (Table 4.1). The exponents for doped materials do not match with the values theoretically predicted for different universality classes based on 3-

dimensional magnetism. The estimated exponents, however, obey the scaling law behavior and Widom relation which implies values are correct.

Table 4.1 Table shows the values of critical exponents β , γ and δ determined using different independent methods such as modifier Arrott plot (MAP), Kouvel-Fisher (KF) plot and critical isotherm analysis for SrRu_{1-x}Ti_xO₃ series. The values of exponents calculated theoretically following different spin interaction models are also given for comparison.

Composition	Ref.	Method	β	$T_c(M_s)$	γ	$T_c(\chi_0)$	δ
SrRuO ₃	This work	MAP	0.534(5)	164.02(1)	0.752(9)	164.09(3)	2.408(2)
		KF Method	0.542(8)	164.02(3)	0.753(6)	164.08(3)	2.389(2)
		Critical Isotherm					2.389(3)
SrRu _{0.9} Ti _{0.1} O ₃	This work	MAP	0.592(6)	163.28(6)	0.574(2)	163.22(0)	1.969(5)
		KF Method	0.592(4)	163.24(5)	0.574(3)	163.26(4)	1.969(5)
		Critical Isotherm					1.974(5)
SrRu _{0.7} Ti _{0.3} O ₃	This work	MAP	0.752(2)	163.03(2)	0.543(9)	163.02(3)	1.722(0)
		KF Method	0.747(9)	163.01(4)	0.540(7)	163.07(3)	1.722(8)
		Critical Isotherm					1.729(4)
SrRu _{0.6} Ti _{0.4} O ₃	This work	MAP	0.831(6)	163.09(2)	0.418(2)	163.05(1)	1.503(0)
		KF Method	0.825(6)	163.06(4)	0.419(8)	163.01(8)	1.507(8)
		Critical Isotherm					1.492(2)
SrRu _{0.5} Ti _{0.5} O ₃	This	MAP	1.120(5)	163.03(1)	0.360(2)	163.00(1)	1.321(4)

3	work	KF Method	1.121(0)	163.04(4)	0.357(6)	163.08(2)	1.318(4)
		Critical Isotherm					1.325(5)
SrRu_{0.3}Ti_{0.7}O 3	This work	MAP	0.994(5)	163.11(5)	0.446(3)	163.10(1)	1.448(6)
		KF Method	0.978(7)	163.02(3)	0.447(4)	163.11(3)	1.457(0)
		Critical Isotherm					1.454(1)
Mean-field Model	[26]	Theory	0.5		1.0		3.0
3D Heisenberg Model	[26]	Theory	0.365		1.386		4.8
3D Ising Model	[26]	Theory	0.325		1.241		4.82

4.2 Experimental Details

Polycrystalline samples of series $\text{SrRu}_{1-x}\text{Ti}_x\text{O}_3$ with $x = 0.0, 0.1, 0.3, 0.4, 0.5$ and 0.7 are prepared by standard solid state method. The samples have been characterized by x-ray diffraction (XRD) and by Rietveld analysis of XRD data. All the samples are in a single phase and without any noticeable chemical impurity. Details of sample preparation and characterization are given elsewhere [6]. Temperature (T) dependent magnetization (M) data have been collected with superconducting quantum interference device (SQUID) magnetometer by *M/s* Quantum Design. For critical analysis, magnetic field (H) dependent isotherms $M(H)$ have been collected at an interval of 1 K across T_c using vibrating sample magnetometer (VSM) by *M/s* Cryogenics Ltd. For proper stabilization of temperature, about 10 minute wait time has been given before recording each isotherm. The external applied magnetic field (H_a) has been corrected by the

demagnetization effect to get the internal magnetic field $H_i [=H_a - N M(T, H_a)]$, where $M(T, H_a)$ is the measured magnetization and N is the demagnetization constant that has been calculated from the physical dimensions of sample [19]. This calculated H_i has been used for critical exponent scaling analysis. The critical temperature and critical exponents are have been determined by commonly used techniques like modified Arrott plots (MAP), Kouvel-Fisher (KF) method and critical isotherm analysis.

4.3 Results and Discussions

4.3.1 Scaling Analysis

In case of second-order phase transition, the correlation length (ξ) among spins diverges at the magnetic phase transition temperature T_c following $\xi = \xi_0|1 - (T/T_c)|^{-\nu}$ where ν is the exponent. Following this, scaling hypothesis predicts that spontaneous magnetization M_s below T_c , initial inverse susceptibility χ_0^{-1} above T_c and magnetization at T_c obey set of power law behavior with temperature as described below [20],

$$M_s(T) = M_0(-t)^\beta, \quad t < 0 \quad (4.1)$$

$$\chi_0^{-1}(T) = G(t)^\gamma, \quad t > 0 \quad (4.2)$$

$$M = X H^{1/\delta}, \quad t = 0 \quad (4.3)$$

where $t = (T - T_c)/T_c$ is the reduced temperature; M_0 , G and X are the critical amplitudes and β , γ and δ are the critical exponents. The scaling hypothesis further predicts magnetic equation of state which describes the relationship between $M(H, t)$, H and T in following manner,

$$M(H, t) = t^\beta f_\pm\left(\frac{H}{t^{\beta+\gamma}}\right) \quad (4.4)$$

where f_+ and f_- are the regular functions for $T > T_c$ and $T < T_c$, respectively. The Eq. (4.4) implies that for right values of critical temperature T_c and critical exponents β and γ , the scaled magnetization $m = t^{-\beta}M(H, t)$ plotted as a function of scaled field $h = t^{-(\beta+\gamma)}H$ would fall on two distinct curves for isotherms both above and below T_c .

4.3.2 DC Magnetization study

Figure 4.1 shows dc magnetization data collected following field cooled (FC) protocol in the magnetic field of 100 Oe for SrRu_{1-x}Ti_xO₃ series. Recently, we have shown an interesting evolution of the magnetic behavior of SrRu_{1-x}Ti_xO₃ series [6]. For parent SrRuO₃, we have observed the magnetic transition temperature $T_c \sim 163$ K which is in conformity with other studies [1–3, 13]. With site dilution through Ti substitution, while though the Curie-Weiss temperature (θ_p) and the magnetic moments decreases, interestingly the long-range magnetic ordering temperature T_c does not change.

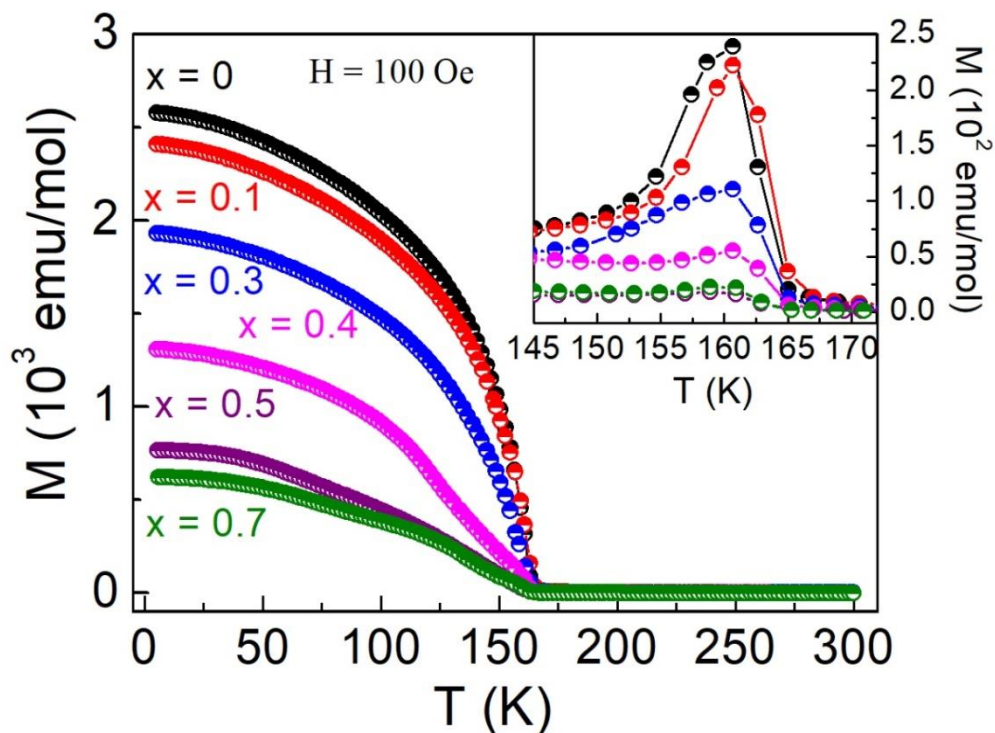


Figure 4.1 Temperature dependent field cooled magnetization data measured in the presence of 100 Oe applied field have been shown for SrRu_{1-x}Ti_xO₃ series. The inset shows zero field cooled magnetization (100 Oe) in an expanded temperature range close to T_c .

In the scenario of itinerant ferromagnetism, we explained this constant nature of T_c through opposite tuning of the density of states (DOS) and electronic correlation (U) with Ti substitution. As evident in the main panel of Figure 4.1, FC magnetization for all the samples shows a sudden rise around 163 K which marks the T_c . The inset of Figure 4.1 depicts ZFC magnetization data in a close temperature scale around T_c . As evident in the inset figure, M_{ZFC} show peak around 163 K which does not change with x . Here, it can be mentioned that our critical analysis of $M_{FC}(T)$ data also shows a constant T_c in present SrRu_{1-x}Ti_xO₃ series. This analysis further shows critical exponent β related to magnetization for parent SrRuO₃ closely matches with that for the mean field model, and the value of β increases with x . In following, we have undertaken detailed critical analysis to understand the effect of site dilution on critical behavior in SrRu_{1-x}Ti_xO₃ series.

4.3.3 Arrott Plot

The Arrott plot offers an important tool to study the second-order magnetic phase transition and the critical behavior across second order PM-FM phase transition [21]. Arrott plot is about the plotting of isothermal $M(H)$ data in the form of M^2 vs. H/M where for a mean-field model with $\beta = 0.5$ and $\gamma = 1$, the isotherms form a set of parallel straight lines. In another sense, straight line behavior in high field regime in Arrott plot implies magnetic interaction is of mean-field type. Intercept due to straight line fitting in Arrott plot on M^2 and H/M axis directly gives spontaneous magnetization (M_s) and initial inverse susceptibility (χ_0^{-1}), respectively. Moreover, isotherm which passes through the origin in Arrott plot marks the T_c as implies zero M_s . As discussed, for analysis of Arrott plot, a set of isotherms $M(H)$ is required across the T_c . Figures 4.2 (a)–(f) show isotherms (M vs H plots) collected at different temperatures with temperature interval of $\Delta T = 1$ K across T_c for SrRu_{1-x}Ti_xO₃ series. The $M(H)$ plots for all the samples look like FM type where it shows downward curvature. Inset in each figure of Figure 4.2 shows a derivative of magnetization (dM/dH) as a function of field for one representative temperature. Inset figures show a decreasing slope of $M(H)$ plot with field. This constitutes a typical signature of second-order PM to FM transition and justifies for following critical analysis.

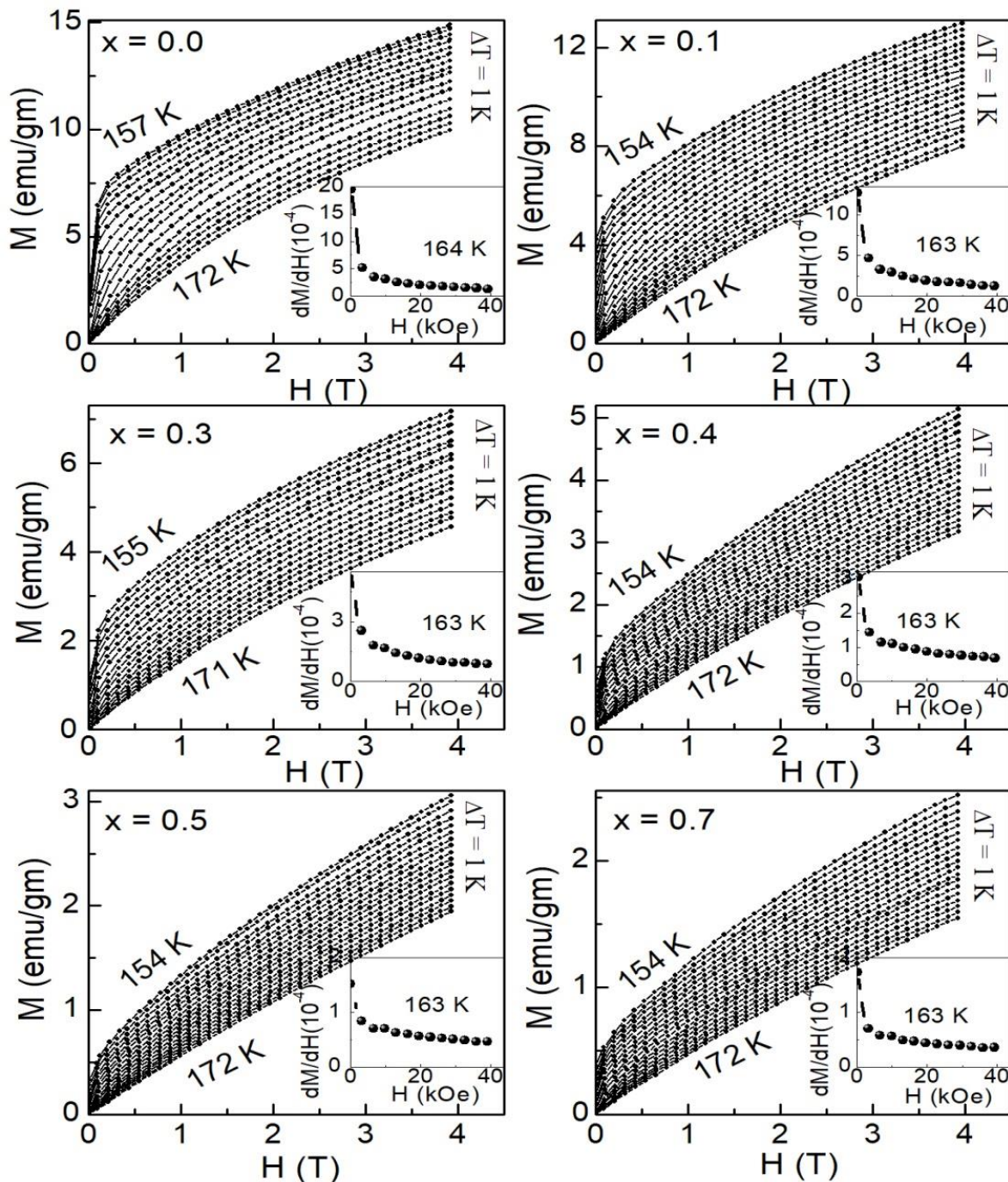


Figure 4.2 Field dependent isothermal magnetization data near to the transition temperature $\sim T_c$ are shown for $\text{SrRu}_{1-x}\text{Ti}_x\text{O}_3$ series with (a) $x = 0.0$ (b) $x = 0.1$ (c) $x = 0.3$ (d) $x = 0.4$ (e) $x = 0.5$ and (f) $x = 0.7$ composition. Inset of each figure shows magnetic-field derivative of magnetization (dM/dH) as a function of magnetic field for $M(H)$ plots taken at T_c for respective sample.

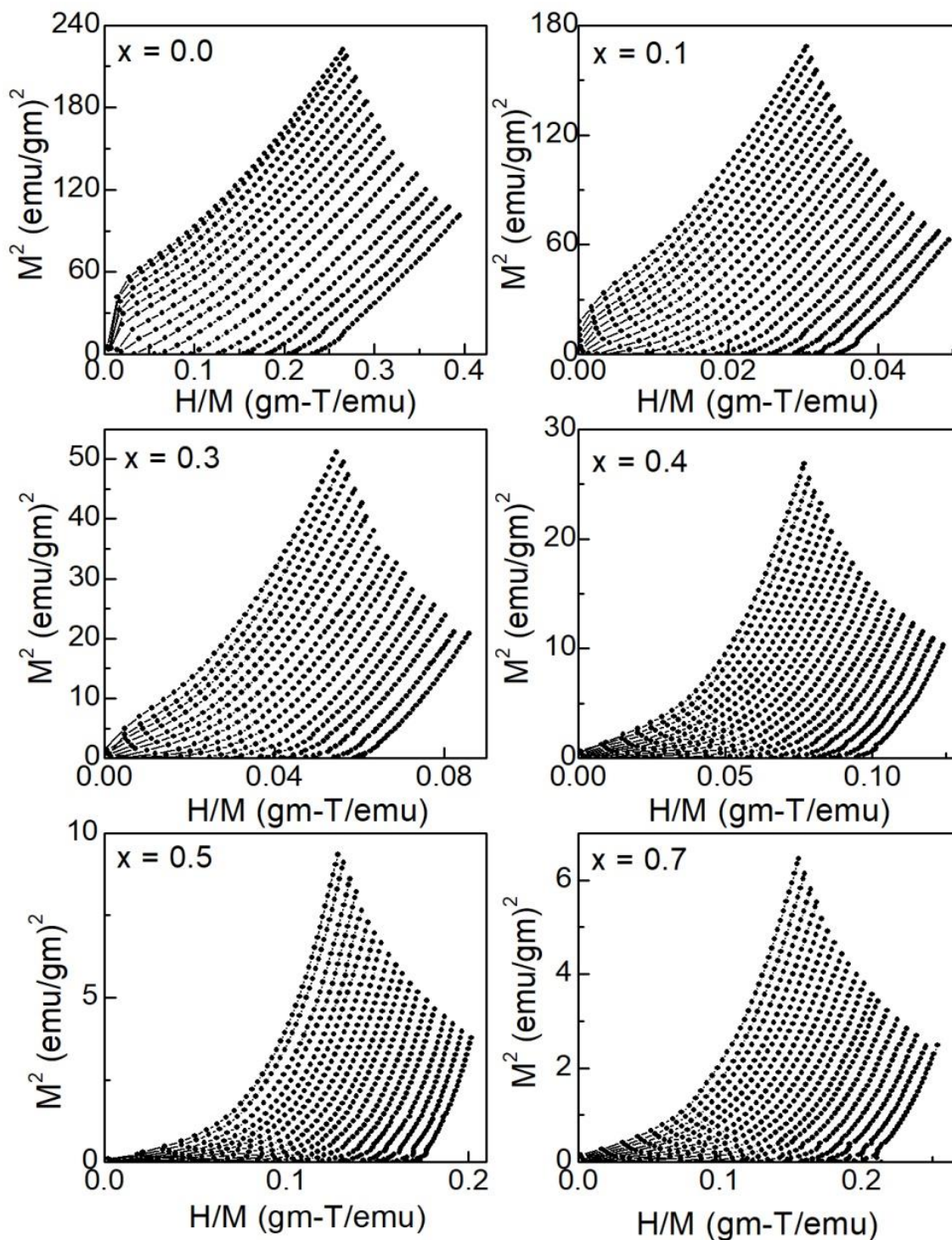


Figure 4.3 Isotherms in Figure 4.2 are plotted in form of Arrott plot (M^2 vs H/M) for $\text{SrRu}_{1-x}\text{Ti}_x\text{O}_3$ series with (a) $x = 0.0$ (b) $x = 0.1$ (c) $x = 0.3$ (d) $x = 0.4$ (e) $x = 0.5$ and (f) $x = 0.7$.

Figure 4.3(a) – (f) show Arrott plot, constructed from $M(H)$ isotherm data shown in Figure 4.2 for SrRu_{1-x}Ti_xO₃ series. For parent SrRuO₃, nature of magnetic state has mostly been shown by earlier studies to follow mean-field interaction model [3]. As discussed, for a mean-field model with critical exponents $\beta = 0.5$ and $\gamma = 1$, the Arrott plot should yield a set of parallel straight lines. Arrott plot for SrRuO₃ in Figure 4.3(a) shows isotherms do not form straight lines even in high field regime; they are rather slightly curved in upward direction. This means critical exponents for SrRuO₃ do not exactly match with the mean-field model, but they are close to the mean-field values. Figure 4.3 further shows with increasing x , nonlinearity in Arrott plot increases which suggests the nature of magnetic interaction moves away from the mean-field model as Ti is introduced in SrRuO₃. As we do not obtain parallel straight lines with mean-field exponents, the analysis in Figure 4.3 suggests a new set of exponents need to be identified for straight line behavior.

To determine the critical exponents and temperature correctly for the present series of samples, we have employed modified Arrott plot (MAP) which is a generalized form of Arrott plot and is based on Arrott-Noakes equation of state given as below [22],

$$\left(\frac{H}{M}\right)^{1/\gamma} = a \left(\frac{T-T_c}{T}\right) + bM^{1/\beta} \quad (4.5)$$

where a and b are the constant. It is obvious that for $\beta = 0.5$ and $\gamma = 1$, Eq. (4.5) recovers Arrott plot discussed above. Following MAP, isotherms are plotted in the form of $M^{1/\beta}$ vs $(H/M)^{1/\gamma}$. Here, we note that we have also tried to form MAP with the exponents β and γ which are theoretically predicted for 3-dimensional models such as, 3D Heisenberg, 3D Ising, 3D XY models, etc. (Table 4.1) but remain unsuccessful in getting parallel straight lines. As the exponents $\beta = 0.5$ and $\gamma = 1$ do not yield straight lines in Figure 4.3, we have tuned the exponents β and γ to obtain parallel straight lines. However, tuning of these parameters is not a straightforward job as two unknown parameters are involved and this often leads to erroneous results. Here, we have adopted an iterative method where we initially tuned β and γ in Eq. (4.5) to get apparently good parallel straight lines in modified Arrott plot [23, 24].

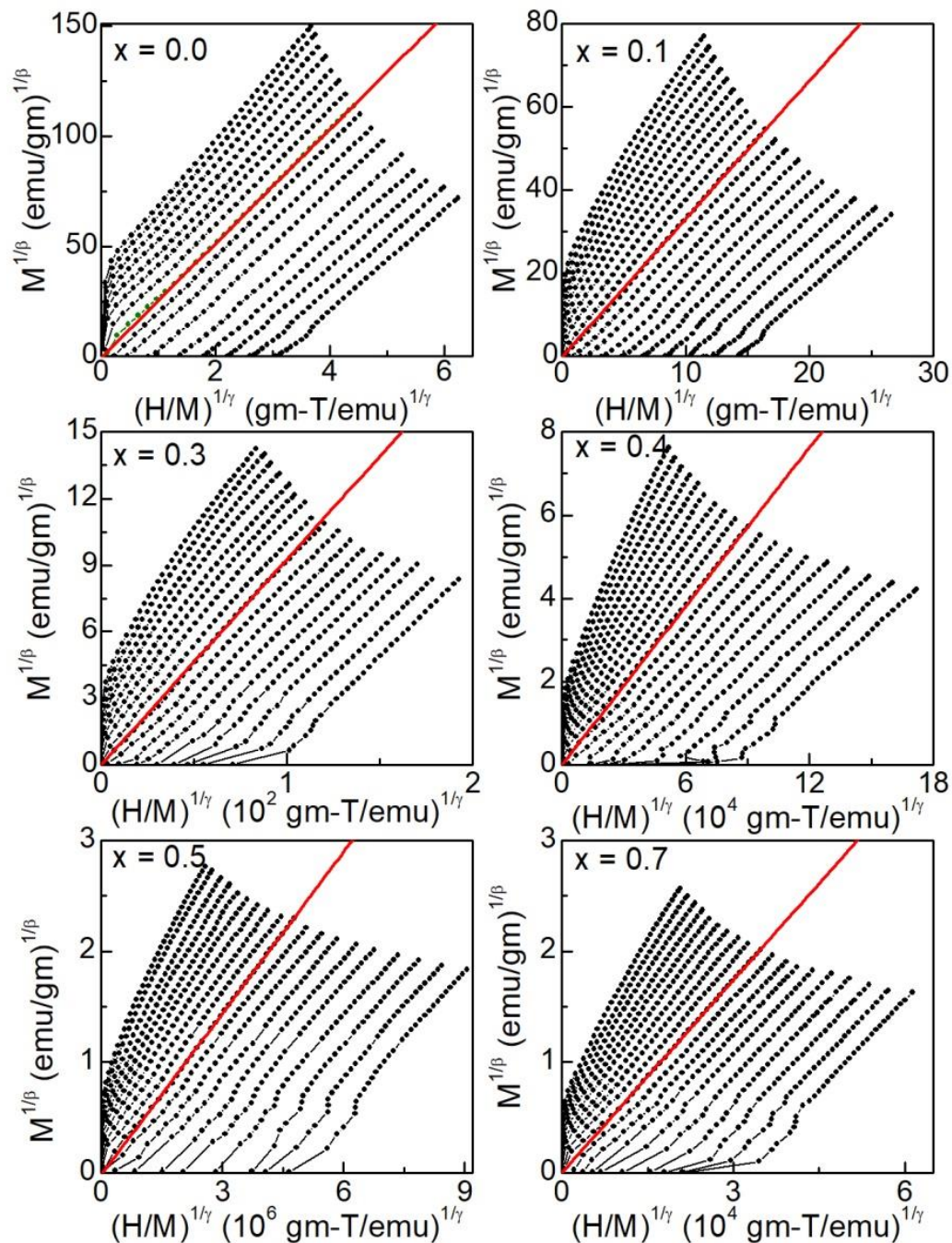


Figure 4.4 Modified Arrott plot, $M^{1/\beta}$ vs $(H/M)^{1/\gamma}$, constructed out of $M(H)$ data in Figure 4.2 are shown for $\text{SrRu}_{1-x}\text{Ti}_x\text{O}_3$ series with (a) $x = 0.0$ (b) $x = 0.1$ (c) $x = 0.3$ (d) $x = 0.4$ (e) $x = 0.5$ and (f) $x = 0.7$. The solid red line in each figure is due to straight line fitting of modified Arrott plot related to isotherm which passes through origin.

Then, temperature dependent $M_s(T)$ and $\chi_0^{-1}(T)$ have been obtained from the intercept of straight fitting in MAP on $M^{1/\beta}$ and $(H/M)^{1/\gamma}$ axis, respectively. The T_c has been identified as the temperature whose $M(H)$ isotherm passes through origin in MAP. These $M_s(T)$, $\chi_0^{-1}(T)$ and T_c are then used in Eq. (4.1) and Eq. (4.2) to obtain new set of β and γ . These new values of β and γ have been used to construct similar MAP. This process has been continued till a convergence in values of critical exponents β and γ and critical temperature T_c is obtained.

Figures 4.4 (a)–(f) show the MAP of isotherms shown in Figures 4.2 (a)–(f) in the vicinity of T_c for all the samples. For parent SrRuO₃, we find that $\beta = 0.54$ and $\gamma = 0.75$ yields parallel straight lines where isotherm at 164 K passes through origin marking the T_c of this material (Figure 4.4a). The same iterative method has been followed for all the samples. Figures 4.4 (a)–(f) show the MAP for all the samples in present series where reasonably good parallel straight lines have been formed in high field regime with proper choice of exponents β and γ .

The finally obtained M_s and χ_0^{-1} have been shown as a function of temperature in Figures 4.5 (a)–(f), showing M_s cease to exist once temperature approaches T_c . The $M_s(T)$ and $\chi_0^{-1}(T)$ data in Figures 4.5(a)–(f) have been fitted with Eq. (4.1) and (4.2), respectively, for all the compositions. The exponents β and γ and temperature T_c are obtained as fitting parameters. Table 4.1 shows the exponents β and γ and respective T_c following MAP method. From fitting of $M_s(T)$ with Eq. (4.1) we obtain $\beta = 0.534(5)$ and $T_c = 164.02(1)$ K and from fitting of $\chi_0^{-1}(T)$ with Eq. (4.2) we get $\gamma = 0.752(9)$ and $T_c = 164.09(3)$ K. These values of β , γ and T_c are significantly close to the values obtained using MAP in Figure 4.4 which underlines the correctness of our iterative method. The T_c values obtained from both $M_s(T)$ and $\chi_0^{-1}(T)$ in MAP show consistent behavior for whole series. For SrRuO₃, obtained $T_c \sim 164$ K matches well with the reported values. Remarkably, T_c remains almost constant with Ti substitution in present series which substantiates our earlier results [6]. The obtained exponents β and γ do not exactly match with the values theoretically predicted for three dimensional systems (Table 4.1), however, values look closer to mean-field model for $x = 0.0$ material.

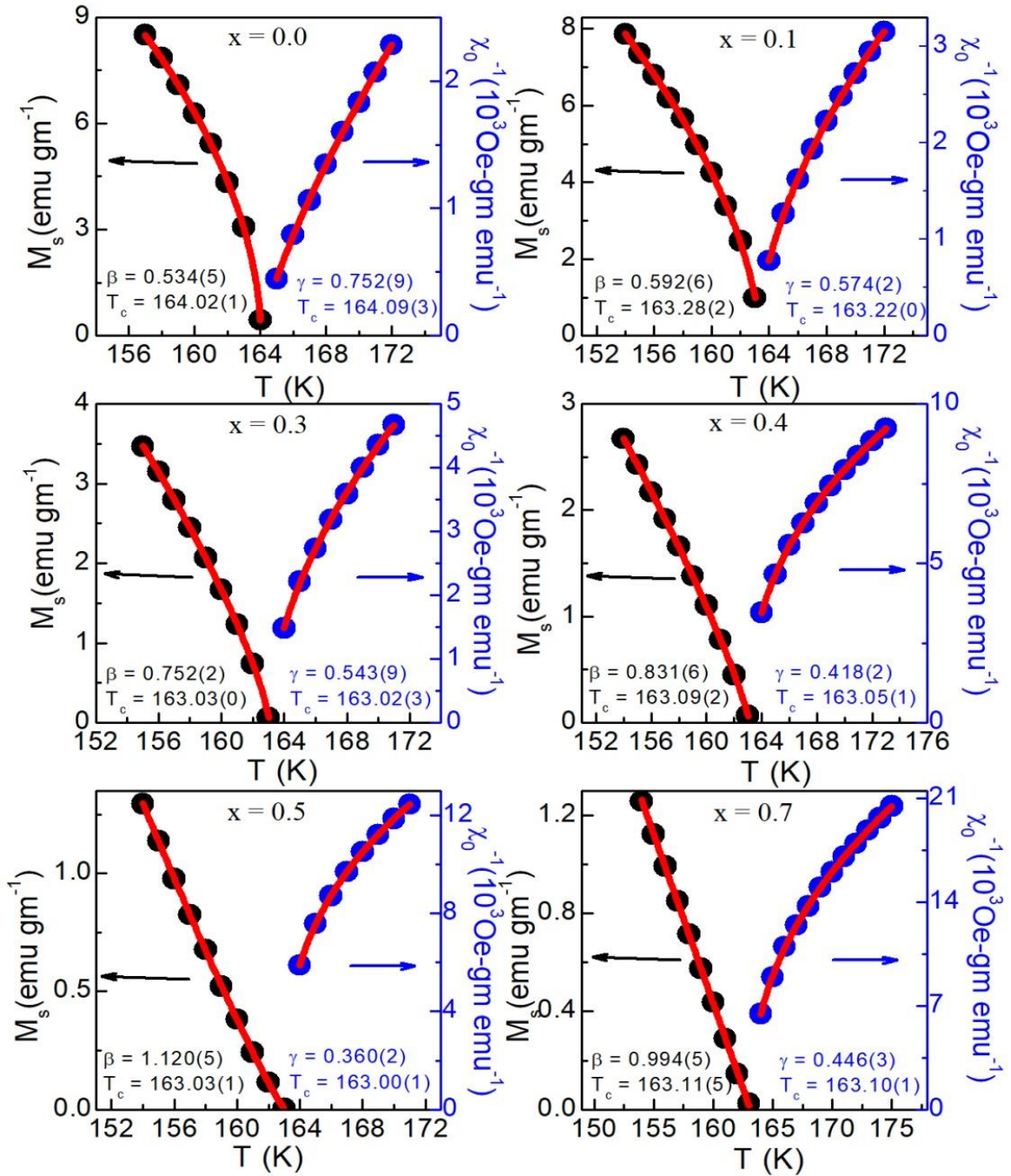


Figure 4.5 Temperature dependent spontaneous magnetization M_s (left axis) and initial inverse susceptibility $\chi_0^{-1}(T)$ (right axis) as estimated from modified Arrott plots in Figure 4.4 are shown for SrRu_{1-x}Ti_xO₃ series with (a) $x = 0.0$ (b) $x = 0.1$ (c) $x = 0.3$ (d) $x = 0.4$ (e) $x = 0.5$ and (f) $x = 0.7$. The solid red lines are due to fitting with power law behavior as stated in Eq. (4.1) and Eq. (4.2).

4.3.4 Kouvel-Fisher plot

Alternatively, critical exponents β and γ and the critical temperature T_c have been determined using more accurate Kouvel-Fisher (KF) method where the M_s and χ_0^{-1} are analyzed using Eqs. (4.6) and (4.7), respectively [25]. The KF plot for whole series of samples has been shown in Figures 4.6 (a)–(f) where $M_s(T)[dM_s(T)/dT]^{-1}$ vs T and $\chi_0^{-1}(T) [d\chi_0^{-1}(T)/dT]^{-1}$ vs T are plotted. According to KF method (Eq. 4.6 and 4.7), these plots would result in straight line behavior where the respective slope would give $1/\beta$ and $1/\gamma$. In addition, T_c can be obtained directly and independently as the intercept on temperature axis would give T_c . In deed, Figure 4.6 shows KF plot forms reasonable straight lines for all the samples which confirm the correctness of KF analysis. For SrRuO₃, we obtain exponents $\beta = 0.542(8)$ and $T_c = 164.02(3)$, and $\gamma = 0.753(6)$ and $T_c = 164.08(3)$. These values of β , γ and T_c obtained from KF plot are given in Table 4.1 for all the compositions. It is remarkable that values of exponents and T_c obtained from KF plots match closely with those obtained from MAF analysis. With Ti substitution, while β increases away from the mean-field value and, on other hand, the γ decreases. Nonetheless, agreement between values obtained from two independent MAP and KF method is quite remarkable indicating obtained values are correct.

$$M_s(T)[dM_s(T)/dT]^{-1} = \frac{T-T_c}{\beta} \quad (4.6)$$

$$\chi_0^{-1}(T)[d\chi_0^{-1}(T)/dT]^{-1} = \frac{T-T_c}{\gamma} \quad (4.7)$$

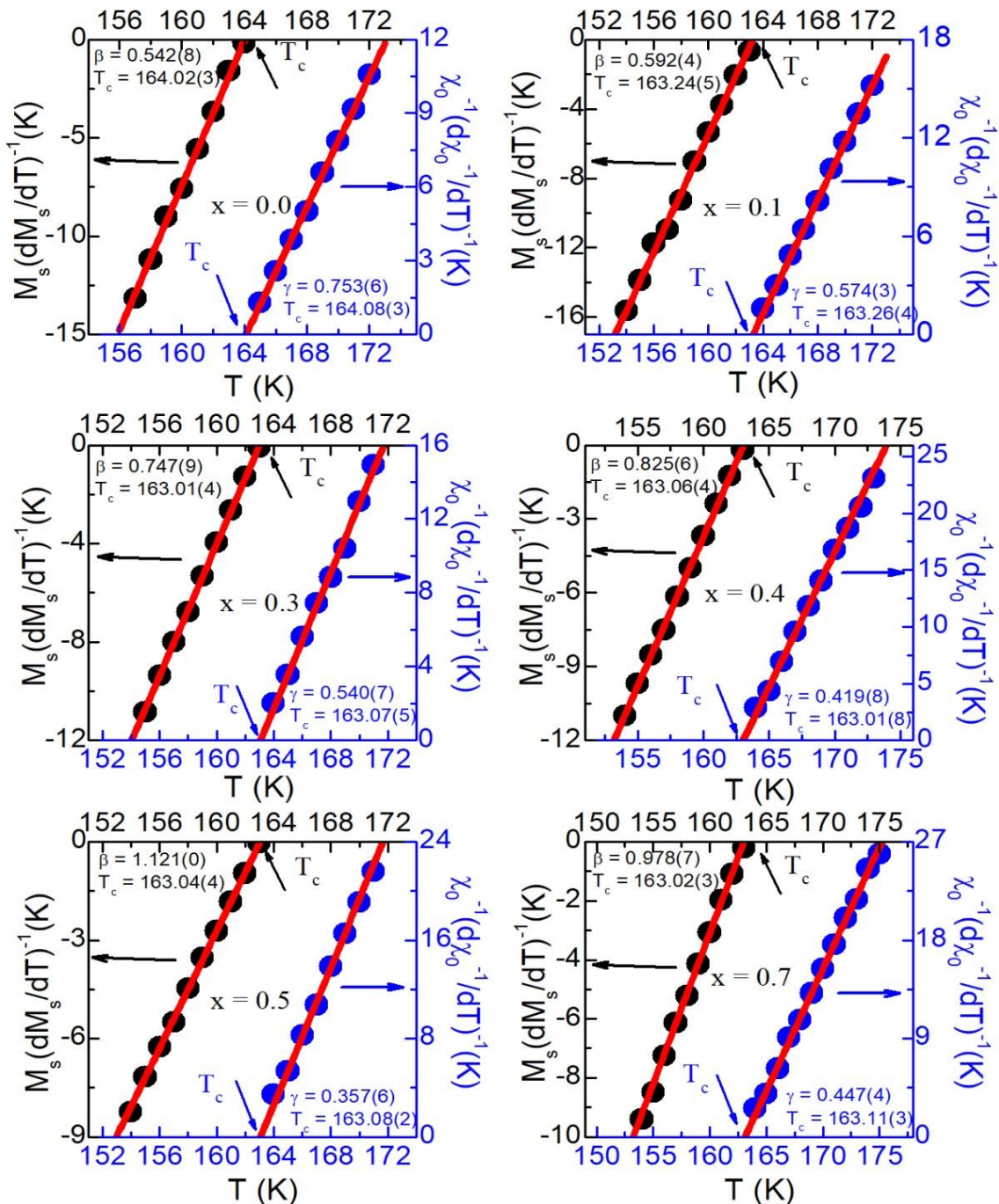


Figure 4.6 Kouvel-Fisher plots for spontaneous magnetization (Eq. 4.6) on left axis and for initial inverse susceptibility (Eq. 4.7) on right have been shown for SrRu_{1-x}Ti_xO₃ series with (a) $x = 0.0$ (b) $x = 0.1$ (c) $x = 0.3$ (d) $x = 0.4$ (e) $x = 0.5$ and (f) $x = 0.7$. The solid straight lines are the linear fits following Eq. 4.6 and 4.7.

4.3.5 Critical isotherm plot

Scaling analysis predicts that variation of $M(H)$ at T_c (critical isotherm) follows a power-law behavior involving exponent δ (Eq. 4.3). Critical isotherms are already identified from MAP in Figure 4.4. The main panel of Figures 4.7 (a)–(f) shows critical isotherms $M(H, T_c)$ for all samples in the present series. The inset of Figures 4.7 (a)–(f) show same plot in \log_{10} - \log_{10} scale. Following Eq. 4.3, slope due to straight line fitting in $\log M$ vs. $\log H$ plot would give $1/\delta$. The inset plots show reasonably linear behavior, and the exponent δ calculated from the slope is given in Table 4.1 as the critical isotherm method. Again, obtain δ does not match with the theoretical values predicted for 3D based different universality classes as mentioned in Table 4.1. To crosscheck the consistency of the estimated exponents, we have used Widom scaling relation where the critical exponents β , γ , and δ obey following relation [27],

$$\delta = 1 + \frac{\gamma}{\beta} \quad (4.8)$$

Eq. (4.8) indirectly gives exponent δ using the values of exponents γ and β . The δ has been calculated following Eq. (4.8) using β and γ values which are estimated from both MAP and KF plot methods. Table 4.1 shows exponent δ where the values represent both obtained from analysis of critical isotherm as well as calculated from using Eq. (4.8). For SrRuO₃, we obtain $\delta = 2.389(3)$ following critical isotherm analysis (Figure 4.7) and 2.408(2) and 2.389(2) from MAP and KF plot using Eq. (4.8). Both the estimated and calculated values match well. With Ti substitution, δ continuously decreases till $x = 0.5$ and then shows an increased value for $x = 0.7$. It is remarkable that values of δ obtained from two distinct processes agree reasonably for all the materials which emphasize that values of exponents β , γ , δ and temperature T_c are estimated quite accurately.

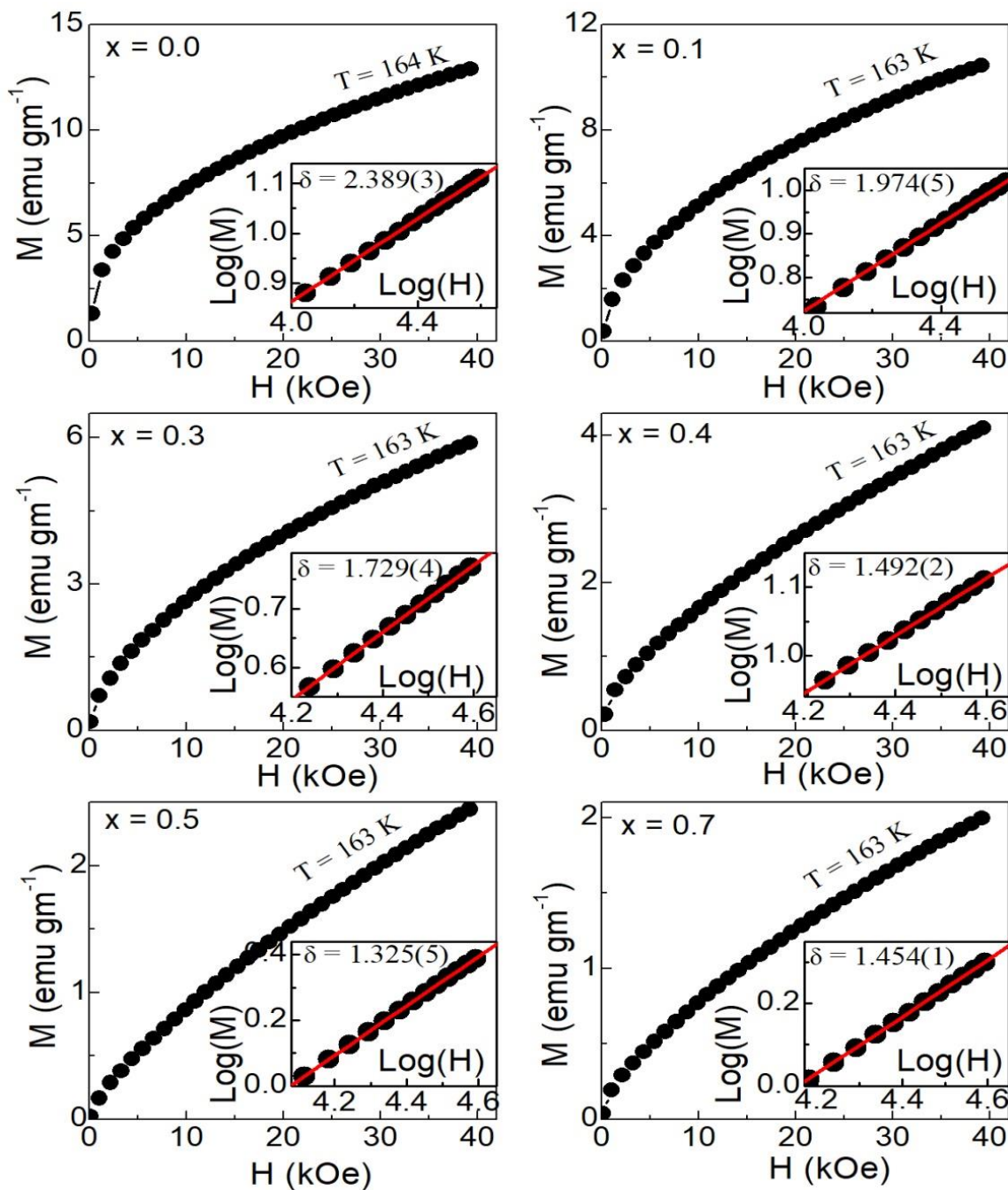


Figure 4.7 The $M(H)$ isotherm at T_c has been shown for $\text{SrRu}_{1-x}\text{Ti}_x\text{O}_3$ series with (a) $x = 0.0$ (b) $x = 0.1$ (c) $x = 0.3$ (d) $x = 0.4$ (e) $x = 0.5$ and (f) $x = 0.7$. The inset shows same $M(H)$ data in \log_{10} - \log_{10} scale for respective samples and the solid line is due to linear fit of the data.

4.3.6 Scaling analysis

So far we have seen that critical exponents in present series do not exactly match with any established theoretical models for classical spin interaction. However, the exponents and T_c determined using different independent methods such as, modified Arrott plot, Kouvel-Fisher plot and critical isotherm analysis agree very closely (Table 4.1). Moreover, exponents follow Widom relation. We have further tested the consistency and accuracy of exponents as well as T_c using a scaling analysis (Eq. 4.4). This analysis suggests plotting of magnetic isotherm $M(H)$ data in the form of $M|t|^{-\beta}$ vs $H|t|^{-(\gamma + \beta)}$ where the isotherms both below and above T_c are scaled into a separate line for correct values of critical exponents and T_c . This rather constitutes a rigorous test to examine the consistency and accuracy of exponents as well as T_c . Scaling plots are shown in Figures 4.8(a)–(f) for this present series where four scaled isotherms both below and above of respective T_c are plotted following Eq. (4.4). As seen in Figure 4.8, isotherms both below and above T_c are nicely scaled into a line. The same plot is shown in \log_{10} - \log_{10} scale in inset of Figure 4.8 for better presentation which also shows a nice scaling of isotherm data. This reconfirms that estimated exponents (β , γ and δ), as well as T_c in Table 4.1 for all the samples in this series, are accurate and consistent.

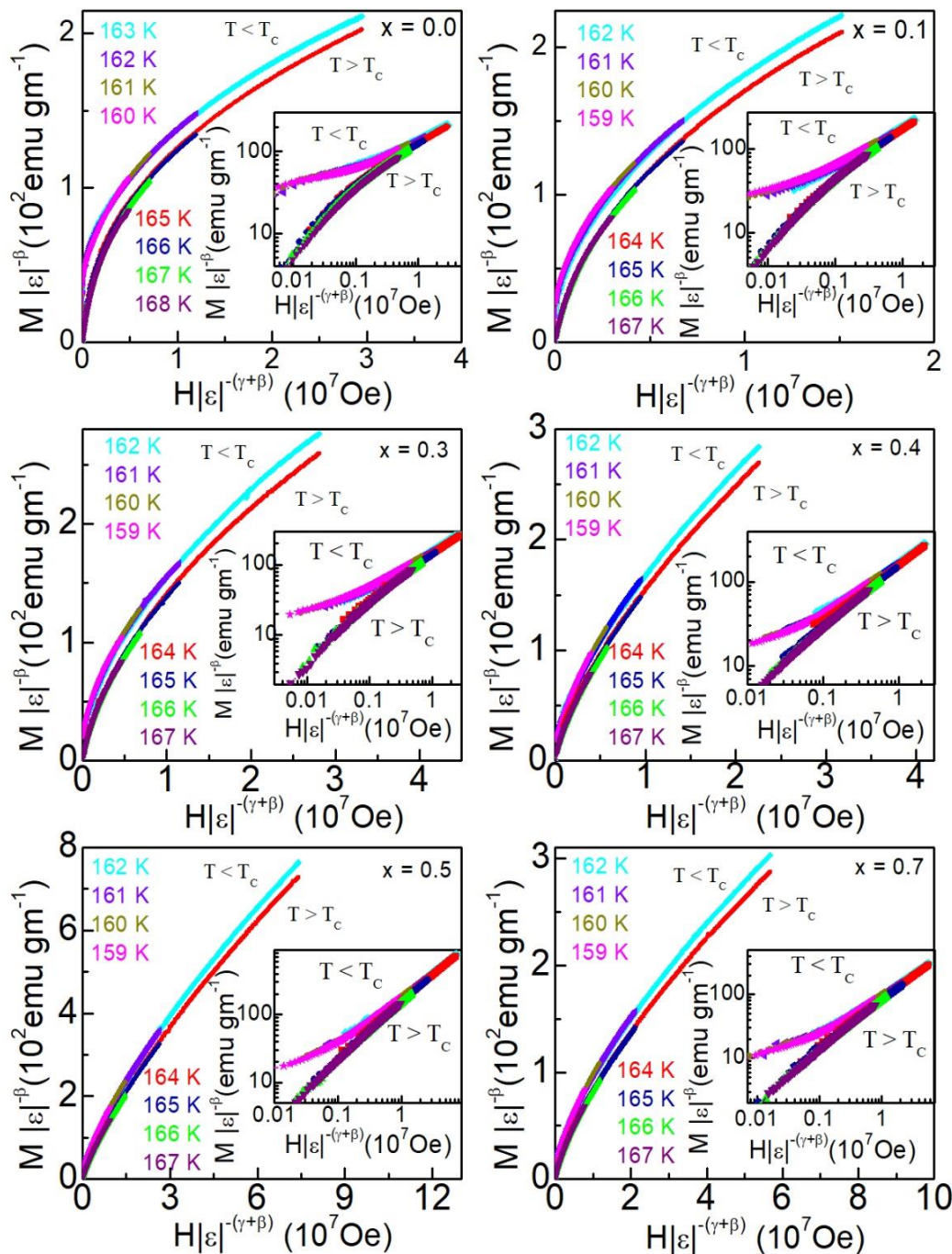


Figure 4.8 Renormalized magnetization $M|t|^{-\beta}$ has been plotted as a function of renormalized field $H|t|^{-(\gamma+\beta)}$ for isotherms both below and above T_c . Data are shown for $\text{SrRu}_{1-x}\text{Ti}_x\text{O}_3$ series with (a) $x = 0.0$ (b) $x = 0.1$ (c) $x = 0.3$ (d) $x = 0.4$ (e) $x = 0.5$ and (f) $x = 0.7$. Inset shows same plot in \log_{10} scale. Renormalized magnetization is merged into single line with renormalized field for isotherms both below and above T_c .

4.3.7 Evolution of exponents in $\text{SrRu}_{1-x}\text{Ti}_x\text{O}_3$

Our experimental data analysis show critical exponent β for SrRuO_3 is close to the mean-field value 0.5, however, exponents γ and δ show the values lower than those for mean-field model i.e., 1.0 and 3.0, respectively (see Table 4.1). For SrRuO_3 , we obtain $T_c \sim 164$ K which is very consistent with reported values for this material [1-3, 7, 13], even this T_c is one of the highest value obtained for this material. Our critical analysis interestingly shows that substitution of Ti has very little influence on T_c of SrRuO_3 as we find T_c remains almost unchanged. This conforms with our earlier study where we have explained this constant behavior of T_c in $\text{SrRu}_{1-x}\text{Ti}_x\text{O}_3$ considering opposite change of electron correlation U and density of states $N(\epsilon_F)$ that maintains T_c in picture of an itinerant ferromagnet.

Nonetheless, critical exponents show an unusual evolution where β increases and both γ and δ decreases with x (see Table 4.1). In Figure 4.9, we have shown an evolution of exponents β , γ , and δ with Ti (x) normalized by respective values for SrRuO_3 ($x = 0$). The figure shows that β continuously increases and γ , δ decreases till $x = 0.5$, though for $x = 0.7$ the values appear to show a reverse turn which may be related to metal-to-insulator transition around $x \sim 0.4$ in $\text{SrRu}_{1-x}\text{Ti}_x\text{O}_3$ series. Here, we mention that critical exponents and T_c are obtained using different independent techniques namely, MAF, KF plot and critical isotherm analysis, and they nicely agree. It can be noted that determined exponents and T_c fairly obey the scaling law behavior (Figure 4.8) for all the samples. Moreover, the Widom relation (Eq. 4.8), which demonstrates the relation among the critical exponents is nicely followed for entire range of Ti doping (Table 4.1). These attest to the fact that determined exponents and T_c are consistent and correct with experimental accuracy. These exponents show a steady variation and deviate from mean-field behavior with increasing x . However, the exponent values do not match with the predicted values for different known universality class models, also those cannot be explained with theoretical models available at hands for spin exchange interaction. Note, that similar kind of evolution of critical exponents (β , γ and δ) has been evidenced in $\text{Sr}_{1-x}\text{Ca}_x\text{RuO}_3$, however, the prominent difference is that T_c decreases to zero around 70% of

Ca doping resulting in quantum phase transition whereas T_c remains almost unchanged in present series [3, 6, 7].

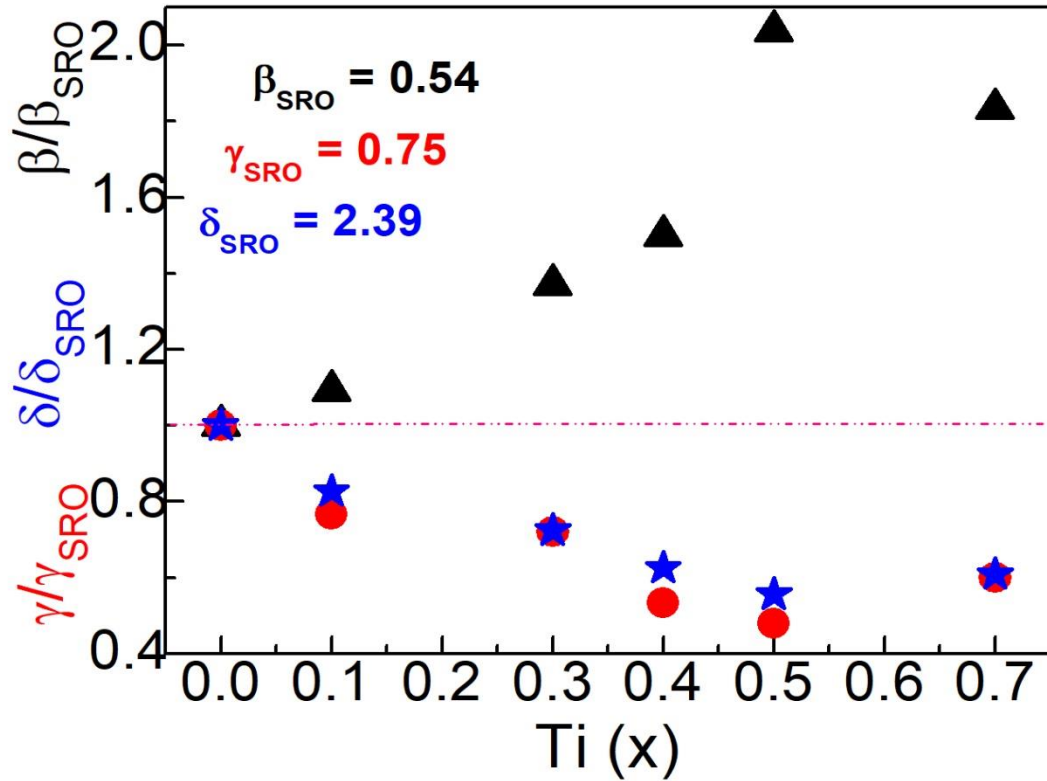


Figure 4.9 The critical exponents scaled by its values for $x = 0.0$ compound are shown as a function of composition (x) for $\text{SrRu}_{1-x}\text{Ti}_x\text{O}_3$ series.

In case of $\text{Sr}_{1-x}\text{Ca}_x\text{RuO}_3$, this particular evolution of exponents has been attributed to crossover from mean-field-like behavior to disorder-induced strong coupling regime arising from quantum fluctuations near quantum phase transition point by Fuchs *et al.*[3]. An another study reports that following of Arrott plot (signature of mean-field model) in SrRuO_3 may not be associated with the itinerant model of magnetism, rather this arises due to continuous curvature evolution from $\text{Sr}_{0.5}\text{Ca}_{0.5}\text{RuO}_3$ to SrRuO_3 to BaRuO_3 as induced by changes in lattice distortion and spin-orbit coupling effect [7]. These changes are responsible for band narrowing in $\text{Sr}_{1-x}\text{Ca}_x\text{RuO}_3$ which leads to phase segregation between strongly and weakly correlated phases. Hence exponents evolve accordingly. Here, it can be further noted that in heavy fermion compound $\text{URu}_{1-x}\text{Re}_x\text{Si}_2$, while though

exponent β remains constant, but the exponents γ and $(\delta - 1)$ decreases to zero as the QPT is approached with decreasing Re substitution around 15% [29].

While though the magnetic moment and the Curie-Weiss temperature decreases in $\text{SrRu}_{1-x}\text{Ti}_x\text{O}_3$ but the ferromagnetic T_c does not modify unlike in case of $\text{Sr}_{1-x}\text{Ca}_x\text{RuO}_3$ [3, 7, 14]. Moreover, minimum structural modification due to almost matching ionic size between Ru^{4+} and Ti^{4+} in present $\text{SrRu}_{1-x}\text{Ti}_x\text{O}_3$ series would unlikely cause these peculiar changes in exponents. This system, however, does not convert into first-order type PM-FM transition with Ti as seen from decreasing slope in $M(H)$ plot in Figure 4.2. Nonetheless, this unusual change in exponents (β , γ and δ) is quite intriguing as their values substantially depart from mean-field values ($\beta = 0.5$, $\gamma = 1.0$ and $\delta = 3.0$), and also from the values typically realized for classical ferromagnetic systems ($\beta < 0.5$, $\gamma > 1.0$ and $\delta > 3.0$).

We believe that Ti substituted at Ru-site dilutes the magnetic exchange path, and at a higher doping concentration of Ti the system develops into small-size magnetic clusters which are manifested through Griffiths phase like behavior, as reported in our earlier study [6]. This has another striking similarity with $\text{Sr}_{1-x}\text{Ca}_x\text{RuO}_3$ which also exhibits GP like behavior with progressive doping of Ca [7, 14]. The disorder is a prerequisite for the GP property which is provided by structural distortion in $\text{Sr}_{1-x}\text{Ca}_x\text{RuO}_3$ whereas site dilution achieved by Ti substitution acts as source of disorder in present $\text{SrRu}_{1-x}\text{Ti}_x\text{O}_3$. Henceforth, we speculate that the effect of disorder realized from both Ti as well as magnetic clusters can provide a possible explanation for this unusual change in critical exponents where β increases and both γ and δ decreases. The value of γ lower than unity in SrRuO_3 suggests parent $x = 0$ sample has some disorder or phase inhomogeneity above T_c . This effect of these changes in exponents is quite evident in Figure 4.1 where the PM-FM phase transition broadens with progressive Ti substitution. In fact, a recent optical spectroscopy study has shown the temperature dependence of optical conductivity spectra indicates itinerant-type FM in SrRuO_3 [30]. This study further demonstrates the non-vanishing local spin moment (sub-micron size) at $T > T_c$ (PM state) originating from local-band exchange splitting which is explained with

fluctuating local band theory. However, the net moment is realized to be zero due to spatial and temporal fluctuations of local bands. This needs to be understood whether this renders a constant T_c in present $\text{SrRu}_{1-x}\text{Ti}_x\text{O}_3$ series.

4.4 Conclusion

In summary, we have studied the critical behavior in perovskite based $\text{SrRu}_{1-x}\text{Ti}_x\text{O}_3$ as a function of Ti substitution using the standard methods such as modified Arrott plot, Kouvel-Fisher plot and critical isotherm analysis. We have estimated critical exponents β , γ , and δ where β increases and both γ and δ decreases with Ti substitution. The transition temperature T_c , however, remains almost unchanged with site dilution by Ti doping. The estimated exponents do not match with the values of any universality classes known for spin interaction models. Nonetheless, the exponents nicely obey the Widom relation as well as scaling behavior which attests to the fact that estimated exponents and T_c are consistent and accurate. The evolution of exponents of similar nature has been observed in isoelectronic doped $\text{Sr}_{1-x}\text{Ca}_x\text{RuO}_3$. This specific change of exponents is likely caused by disorders arising from magnetic clusters which originate due to site dilution with Ti substitution. The evolution of the Griffiths phase like behavior in present series as evidenced in our earlier study substantiates the formation of magnetic clusters and its influences on the magnetic behavior.

Bibliography

- [1]. P. B. Allen, H. Berger, O. Chauvet, L. Forro, T. Jarlborg, A. Junod, B. Revaz and G. Santi, *Phys. Rev. B*, **53**, 4393 (1996).
- [2]. G. Cao, S. McCall, M. Shepard, J. E. Crow and R. P. Guertin, *Phys. Rev. B*, **56**, 321 (1997).
- [3]. D. Fuchs, M. Wissinger, J. Schmalian, C. L. Huang, R. Fromknecht, R. Schneider and H. V. Lohneysen, *Phys. Rev. B*, **89**, 174405 (2014).
- [4]. I. I. Mazin and D. J. Singh, *Phys. Rev. B*, **56**, 2556 (1997).
- [5]. M. Kim and B. I. Min, *Phys. Rev. B*, **91**, 205116 (2015).
- [6]. R. Gupta and A. K. Pramanik, *J. Phys.: Condens. Matter*, **29**, 115801 (2017).
- [7]. J.G. Cheng, J.S. Zhou, J. B. Goodenough, and C.Q. Jin, *Phys. Rev. B*, **85**, 184430 (2012).
- [8]. D. Kim, B. L. Zink, F. Hellman, S. McCall, G. Cao, and J. E. Crow, *Phys. Rev. B*, **67**, 100406 (2003).
- [9]. R. Palai, H. Huhtinen, J. F. Scott, and R. S. Katiyar, *Phys. Rev. B*, **79**, 104413 (2009).
- [10]. Y. Kats, L. Klein, J. W. Reiner, T. H. Geballe, M. R. Beasley, and A. Kapitulnik, *Phys. Rev. B*, **63**, 054435 (2001).
- [11]. L. Klein, J. S. Dodge, C. H. Ahn, J. W. Reiner, L. Mieville, T. H. Geballe, M. R. Beasley and A. Kapitulnik, *J. Phys.: Condens. Matter*, **8**, 10111 (1996).
- [12]. L. M. Wang, H. E. Horng and H. C. Yang, *Phys. Rev. B*, **70**, 014433 (2004).
- [13]. C. Sow, D. Samal, P. S. Anil Kumar, A. K. Bera and S. M. Yusuf, *Phys. Rev. B*, **85**, 224426 (2012).

- [14]. C. Q. Jin, J. S. Zhou, J. B. Goodenough, Q. Q. Liu, J. G. Zhao, L. X. Yang, Y. Yu, R. C. Yu, T. Katsura, A. Shatskiy and E. Ito, *Proc. Natl Acad. Sci. USA*, **105**, 7115 (2008).
- [15]. E. C. Stoner, *Proc. R. Soc. London*, **169**, 339 (1939).
- [16]. Y. J. Chang, C. H. Kim, S. H. Phark, Y. S. Kim, J. Yu and T. W. Noh, *Phys. Rev. Lett.* **103**, 057201 (2009).
- [17]. J. Kim, J.Y. Kim, B.G. Park and S.J Oh, *Phys. Rev. B*, **73**, 235109 (2006).
- [18]. P.A. Lin, H.T. Jeng, and C.S. Hsue, *Phys. Rev. B*, **77**, 085118 (2008).
- [19]. J. A. Osborn, *Phys. Rev.*, **67**, 351 (1945).
- [20]. H. E. Stanley, *Introduction to phase transitions and critical phenomena*, Oxford University Press, London, 1971.
- [21]. A. Arrott, *Phys. Rev.*, **108**, 1394 (1957).
- [22]. A. Arrott and J. E. Noakes, *Phys. Rev. Lett.*, **19**, 786 (1967).
- [23]. A. K. Pramanik and A. Banejee, *Phys. Rev. B*, **79**, 204426 (2009).
- [24]. Imtiaz Noor Bhatti and A. K. Pramanik, *J. Magn. Magn. Mater.*, **422**, 141 (2017).
- [25]. J. S. Kouvel, and M. E. Fisher, *Phys. Rev.*, **136**, A1626 (1964).
- [26]. S. N. Kaul, *J. Magn. Magn. Mater.*, **53**, 5 (1985).
- [27]. B. Widom, *J. Chem. Phys.*, **43**, 3898 (1965); **41**, 1633 (1964).
- [28]. K.W. Kim, J.S. Lee, T.W. Noh, S.R. Lee, K. Char, *Phys. Rev. B*, **71**, 125104 (2005).
- [29]. N. P. Butch and M. B. Maple, *Phys. Rev. Lett.*, **103**, 076404 2009.
- [30]. D.W. Jeong, H.C. Choi, C.H. Kim, S.H. Chang, C.H. Sohn, H.J. Park, T.D. Kang, D.Y. Cho, S.H. Baek, C.B. Eom, J.H. Shim, J. Yu, K.W. Kim, S.J. Moon, T.W. Noh, *Phys. Rev. Lett.*, **110**, 247202 (2013).

Chapter 5

Effects of Site dilution and Ru-charge modulation on physical properties in $\text{SrRu}_{1-x}\text{Ga}_x\text{O}_3$

In this chapter, we report the evolution of structural, magnetic and transport behavior of $\text{SrRu}_{1-x}\text{Ga}_x\text{O}_3$ series ($x \leq 0.2$) where the doped $\text{Ga}^{3+}(3d^{10})$ not only acts for site dilution but also it modifies the Ru charge state from Ru^{4+} to Ru^{5+} . Unlike Ti^{4+} substitution which does not change the Ru charge state. The Ga^{3+} substitution does not affect the original orthorhombic $Pbnm$ structure of SrRuO_3 due to its matching ionic radii with Ru^{4+} . However, the lattice parameters show a decrease due to smaller ionic radii of generated Ru^{5+} . The Ga^{3+} has a substantial effect on the magnetic behavior including the magnetic moment and magnetic phase transition. The Ga^{3+} substitution further induces an insulating behavior in SrRuO_3 . We have done a detailed analysis of the charge transport mechanism in present series in whole temperature range across the magnetic transition temperature (T_c).

5.1 Introduction

As already has been discussed that at low temperature, the magnetic nature of SrRuO_3 shows itinerant ferromagnetic type with $T_c \sim 163$ K [1-4]. We have seen the structure and magnetic behavior of SrRuO_3 by nonmagnetic substitution of Ti^{4+} [5].

In this chapter, we have studied the evolution of magnetic and electron transport behavior with of another nonmagnetic Ga^{3+} which has electronic configuration of $3d^{10}$. The Ga^{3+} has ionic radii (0.62 \AA) which closely match with that for Ru^{4+} (0.62 \AA), therefore this substitution is expected to introduce minimum structural modification. The nonmagnetic

character of Ga^{3+} will act for dilution of magnetic lattice similar to Ti^{4+} . However, Ga^{3+} will have added effect where it will convert an equivalent amount of Ru^{4+} to Ru^{5+} . Henceforth, in the present series, there will be a mixture of Ru^{4+} and Ru^{5+} which will influence the magnetic interaction accordingly. The possible magnetic interaction path will be $\text{Ru}^{4+}\text{-O-Ru}^{4+}$, $\text{Ru}^{4+}\text{-O-Ru}^{5+}$, and $\text{Ru}^{5+}\text{-O-Ru}^{5+}$. Hence, an interaction in magnetic and transport behavior has expected in the present study with Ga substitution.

We have tried to understand the effect of Ga^{3+} substitution for the magnetic property of SrRuO_3 through studying the temperature dependent magnetization measurement under ZFC-FC protocol. The low temperature demagnetization effect, critical exponent close to T_c , high temperature $M(T)$ data in PM state, Griffiths singularity and magnetic hysteresis $M(H)$ at low temperature has analyzed. We find overall magnetic moment decreases with Ga substitution and the magnetic data in PM state follows CWL. The analysis of low temperature demagnetization data indicates the presence of both localized and itinerant type magnetism. Critical behavior analysis implies a mean field (β) type behavior, however, β continuous increases with Ga doping.

While the charge transport mechanism in high temperature PM state follows modified Mott VRH model, the same in FM state shows a FL type behavior where the temperature range for the validity of FL behavior enhances with Ga doping.

5.2 Experimental Details

Polycrystalline series of samples $\text{SrRu}_{1-x}\text{Ga}_x\text{O}_3$ with nominal compositions ($x = 0.0, 0.05, 0.1$ and 0.2) have been synthesized following standard solid state reaction method. High purity ($> 99.99\%$) ingredient materials such as SrCO_3 , RuO_2 and Ga_2O_3 are mixed well in stoichiometric ratio and heated at 1000°C in the air for 24 hours twice with intermediate grinding. Then, powders are pressed into pellets and heated at 1100°C for 36 hours. Details of sample preparation and analysis are given elsewhere [5]. Sample quality has been checked with powder X-ray diffraction (XRD) and Rietveld analysis [6]. XRD data are collected using Rigaku MiniFlex diffractometer with CuK_α radiation in the 2θ range from 10 to 90° at room temperature. The recorded XRD patterns were evaluated using Rietveld refinement analysis by the FullProf software. Temperature (T) and magnetic

field (H) dependent magnetization (M) data are collected using a superconducting quantum interference device (SQUID) magnetometer by Quantum Design. The electrical resistivity ρ (T) of the present series is measured by a home-made instrument using the four-probe method.

5.3 Results and Discussions

5.3.1 Structural study

The room temperature XRD patterns of present series are shown in figure 5.1(a). As seen in the figure, XRD pattern do not modify with Ga composition in terms of peak position or additional impurity peak(s). We have previously shown that parent SrRuO₃ crystallizes in GdFeO₃-type orthorhombic structure with $Pbnm$ symmetry in agreement with reported studies [5, 7, 8]. We find that the original orthorhombic- $Pbnm$ structure is continued for whole series. Figure 5.1(b) shows representative Rietveld analysis of XRD data for doped $x = 0.2$ sample with is the last member of the present series. The Rietveld refinement shows a reasonably good fitting of XRD data for SrRu_{0.8}Ga_{0.2}O₃ with orthorhombic- $Pbnm$ structure. Here it can be mentioned that we obtain fitting indicator such as, χ^2 value about 1.74, 1.97, 1.41 and 1.74 for $x = 0.0, 0.05, 0.1$ and 0.2 of present series which suggests a reasonably good fitting. Our Rietveld fitting is evaluated with 'Goodness of fitting' parameter (R_{wp}/R_p) which yields values around 1.25 which further indicates a good fitting. However, given that Ga⁺³ and Ru⁺⁴ has matching ionic radii (0.62 Å), therefore it is least expected for major structural modification in the present series.

Table 5.1 The structural parameters of SrRu_{1-x}Ga_xO₃ series with compositions $x = 0.0, 0.05, 0.1$ and 0.2 in terms of structural parameters a, b, c , unit cell volume (V) and basal bond length (Ru-O1), apical bond length (Ru-O2), basal bond angle (Ru-O1-Ru) and apical bond angle (Ru-O2-Ru)

Ti(x)	0.0	0.05	0.1	0.2
a (Å)	5.5733(2)	5.5744(2)	5.5678(2)	5.5662(4)
b (Å)	5.5336(2)	5.5379(2)	5.5311(2)	5.5307(4)

<i>c</i> (Å)	7.8475(3)	7.8482(4)	7.8377(3)	7.8293(7)
<i>V</i> (Å³)	242.02(1)	242.28(2)	241.37(2)	241.03(3)
Ru-O1 (Å)	1.9984(1)	1.9936(1)	1.9928(1)	1.9789(1)
Ru-O2 (Å)	1.9665(1)	1.9704(1)	1.9613(1)	1.9587(2)
Ru-O1-Ru	158.482(1)	160.359(2)	159.772(2)	164.865(3)
Ru-O2-Ru	172.148(1)	169.465(1)	174.945(1)	175.701(2)

Table 5.1 shows the evolution of structural parameters with Ga substitution which are obtained from Rietveld analysis. The lattice parameters *a*, *b* and *c* and volume *V* show a slight increase for *x* = 0.05, but then values decrease with higher doping concentration. This evolution in lattice parameters can be understood from ionic distribution. The substitution of Ga⁺³ will equivalently generate Ru⁺⁵ (0.565 Å) which has comparatively lower ionic radii than Ru⁺⁴. Therefore, for initial doping concentration the lattice parameters increase till *x* = 0.05 due to the presence of Ga⁺³. In higher doping concentration, however, Ru⁺⁵ dominates which lead to decreasing lattice parameters that ultimately affects the unit cell volume *V*. We have calculated the percentage change in structural parameters of SrRu_{1-x}Ga_xO₃ series such as, Δ*a*, Δ*b*, Δ*c* and Δ*V* with values 0.007, 0.003, 0.018 and 0.99%, respectively. The changes in respective values are very minimal which follows our expectation due to matching ionic radii. We also observe the change in RuO₆ parameters. The SrRuO₃ adopts a GdFeO₃ crystal structure where RuO₆ octahedra demonstrate distortion both along ab-plane as well as along *c*-direction which causes the basal and apical Ru-O-Ru bond angle to deviate from the ideal condition. Table 5.1 shows that both the basal Ru-O1 and apical Ru-O2 bond-length decreases in agreement with changes in lattice parameters. The basal (<Ru-O1-Ru>) and apical (<Ru-O2-Ru>) bond-angle for SrRuO₃ in Table 5.1 agree with reported values and implies RuO₆ octahedra are both rotated and tilted along *c*-axis. With Ga substitution, both the bond-angle increases toward ideal value of 180° suggesting octahedral distortion is relieved progressively.

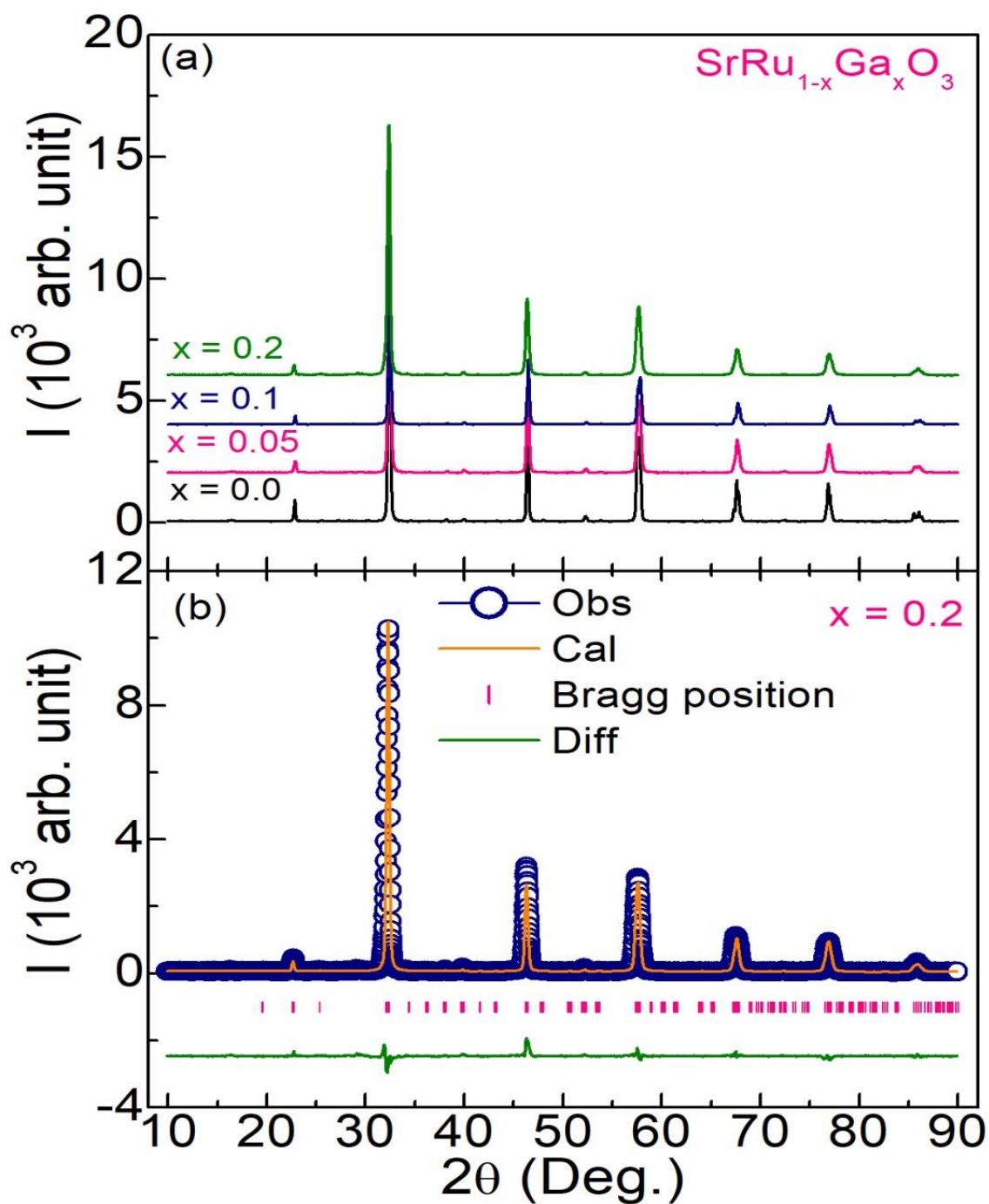


Figure 5.1 (a) The room temperature powder XRD patterns of polycrystalline samples of $\text{SrRu}_{1-x}\text{Ga}_x\text{O}_3$ series with compositions of $x = 0.0, 0.05, 0.1$ and 0.2 (b) The XRD pattern along with Rietveld refinement analysis of $\text{SrRu}_{0.8}\text{Ga}_{0.2}\text{O}_3$ with the orthorhombic $Pbnm$ structure at room temperature.

5.3.2 Magnetization study for $\text{SrRu}_{1-x}\text{Ga}_x\text{O}_3$ series

The temperature dependent magnetization data measured in 100 Oe following zero field cooling (ZFC) and field cooling (FC) are shown in figure 5.2(a) for $\text{SrRu}_{1-x}\text{Ga}_x\text{O}_3$ series.

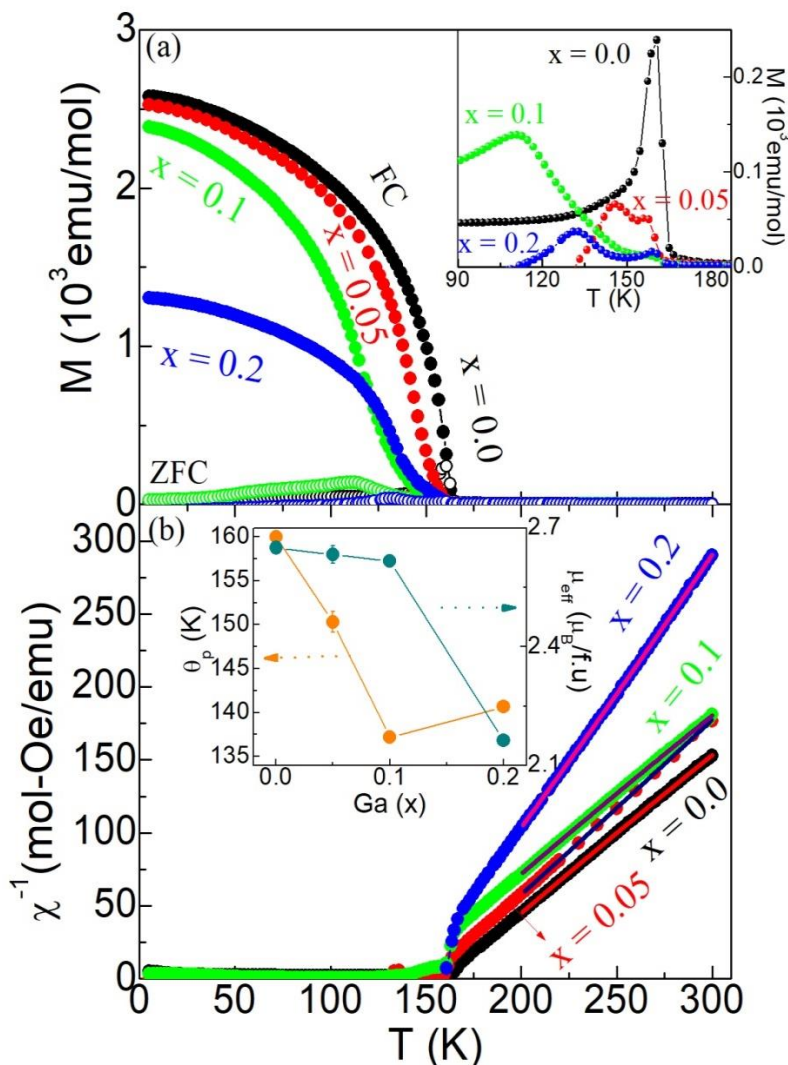


Figure 5.2 (a) The temperature dependent dc magnetization from 5 K to 300 K in the form of M_{ZFC} and M_{FC} protocol at 100 Oe of magnetic field as function of temperature of $\text{SrRu}_{1-x}\text{Ga}_x\text{O}_3$ series with compositions $x = 0.0, 0.05, 0.1$ and 0.2 . The inset shows M_{ZFC} highest peak close to T_c (b) The inverse susceptibility ($\chi^{-1} = H/M$) plot with modified Curie-Weiss Law fitting in the temperature range of 200 K to 300 K of $\text{SrRu}_{1-x}\text{Ga}_x\text{O}_3$ series; the solid line is linear fitting. In the inset, left axis shows the Curie temperature (θ_p) variation by Ga doping of $\text{SrRu}_{1-x}\text{Ga}_x\text{O}_3$ series and right axis shows effective PM moment variation by Ga doping of $\text{SrRu}_{1-x}\text{Ga}_x\text{O}_3$ series.

The SrRuO₃ is well documented itinerant type FM with transition temperature $T_c \sim 162$ K. Inset of figure 5.2(a) shows a close view of $M_{ZFC}(T)$ for all the samples across the transition temperature. We observe that M_{ZFC} for parent SrRuO₃ shows a peak around 163 K and the bifurcation between M_{ZFC} and M_{FC} starts around this temperature (figure 5.2(a)). In fact, SrRuO₃ exhibits large bifurcation between ZFC and FC magnetization data which is suggestive of large anisotropy in this material [9, 10]. In doped samples, while though onset temperature for bifurcation remains almost the same, but the amount of bifurcation reduces substantially.

This result is similar to Ti doped samples where recently we have shown the long-range ordering temperature T_c remains almost unchanged till 70% of Ti substitution which has been explained from opposite tuning of electron correlation and density of states with Ti doping [5]. The present series, however, differs from the Ti doped one as Ga⁺³ not only act for site dilution but it creates Ru⁺⁵ which is magnetic and participates in magnetic interaction with existing Ru⁺⁴ ions. It is evident in inset of figure 5.2(a) that below T_c , the M_{ZFC} shows another peak at different temperatures which may originate from magnetic clustering effect.

To understand the high temperature paramagnetic (PM) state, inverse susceptibility ($\chi^{-1} = (M/H)^{-1}$) as deduced from magnetization data in figure 5.2(a), is shown in figure 5.2(b). The $\chi^{-1}(T)$ in PM regime shows linear behavior close to T_c for all the samples which implies Curie-Weiss (CW) behavior is followed in PM state. The $\chi^{-1}(T)$, however, shows sharp downturn close to T_c in higher doped samples which are analyzed in terms of Griffiths phase behavior (discussed later). The $\chi^{-1}(T)$ data have been analyzed with modified Curie-Weiss (CW) law as following,

$$\chi(T) = \chi_0 + \frac{C}{T - \theta_p} \quad (5.1)$$

where χ_0 is the temperature independent susceptibility, C is the Curie constant and θ_p is Curie temperature. Figure 5.2(b) shows $\chi^{-1}(T)$ data have been fitted with eq. (5.1) in high temperature regime down to 200 K indicating reasonably good fitting. The fitting yields $\chi_0 = 2.56 \times 10^{-4}$ emu mole⁻¹Oe⁻¹, $C = 0.88$ emu K mole⁻¹ Oe⁻¹ and $\theta_p = 160$ K for

SrRuO₃. The positive sign of θ_p is showing that the interaction between Ru ions is of FM type [1, 11]. Using the above value of Curie constant, we have calculated the effective PM moment (μ_{eff}) which is 2.65 $\mu_B/\text{f.u.}$ for SrRuO₃ which closely matches with the reported values [2, 12-14]. The obtained value is also close to the theoretically calculated value (for spin-only $g\sqrt{S(S+1)}\mu_B$) of 2.83 $\mu_B/\text{f.u.}$ for SrRuO₃ with $S = 1$. The inset of figure 5.2(b) shows the variation of θ_p (left axis) and μ_{eff} (right axis) with x . The θ_p initially decreases till $x = 0.1$ but then shows slight increase for $x = 0.2$. While θ_p remains positive throughout the series but this nonmonotonic behavior may be related to change in Ru⁺⁴/Ru⁺⁵ ratio with x . The μ_{eff} , on the other hand, decreases linearly till $x = 0.1$ and then shows a steep decrease. As discussed, doped Ga⁺³ ($S = 0$) converts Ru⁺⁴ ($S = 1$) to Ru⁺⁵ ($S = 3/2$), therefore, overall μ_{eff} of the sample can be expressed as, $\mu_{\text{eff}} = g\sqrt{\left[(1-2x)(\mu_{\text{eff}}^{S=1})^2 + x(\mu_{\text{eff}}^{S=3/2})^2\right]}\mu_B$. The calculation shows overall μ_{eff} continuously decreases which agrees with our experimental values of μ_{eff} .

5.3.3 Thermal Demagnetization study

The thermal demagnetization of FM materials at low temperature is of particular interest. Usually, for exchange interaction driven FM systems, the thermal demagnetization is explained by Bloch's spin-wave (SW) analysis which is expressed in following (neglecting higher order terms) [15],

$$M(T) = M(0)[1 - BT^{3/2}] \quad (5.2)$$

where $M(0)$ is the zero temperature magnetization and $T^{3/2}$ term comes from long wavelength q^2 harmonic term [16]. Using the spin-wave coefficient 'B', spin-wave stiffness constant D can be calculated as;

$$D = \frac{k_B}{4\pi} \left[\frac{\zeta(3/2)g\mu_B}{M(0)\rho B} \right]^{2/3} \quad (5.3)$$

where k_B , g , μ_B and ρ are the Boltzmann constant, Lande g -factor, Bohr magneton and density of material respectively and $\zeta(3/2) = 2.612$. Similarly, Stoner single-particle (SP) excitations have been used to understand the low temperature demagnetization of itinerant FM where the origin of FM is associated with the splitting of the band into spin-

up and spin-down sub-bands separated by exchange energy [17]. The energy difference between the two sub-bands is proportional to spontaneous magnetization (M_s). The generalized form of Stoner's single-particle excitations is given below,

$$M(T) = M(0) \left[AT^n e^{\left(-\frac{\Delta}{k_B T}\right)} \right] \quad (5.4)$$

where 'A' is the single-particle excitation coefficient, and Δ is the energy gap between the top of full sub-band and Fermi level. The itinerant FM can be divided into two categories based on n and Δ . For example, $n = 2$ and $\Delta = 0$ gives a weak-type itinerant FM where both the sub-bands are partially filled and the Fermi level stays within both the sub-bands. On the other hand, a strong-type itinerant FM is realized for $n = 3/2$ and $\Delta \neq 0$ where one sub-band is partially filled and another one is fully filled. As the spin-polarization of SrRuO₃ is reported less than 100%, therefore a weak-type itinerant FM is expected in this material with following temperature dependence,

$$M(T) = M(0)[AT^2] \quad (5.5)$$

We have tried to fit the low temperature $M(T)$ data, using both spin-wave (SW) and single-particle (SP) model separately has shown in insets of figure 5.3. However, the thermal demagnetization data can be better fitted using combination of both the SW and SP model which takes account both the localized as well as an itinerant model of magnetism with eq. (5.6) as given below [18, 19],

$$M(T) = M(0)[1 - BT^{3/2} - AT^2] \quad (5.6)$$

Our recent study has shown low temperature thermal demagnetization in SrRu_{1-x}Ti_xO₃ can be better explained taking account of both SW and SP model which is also in line with a recent theoretical calculation which suggests a coexistence of localized and itinerant magnetism in SrRuO₃ [5]. Figure 5.3 shows the temperature dependent magnetization data in low temperature FM phase and the solid lines are due to the best fitting of $M(T)$ data up to ~ 65 K where the fitting of $M(T)$ data is shown with only spin-wave model [Eq. (5.2), upper inset], single-particle model [Eq. (5.5), lower inset] and combined model [Eq. (5.6), main panel] for SrRuO₃. As evident in the figure, the eq. (5.6) gives better fitting in wide temperature range which is also validated by higher χ^2

value. Here, it can be mentioned that we have previously shown that low temperature demagnetization in SrRuO₃ can be explained counting contribution from both spin-wave and single-particle model. The fitting in figure 5.3 gives fitted parameters of constants $M(0)$, B and A to be $0.463 \mu_B/\text{f.u.}$, $9.0 \times 10^{-5} \text{ K}^{-3/2}$ and $1.17 \times 10^{-5} \text{ K}^{-2}$, respectively for SrRuO₃ [20]. The observation shows that the spin-wave excitations give the dominant contribution to the thermal demagnetization effect in SrRuO₃. The spin-wave stiffness constant D has been calculated using the fitted parameter B from Eq. (5.3) and we obtain $D = 264.9 \text{ meV \AA}^2$ for SrRuO₃.

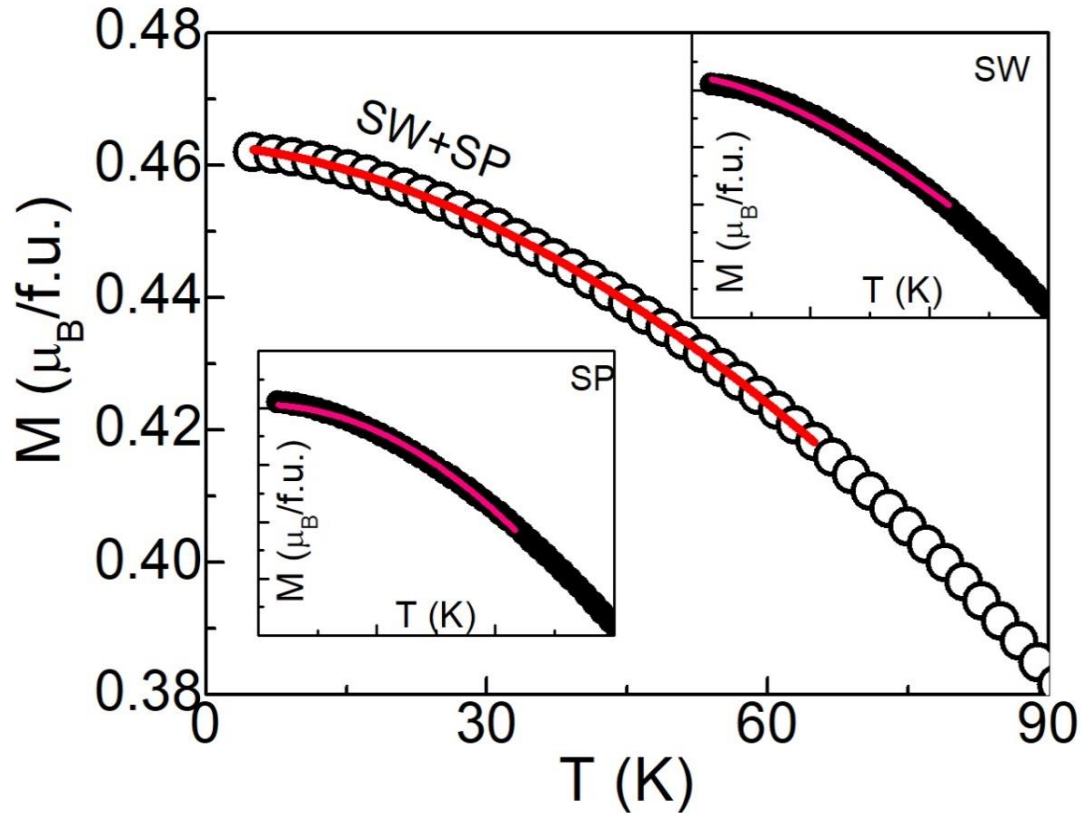


Figure 5.3 The spin-wave and single particle combined fitting of SrRuO₃ and the upper inset shows only spin wave fitting while lower inset shows only single particle fitting of SrRuO₃.

The magnetic exchange coupling constant (J) between nearest-neighbor magnetic atoms has also been calculated using the following equation [21]

$$J = \frac{k_B}{2S} \left[\frac{0.0587}{BS} \right]^{2/3} \quad (5.7)$$

where $S (=1)$ is the localized atomic spin and for SrRuO₃. The value of J comes out to be $37.6 k_B$. For the doped materials in SrRu_{1-x}Ga_xO₃ series, we find similar dual model is required to understand the low temperature demagnetization effect. According to band magnetism model, if the spontaneous moment M_s decreases, then the exchange splitting will also be decreased by $\Delta E = IM_s / N\mu_B$, where N is the number of spins per unit volume and I is the Stoner parameter of spin-up and spin-down ‘ d ’ sub-bands. In present series, the M_s decreases with Ga doping, therefore, it is believed that Fermi level E_F lies within the d_{\downarrow} and d_{\uparrow} sub-bands for all the samples, which suggests both spin-wave, as well as single-particle models, would be required to explain the thermal demagnetization effect [22].

The calculated D and J have been shown in Table 5.2 for present SrRu_{1-x}Ga_xO₃ series. The SW stiffness constant D decrease till $x \sim 0.1$ and then it increases for $x = 0.2$. Here, it can be mentioned that we find an increasing D value in other non-magnetic Ti⁴⁺ doped systems SrRu_{1-x}Ti_xO₃ where the opposite evolution of D in both series is believed it arise due to change of Ru⁴⁺ ionic state on Ga doped series where in Ti doped series the Ru⁴⁺ charge state does not alter with doping. However, for Ga doping with $x = 0.2$, the D shows an increase which may be due to an interplay between site dilution caused by Ga³⁺ doping and changing ionic state of Ru from Ru⁴⁺ to Ru⁵⁺.

Table 5.2 The characteristic random critical temperature T_c^R (K), the inverse susceptibility exponent λ , Griffiths temperature (T_G) and the range of Griffiths temperature defined as $[(T_G - T_c)/T_c] \times 100$ of SrRu_{1-x}Ga_xO₃ series by dc magnetization.

Ti(x)	0.0	0.05	0.1	0.2
T_c (K)	161	146	111	133
T_c (K)			169	173
T_c^R (K)			134	144.7
λ_{PM}			0.004	0.002
λ_{GP}			0.846	0.944

GP(%T_c)			52	30
$M_r(\mu_B/f.u)$	0.69	0.61	0.55	0.38
q_c/q_s	1.47	1.63	1.81	1.82
D (meVÅ²)	264.9	206.6	179.2	327.0
J (k_BK)	37.6	28.9	23.1	28.2

5.3.4 Critical exponent behavior

The nature of magnetic interaction in magnetic materials is usually characterized by universality which is associated with different values of critical exponents [23]. These universality classes do not depend on microscopic details of materials; rather those are defined by lattice dimension (d) and spin dimension (n). The temperature dependent magnetization in vicinity of T_c obeys following equation,

$$M(T) = M_0 (T_c - T)^\beta \quad (5.8)$$

where β is the critical exponent and M_0 is the magnetization at zero K. The $M(T)$ data have been fitted with Eq. (5.8) close to T_c .

In the fitting, the M_0 , T_c and β have been kept as free parameters and have been determined from fitting in figure 5.4. The obtained values of M_0 , T_c and β for SrRuO₃ are 309.57 emu mol⁻¹, 162 K and 0.48(2), respectively, which implies a mean-field type behavior in SrRuO₃ [24]. This behavior is consistent with other reported studies [25, 26]. The values of β as a function of Ga doping are shown in inset of figure 5.4. It is clear in the figure that the β increases monotonically with Ga, reaching the value ~ 0.696 for $x = 0.2$ in SrRu_{1-x}Ga_xO₃ series. The similar behavior has also obtained in nonmagnetic Ti doping at Ru site in SrRu_{1-x}Ti_xO₃ series. This increase in value of β with Ga substitution is probably caused by formation of FM clusters across T_c as explained in case of Ti substitution in SrRuO₃ [5].

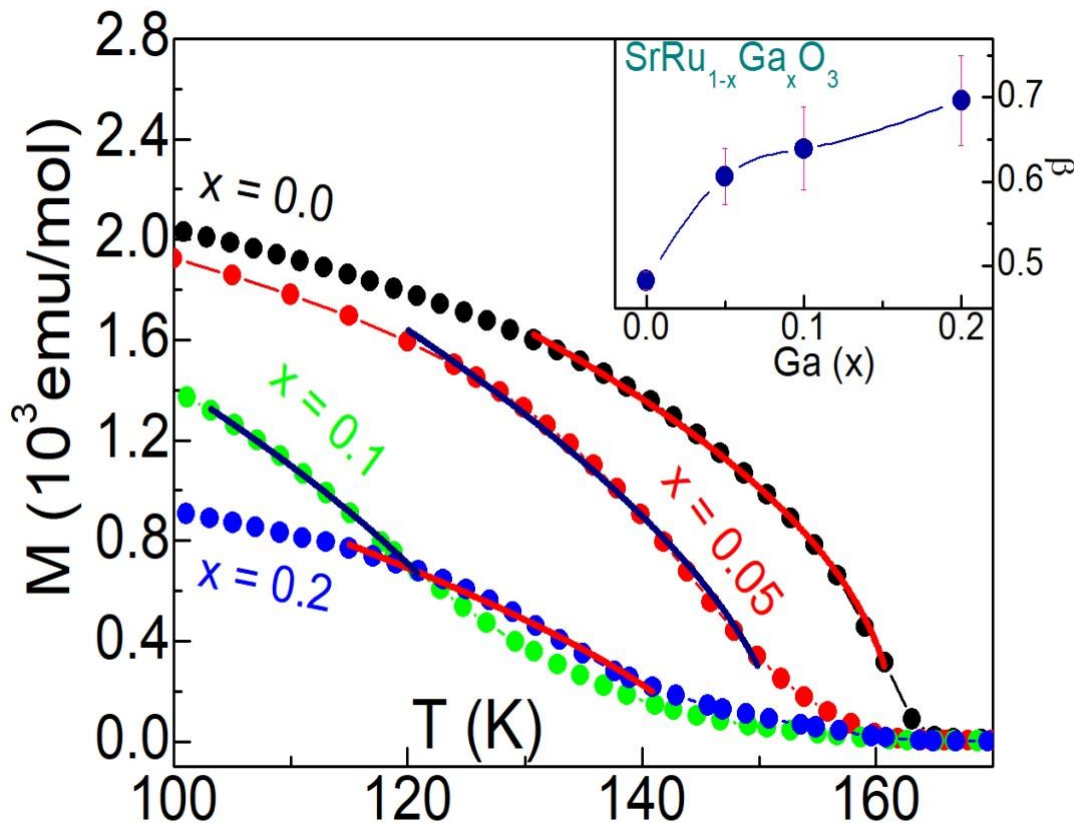


Figure 5.4 The critical exponent (β) fitting close to T_c of $\text{SrRu}_{1-x}\text{Ga}_x\text{O}_3$ series and the inset shows a variation of β by Ga doping of $\text{SrRu}_{1-x}\text{Ga}_x\text{O}_3$ series.

5.3.5 Griffiths Phase behavior

The Griffiths phase (GP) like behavior originates from local disorder present in crystallographic structure and magnetic interactions. The GP behavior is mainly characterized by formation ferromagnetic clusters at temperatures higher than the T_c . The inverse magnetic susceptibility (χ^{-1}) plotted as a function of temperature shows a sudden downturn in the case of GP [27]. Figure 5.5(a) shows inverse susceptibility (χ^{-1}) with the variation of temperature for $\text{SrRu}_{1-x}\text{Ga}_x\text{O}_3$ series. The $\chi^{-1}(T)$ data for higher doped samples show a downturn just above T_c which implies a signature of Griffiths phase (GP) like behavior. The temperature where $\chi^{-1}(T)$ data show an onset of downturn is termed as Griffiths temperature (T_G) and the temperature range between T_G and T_c is called GP regime where the system neither exhibits ideal FM order nor PM behavior, rather in this

regime there exists ferromagnetically ordered finite-size clusters embedded in PM background [28]. Due to the presence of clusters, the magnetization shows nonanalytic behavior, so the susceptibility diverges which is reflected in a sharp downturn in χ^{-1} [28, 29]. The sudden and sharp downfall of $\chi^{-1}(T)$ above T_c in the GP regime is characterized by the following relation [30]:

$$\chi^{-1} = (T - T_c^R)^{1-\lambda} \quad (5.9)$$

where T_c^R is the random critical temperature where the magnetic susceptibility diverges which generally lies between the T_c and (T_G) .

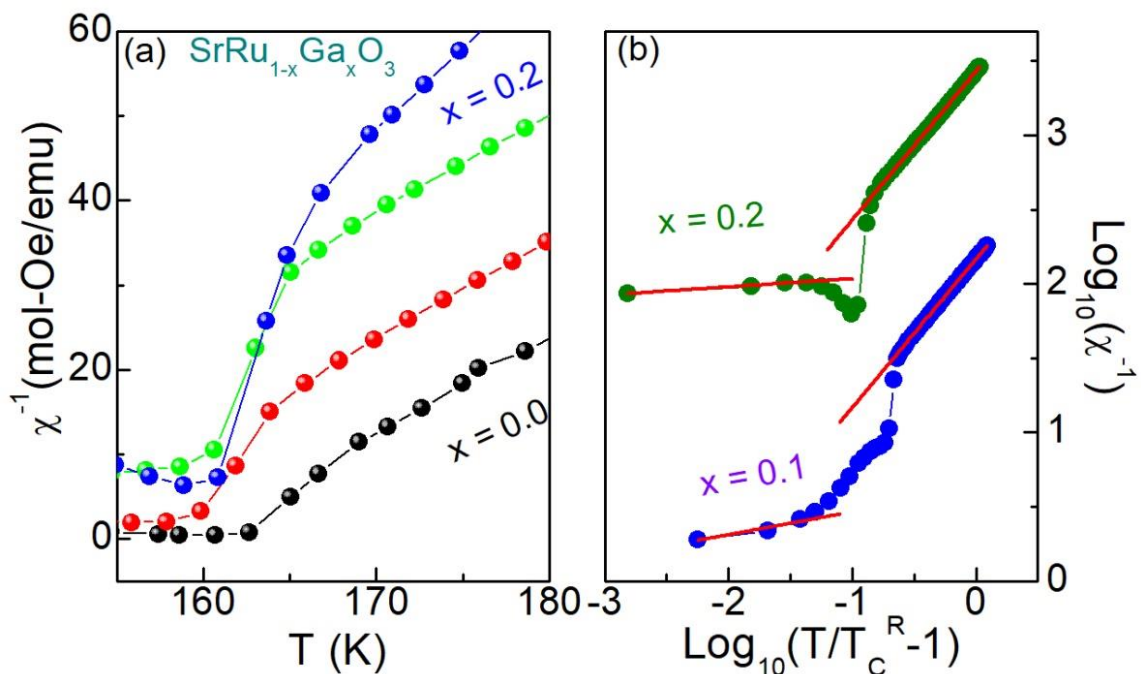


Figure 5.5 (a) The χ^{-1} with the variation of temperature of $\text{SrRu}_{1-x}\text{Ga}_x\text{O}_3$ series in PM state close to phase transition (b) The \log_{10} - \log_{10} scale fitting of Eq. (5.9) of $\text{SrRu}_{1-x}\text{Ga}_x\text{O}_3$ series with $x = 0.1$ and 0.2 . This plot of $x = 0.2$ samples has shifted upward by +1 for clarity.

The choice of proper T_c^R is very important for the correct evaluation of exponent λ . This power law behavior appears a modified form of the CW equation where the finite λ arises due to FM cluster formation. The λ value lies in the range of 0 to 1. In the PM region the value of λ is realized to be 0, hence the eq. (5.9) reduces to the standard CW equation. In the GP regime the χ^{-1} follows the modified CW behavior i.e., eq. (5.9) with

non-zero value of λ . Figure 5.5(b) shows semi-log fitting of eq. (5.9) both in paramagnetic as well as in GP regime for $x = 0.1$ and 0.2 samples of SrRu_{1-x}Ga_xO₃ series. The straight line fitting in figure 5.5(b) confirms GP like behavior in present series as similar to previous Ti doped samples. The obtained values of T_c^R , λ_{GP} and λ_{PM} of doped samples are given in table 5.2. The high value of λ in GP phase indicates the stronger behavior of GP in these materials. The increase of λ_{GP} indicates the sizes of FM clusters decreases with Ga doping.

5.3.6 Isothermal Magnetization study

Figure 5.6(a) shows the field dependent isothermal magnetization $M(H)$ data collected at 5 K for SrRu_{1-x}Ga_xO₃ series. The data have been collected with a field cycling of ± 70 kOe. The parent SrRuO₃ shows large hysteresis with coercive field (H_c) ~ 4800 Oe [31]. Even at high magnetic field, SrRuO₃ does not exhibit sign of saturation which is due to itinerant nature of magnetism [1]. At 70 kOe, we obtain magnetic moment $\mu_H = 1.25 \mu_B/\text{f.u.}$ which is less than the calculated value ($gS\mu_B = 2 \mu_B/\text{f.u.}$ with $S = 1$), g is the Lande g -factor. The non-saturation nature of $M(H)$ data till an applied field of 70 kOe is interesting. The variation of remnant magnetization (M_r) has given in Table 5.2. The lower inset of figure 5.6(a) shows variation of H_c with Ga doping for SrRu_{1-x}Ga_xO₃ series. The H_c initially decreases up to $x \sim 0.1$ and after that H_c increases with Ga doping. This behavior again appears connected to the competition between site dilution effect caused by nonmagnetic Ga³⁺ and mixed ionic states of Ru⁴⁺ and Ru⁵⁺. The inset of figure 5.6(b) shows the magnetic moment (μ_H) value experimentally found at the highest applied field of 70 kOe by Ga substitution. Both the observed and calculated (not shown) values of μ_H decrease with Ga doping in SrRu_{1-x}Ga_xO₃ series, where the agreement between the values are satisfactory.

The nature of the magnetic state in SrRuO₃ and its evolution with Ga substitution has been checked with Arrott plot which is above of plotting the magnetic isotherm $M(H)$ data in the form of M^2 vs H/M [32]. Figure 5.6(b) shows Arrott plot for SrRu_{1-x}Ga_xO₃ series with varying Ga doping concentration. The Arrott plot is constructed using $M(H)$ data from figure 5.6(a).

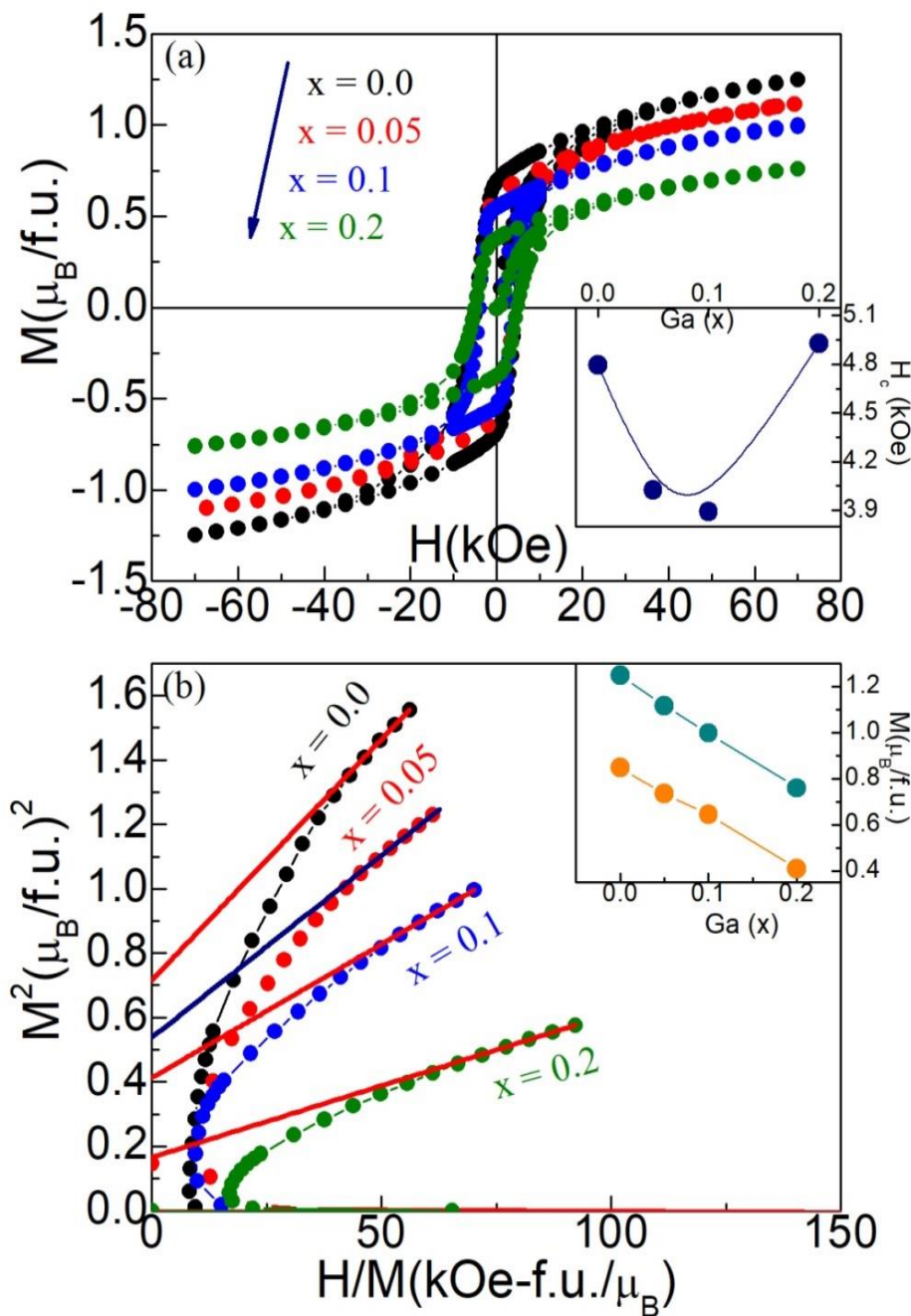


Figure 5.6 (a) The magnetic field dependent iso-thermal magnetization at 5 K is shown for $\text{SrRu}_{1-x}\text{Ga}_x\text{O}_3$ series with $x = 0.0, 0.05, 0.1$ and 0.2 . The inset shows coercive field (H_c) by Ga doping variation in $\text{SrRu}_{1-x}\text{Ga}_x\text{O}_3$ series (b) The Arrott plot (M^2 vs H/M) of magnetization $M(H)$ data at 5 K for $\text{SrRu}_{1-x}\text{Ga}_x\text{O}_3$ series and inset shows the saturation magnetization (μ_H) at 7 T and spontaneous magnetization (M_s) by Ga doping in $\text{SrRu}_{1-x}\text{Ga}_x\text{O}_3$ series.

The significance of the Arrott plot is that positive intercept on M^2 axis due to straight line fitting in high field regime gives spontaneous magnetization (M_s) which is the signature of ferromagnetic nature. Figure 5.6(b) shows the Arrott plot forms non-linear behavior with concave nature. However, the straight lines fitted in high field regime give positive intercept for all the samples. Considering that intercept presents M_s in the Arrott plot, we obtain $M_s = 0.846 \mu_B/\text{f.u.}$ for SrRuO₃. With Ga doping, M_s decreases in SrRu_{1-x}Ga_xO₃ series which is in agreement with dilution of magnetic lattice with Ga substitution and has shown in the inset of figure 5.6(b).

Further, the Rhodes-Wohlfarth ratio has been used to understand the itinerant character of magnetism in present series. This ratio is to calculate q_c/q_s [33]. The q_c characterizes the number of carriers per magnetic atom and is derived from the effective magnetic moment in paramagnetic state, $\mu_{\text{eff}} = g \sqrt{S(S+1)}$ in which $S = q_c/2$, g is the Lande factor and q_s represents μ_H which is the saturated ferromagnetic moment per magnetic atom. It is argued that for $q_c/q_s > 1$, the nature of magnetic interaction would be of itinerant type and the $q_c/q_s \sim 1$ condition implies localized nature of magnetic state in a material. For SrRuO₃, we obtain $q_c = 1.82$ and $q_s = 1.25$, therefore the q_c/q_s ratio becomes 1.46 which favors itinerant magnetic nature. Table 5.2 shows the q_c/q_s ratio increases with Ga doping which again implies that the itinerant ferromagnetic character increases with progressive doping of Ga.

5.3.7 Electrical Resistivity study

Figure 5.7 (a) shows the temperature dependent electrical resistivity $\rho(T)$ of SrRu_{1-x}Ga_xO₃ series with $x = 0.0, 0.05, 0.1$ and 0.2 , the data have been shown in semi-log scale. The SrRuO₃ shows metallic behavior with very low resistance value in whole temperature range [34]. The figure 5.7(a) shows a kink in $\rho(T)$ around the magnetic transition temperature T_c . Below T_c , $\rho(T)$ decreases with a faster rate due to reduced spin disorder effect where above T_c , the $\rho(T)$ increases linearly with variation of temperature. The Ga doping in present series induces insulating nature for $x = 0.1$ material while the $\rho(T)$

increases further for $x = 0.2$ in $\text{SrRu}_{1-x}\text{Ga}_x\text{O}_3$ series. This indicates metal to insulator transition (MIT) takes place for x between 0.05 and 0.1.

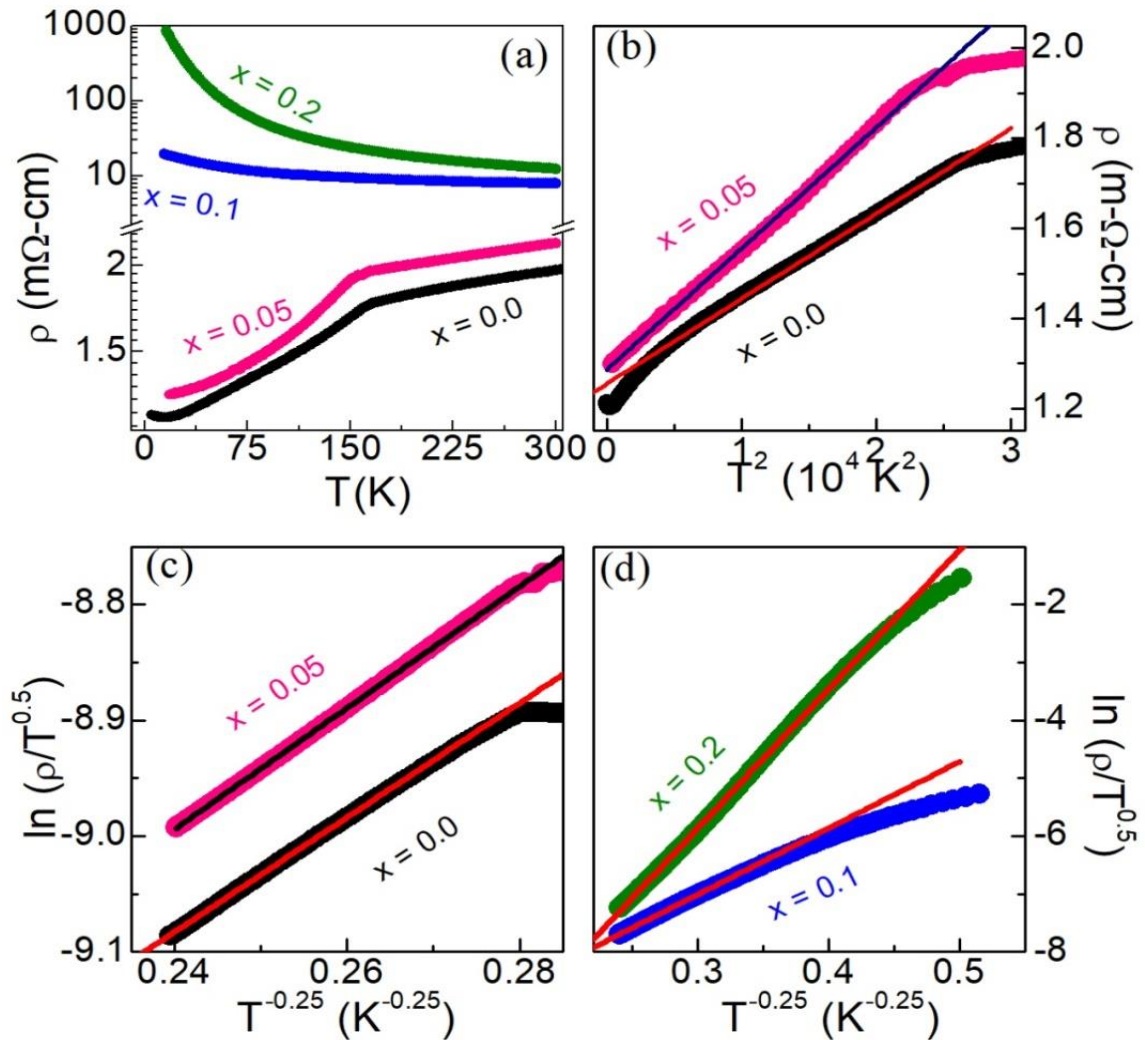


Figure 5.7 (a) The temperature dependent variation in electrical resistivity $\rho(T)$ as function of temperature from temperature range of 5 K to 300 K in logarithmic form of $\text{SrRu}_{1-x}\text{Ga}_x\text{O}_3$ series with $x = 0.0, 0.05, 0.1$ and 0.2 . (b) The linear fitting in FL form in the FM region just below T_c for $x = 0.0$ and $x = 0.05$ of $\text{SrRu}_{1-x}\text{Ga}_x\text{O}_3$ series. (c) The $\rho(T)$ fitting in the high temperature range in the form of Mott-variable range hopping (VRH) of $\text{SrRu}_{1-x}\text{Ga}_x\text{O}_3$ series with $x = 0.0, 0.05$ (d) with $x = 0.1$ and 0.2 .

Here, it can be mentioned that similar insulating behavior has also been observed with Ti^{4+} substitution in $\text{SrRu}_{1-x}\text{Ti}_x\text{O}_3$ series where $\rho(T)$ increases and shows MIT around $x = 0.4$ [35]. This shows Ga^{3+} has stronger influence on the electron transport behavior in

SrRuO₃ inducing insulating behavior at lower concentration of doping. In SrRu_{1-x}Ti_xO₃ and SrRu_{1-x}Ga_xO₃ series, both dopant, Ga³⁺ (0.62 Å) and Ti⁴⁺ (0.605 Å) has similar ionic radii with Ru⁴⁺ (0.62 Å) and they act for site dilution. However, the Ga³⁺ doping generates Ru⁵⁺ along with site dilution. This strong influence Ga³⁺ of electron transport behavior is quite interesting. Plotting of resistivity as a function of T^2 of figure 5.7(b) shows linear fitting.

It is clear in figure that ρ verses T^2 show plotting of resistivity as a function of T^2 , a linear behavior below T_c which extends down to 55 K for SrRuO₃. This suggests a FL type behavior in FM state below T_c in SrRuO₃ which is in agreement with another study [36, 37]. With Ga doping for $x = 0.05$, similar ρ verses T^2 following is observed, however, we find FL behavior is observed in extended temperature range from T_c to 20 K.

Table 5.3 Table shows the values of coefficient of modified Mott VRH behavior of SrRu_{1-x}Ga_xO₃ series.

Quantity/Ti (x)	x = 0.0	x = 0.05	x = 0.1	x = 0.2
ρ_0 (mΩcm K ^{-1/2})	0.037	0.035	0.031	0.003
T_M (K)	466	625	15345	243478

The $\rho(T)$ of SrRuO₃ shows almost linearly increasing behavior with temperature in the PM region. In present series $\rho(T)$ shows both metallic (for low doped sample) as well as insulating (for high doped samples). In insulating state behavior in high temperature PM region decreases with temperature and follows thermally activated charge transport phenomenon. Generally, charge transport mechanism in the insulating region follows the Mott's variable range hopping (VRH) which can be written for the 3D case as [38-41],

$$\rho(T) = \rho_0 \exp \left[\frac{T_M}{T} \right]^{1/4} \quad (5.10)$$

where ρ_0 and T_M are constants. This formula would then be valid for higher doped insulating samples of SrRu_{1-x}Ga_xO₃ series. The Mott formula [eq. (5.10) Greaves have further developed] for materials with the disordered state in which \sqrt{T} term has been included as prefactor and can be written as [42],

$$\rho(T) = \rho_0 \sqrt{T} \exp \left[\frac{T_M}{T} \right]^{1/4} \quad (5.11)$$

The ρ_0 is due to an electron-phonon interaction and has following form of Eq. (5.12)

$$\rho_0 = \frac{1}{3v_{ph} e^2} \left[\frac{8\pi\alpha k_B}{N(E_F)} \right]^{1/2} \quad (5.12)$$

where v_{ph} ($\sim 10^{13} \text{ s}^{-1}$) is an optical phonon frequency, $\alpha = 1/\xi$ is an inverse localization length of the localized states, k_B is the Boltzmann constant, $N(E_F)$ is the DOS and e is the electronic charge. The T_M term of Mott eq. (5.11) measures the degree of disorder present in the system and can be written as

$$T_M = \lambda \left[\frac{\alpha^3}{N(E_F) k_B} \right] \quad (5.13)$$

Where λ is constant and has value 19.4 for disordered state. The present experimental data are fitted with Eq. (5.11) for all the samples of the present series. Figure 5.7(c) and (d) show the fitting of $\rho(T)$ data following Eq. (5.11) for $x = 0.0, 0.05$ and $x = 0.1, 0.2$ respectively in high temperature region. It can be noted that single equation explains the charge conduction mechanism for both metallic and insulating samples. The validity of equation has been previously showing for SrRuO₃. The parameters ρ_0 and T_M estimates from fitting in figures 5.7(c) and 5.7(d) are given in Table 5.3, while ρ_0 does not show large variation with Ga but the T_M , shows a large increase with Ga doping which signifies disorder in system, this probably arises due to introduction of Ga in system which acts for site disorder.

5.3.8 Magnetoresistance study

Figure 5.8 (a) shows temperature dependent resistivity $\rho(T)$ of SrRuO₃, recorded in the presence of 0 T and 8 T magnetic field, which shows metallic behavior throughout the temperature range [43]. However, $\rho(T)$ in the 8 T field is less than $\rho(T)$ in the 0 T field, indicating the presence of magnetoresistance (MR) in SrRuO₃ [43]. MR is defined as the percentage change in $\rho(T)$ in the presence of magnetic field as given by Eq. (5.14)

$$MR\% = \left[\frac{\rho(8T) - \rho(0T)}{\rho(0T)} \right] \times 100 \quad (5.14)$$

where $\rho(8\text{T})$ and $\rho(0\text{T})$ are the resistivities recorded with 8 T and 0 T applied magnetic field respectively.

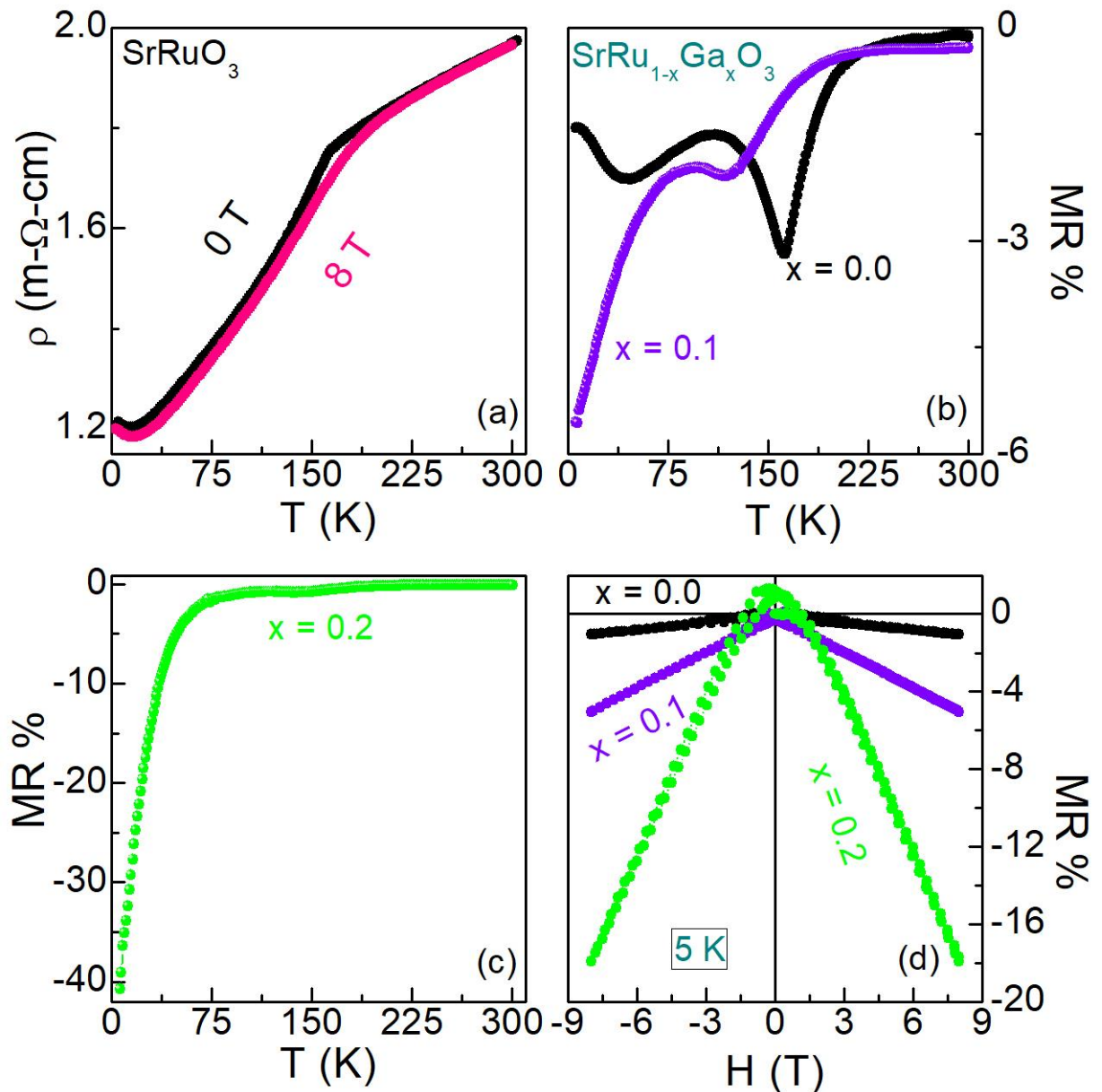


Figure 5.8 (a) The temperature dependent variation in electrical resistivity $\rho(T)$ as function of temperature from temperature range of 5 K to 300 K in zero and 8 T applied magnetic field of SrRuO_3 (b) The MR% as function of temperature range of 5 K to 300 K of $x = 0.0$ and $x = 0.1$ (c) $x = 0.2$ of $\text{SrRu}_{1-x}\text{Ga}_x\text{O}_3$ series. (d) The MR% at 5 K of $\text{SrRu}_{1-x}\text{Ga}_x\text{O}_3$ series with $x = 0.0, 0.1$ and 0.2 .

Figure 5.8(b) shows temperature dependent MR of SrRuO_3 and $\text{SrRu}_{1-x}\text{Ga}_x\text{O}_3$ ($x = 0.1$) calculated from $\rho(T)$ data (as shown in figure 5.8a for SrRuO_3), showing negative MR throughout the temperature range. SrRuO_3 shows minimum MR of -3.2% at T_c and below T_c , MR increases and other minima of -2.1% has been observed at 40 K. However, $\text{SrRu}_{1-x}\text{Ga}_x\text{O}_3$ ($x = 0.1$) shows an increase in MR which is prominent at low temperature. Figure 5.8(c) shows MR of 20% Ga concentration with MR of -40% at 5K, which indicates with increases in Ga doping concentration MR increases. Also, 20% Ga doped sample is insulating throughout the temperature range, and in insulators, the effect of magnetic field on charge carriers is high. Thus magnetic field polarizes electron spin and increases the conductivity.

Further, to observe the MR in the presence of different magnetic field, isothermal magnetization at 5 K has been done with field sweeping ± 8 T for $x = 0.0, 0.1$ and 0.2 of Ga doping concentration as shown in figure 5.8(d), indicating MR throughout the applied field. SrRuO_3 does not show much change in MR, however, with the increase in Ga doping concentration MR increases sharply and becomes 20% at the 8 T field. The temperature dependent and field dependent MR shows conductivity increases in the presence of magnetic field.

5.4 Conclusion

The polycrystalline samples of $\text{SrRu}_{1-x}\text{Ga}_x\text{O}_3$ series with compositions ($x = 0.0, 0.05, 0.1$ and 0.2) have been prepared by the solid-state reaction method. All samples show single phase orthorhombic structure of $Pbnm$ space group. The lattice parameters decrease by Ga substitution due to lower ionic radii of Ru^{5+} which is generated through of Ru^{4+} charge state of by Ga^{3+} doping. Both the dc magnetization decreases and the bifurcation between M_{ZFC} and M_{FC} magnetization decreases with Ga^{3+} substitution. The analysis of thermal demagnetization at low temperature shows coexistence of both itinerant and localized model of magnetization. The magnetic critical exponent (β) of SrRuO_3 close to T_c indicates a mean field type behavior where the value of β increases with Ga substitution. In high temperature region, χ^{-1} follows Curie-Weiss behavior and both the μ_{eff} and θ_p decreases with Ga doping, a GP like behavior is observed at higher doping

concentration. A transition from metallic to insulating state is observed between $x = 0.05$ to 0.1, while the charge transport behavior in high temperature PM region is explained by modified Mott VRH model but in FM state below T_c , the charge transport mechanism mainly follow FL behavior where the temperature range for FL behavior increases with Ga doping.

Bibliography

- [1]. G. Cao, S. McCall, M. Shepard, J. E. Crow, and R. P. Guertin, *Phys. Rev. B*, **56**, 321 (1997).
- [2]. J. M. Longo, P. M. Raccach & J. B. Goodenough, *J. Appl. Phys.* **39**, 1327–1328 (1968).
- [3]. T. Kiyama, K. Yoshimura, K. Kosuge, H. Michor & G. Hilscher, *J. Phys. Soc. Jpn* **67**, 307–311 (1998).
- [4]. K. Yoshimura, T. Imai, T. Kiyama, K. R. Thurber, A. W. Hunt, and K. Kosuge, *Phys. Rev. Lett.* **83**, 4397–4400 (1999).
- [5]. R. Gupta and A. K. Pramanik, *J. Phys.: Condens. Matter*, **29**, 115801 (2017).
- [6]. R. A. Young, A. Sakthivel, T. S. Moss and C. O. Paiva-Santos 1994 *Users Guide to Program DBWS-9411* Georgia Institute of Technology, Atlanta.
- [7]. C. W. Jones, P. D. Battle, P. Lightfoot, and W. T. A. Harrison, *Acta Crystallogr., Sect. C: Cryst. Struct. Commun.* **45**, 365 (1989).
- [8]. T. C. Gibbs, R. Greatrex, N. N. Greenwood, and P. Kaspi, *J. Chem. Soc. Dalton Trans.* 1973, 1250 (1973).
- [9]. L. Klein, J. S. Dodge, C. H. Ahn, J. W. Reiner, L. Mieville, T. H. Geballe, M. R. Beasley, and A. Kapitulnik, *J. Phys.: Condens. Matter* **8**, 10111 (1996).
- [10]. A. Kanbayasi, *J. Phys. Soc. Japan* **41** (1976) 1876.
- [11]. K. Maiti and R. S. Singh, *Phys. Rev. B*, **71**, 161102 (2005).
- [12]. L. Kelin, J.S. Dodge, T.H. Geballe, and A. Kapitulnik, *Appl. Phys. Lett.* **66**, 2427 (1995).
- [13]. A. Callaghan, C. W. Moeller, and R. Ward, *Inorg. Chem.* **5**, 1573 (1966).

- [14]. Cuffini, S.L., Macagno, V.A., Carbonio, R.E., Melo, A. Trollund, E. and Gautier, J.L.. *J Solid State. Chem.*, **105**, 1993, 161-170.
- [15]. C. Kittel, Introduction to Solid State Physics, Wiley, New Delhi (2012).
- [16]. F. Keffer, in: Encyclopedia of Physics, vol. XVIII, ed. H. P. Wign (*Springer, Berlin*, 1966) part 2, p. 1.
- [17]. A. Das and A. K. Majumdar, *Journal of Magnetism and Magnetic Materials*, **128** 47-57 (1993).
- [18]. B. Nadgorny, M. S. Osofsky, D. J. Singh, G. T. Woods, R. J. Soulen Jr., M. K. Lee, S. D. Bu and C. B. Eom, *Appl. Phys. Lett.*, **82**, 427 (2003).
- [19]. P. Raychaudhuri, A. P. Mackenzie, J. W. Reiner and M. R. Beasley, *Phys. Rev. B*, **67**, 020411 (2003).
- [20]. C. Sow, D. Samal, P. S. Anil Kumar, A. K. Bera, and S. M. Yusuf, *Phys. Rev. B*, **85**, 224426 (2012).
- [21]. C. Kittel, Introduction to Solid State Physics, Wiley, New Delhi (2012).
- [22]. A. Perumal and V. Srinivas, K. S. Kim and S. C. Yu, V. V. Rao, R. A. Dunlap, *Phys. Rev. B*, **65**, 064428.
- [23]. H. E. Stanley, Introduction to Phase Transitions and Critical Phenomena, *Oxford University Press* (1971).
- [24]. D. Fuchs, M. Wissinger, J. Schmalian, C. L. Huang, R. Fromknecht, R. Schneider and H. v. Lohneysen, *Phys. Rev. B.*, **89**, 174405 (2014).
- [25]. J.G. Cheng, J.S. Zhou, J. B. Goodenough, and C.-Q. Jin, *Phys. Rev. B*, **85**, 184430 (2012).
- [26]. D. Kim, B. L. Zink, F. Hellman, S. McCall, G. Cao, and J. E. Crow, *Phys. Rev. B*, **67**, 100406 (2003).
- [27]. R. B. Griffiths, *Phys. Rev. Lett.*, **23**, 17 (1969).
- [28]. A. K. Pramanik and A. Banerjee, *Phys. Rev. B*, **81**, 024431 (2010).
- [29]. C. Magen, P. A. Algarabel, L. Morellon, J. P. Araújo, C. Ritter, M. R. Ibarra, A. M. Pereira and J. B. Sousa, *Phys. Rev. Lett.*, **96**, 167201 (2006).
- [30]. A. H. Castro Neto, G. Castilla and B. A. Jones, *Phys. Rev. Lett.*, **81**, 3531 (1998).

- [31]. C. Sow, D. Samal, P. S. Anil Kumar, A. K. Bera, and S. M. Yusuf, *Phys. Rev. B*, **85**, 224426 (2012).
- [32]. A. Arrott, *Phys. Rev.*, **108**, 1394 (1957).
- [33]. P. Rhodes and E. P. Wohlfarth, *Proc. R. Soc. London*, **273**, 247 (1963).
- [34]. P. B. Allen, H. Berger, O. Chauvet, L. Forro, T. Jarlborg, A. Junod, B. Revaz, G. Santi, *Phys. Rev. B*, **53**, 4393 (1996).
- [35]. K. W. Kim, J. S. Lee, T. W. Noh, S. R. Lee and K. Char, *Phys. Rev. B*, **71**, 125104 (2005).
- [36]. P. Kostic, Y. Okada, N. C. Collins, Z. Schlesinger, J. W. Reiner, L. Klein, A. Kapitulnik, T. H. Geballe, and M. R. Beasley, *Phys. Rev. Lett.*, **81**, 2498 (1998).
- [37]. M. S. Laad and E. Müller-Hartmann, *Phys. Rev. Lett.*, **87**, 246402 (2001).
- [38]. N. F. Mott, *Proc. Phys. Soc. London Sect. A* **62**, 416 (1949).
- [39]. N. F. Mott, *Metal-Insulator Transitions* (Taylor and Francis, London, 1990).
- [40]. N. F. Mott and E. A. Davis, *Electronic Processes in Non-Crystalline Materials* (Oxford University Press, Oxford, 1979).
- [41]. N. F. Mott, *Philos. Mag.* **19**, 835 (1969).
- [42]. G. N. Greaves, *J. Non-Cryst. Solids* **11**, 427 (1973).
- [43]. C. Sow, D. Samal, and P. S. Anil Kumar, *J. Appl. Phys.*, **111**, 07E121 (2012).

Chapter 6

Site dilution effect on Electrical Transport Behavior in $\text{SrRu}_{1-x}\text{Ti}_x\text{O}_3$

In this chapter, we discuss transport behavior study in terms of electrical resistivity (presence of zero field and in field) and specific heat study of $\text{SrRu}_{1-x}\text{Ti}_x\text{O}_3$ series ($x \leq 0.7$). The Ti^{4+} substitution has changed the electron correlation effect and as we have already discussed the significant change of electron correlation (U) and density of states (DOS) which effect also present in transport behavior in increasing and decreasing order respectively. The transport behavior has studied in terms of Fermi liquid, non-Fermi liquid, Kondo and modified Mott variable range hopping (VRH) in absence and presence of magnetic field. The specific heat (C_p) study also shows strong correlation effect at low temperature.

6.1 Introduction

It has been observed that SrRuO_3 exhibits metallic behavior with temperature as well as range of 1000 K [1]. However, the $\rho(T)$ has direct correlation with magnetic properties in this material for instance in paramagnetic (PM) high temperature region without any spin correlation, the $\rho(T)$ shows almost linear behavior with temperature as high as 1000 K. However, in low temperature ferromagnetic (FM) state below ~ 160 K, $\rho(T)$ shows a change in slope across T_c and its value decreases with faster rate with decreasing

temperature. This clearly implies that a FM type spin correlation influences the electronic transport mechanism. The magnetic nature in SrRuO₃ is mostly believed to be of itinerant type [2-8]. However, recently a coexistence of both itinerant and localized model of magnetism has been shown to be present in this material [9]. In SrRu_{1-x}Ti_xO₃ series, we use nonmagnetic Ti⁺⁴ (3d⁰) substitution method which has been doped to dilute the magnetic Ru-O-Ru channel and also to tune the electronic properties through changing the electron number and electron correlation. By following Ti⁺⁴, one can expect an increase in U and decrease of electrons of the SrRuO₃ system by 3d⁰ non-magnetic character. The change in U and $N(\epsilon_F)$ will affect the magnetic nature of itinerant FM. The photo emission spectroscopy (PES) study of SrRuO₃ shows that the existence of coherent (itinerant) peak with the presence of incoherent (localized) peak at Fermi level (E_F), which shows that U cannot be ignored in the present system. The same study (PES) by Ti substitution shows that the ratio of incoherent to coherent peak increases at E_F while the density of states (DOS) decreases [10, 11]. The band structure study shows that the U increases by Ti doping in SrRu_{1-x}Ti_xO₃ series [12]. On the other way, by following the localized model the dilution will effect on Ru-O-Ru bond so by this transition temperature (T_c) should modify.

The motivation of present chapter in the thesis is to understand the evolution of transport behavior by Ti substitution. Further, to understand the behavior of charge transport in the presence of magnetic field, the $\rho(T)$ has been measured in the presence of magnetic field both in the presence of temperature as well as various selected temperatures. The charge transfer mechanism in SrRuO₃ has been investigated in detail in different magnetic regions in terms of modified Mott variable range hopping (VRH), Fermi liquid, non-Fermi liquid (NFL) and Kondo behavior and the influence of Ti substitution on these phenomena have been studied in present SrRu_{1-x}Ti_xO₃ series. We have further use specific heat $C_p(T)$ measurement to understand the thermodynamic behavior in this material as well as establish a correlation with the electronic transport behavior.

6.2 Experimental Details

The doped and undoped polycrystalline samples of SrRu_{1-x}Ti_xO₃ series with $x = 0.0, 0.1, 0.2, 0.3, 0.4, 0.5$ and 0.7 have been prepared by using solid-state reaction method and details of samples preparation have been discussed elsewhere [13]. The dc electrical resistivity $\rho(T)$ and magnetoresistance (MR) data were measured by the home-built setup of Oxford superconducting magnet using the four probe technique, in the temperature range 5 K to 300 K and at 80 kOe applied magnetic field. The specific heat $C_p(T)$ measurement has been measured by semi adiabatic method.

6.3 Results and Discussions

6.3.1 Electrical Resistivity Study

Figure 6.1 shows temperature dependent electrical resistivity $\rho(T)$ data (right axis) and magnetization $M(T)$ data in the temperature range 5 K to 300 K (left axis) are measured as field cool (FC) and zero field cool (ZFC) protocol in the presence of 100 Oe magnetic fields. The $M(T)$ shows ferromagnetic (FM) to paramagnetic (PM) second-order phase transition at transition temperature ($T_c \sim 163$ K) indicates by arrow and also vertical dotted line (chapter 3). The right axis of Figure 6.1 shows temperature dependent electrical resistivity $\rho(T)$ of SrRuO₃ in zero magnetic field and in the presence of 8 T of the magnetic field. The $\rho(T)$ of SrRuO₃ shows metallic behavior throughout the temperature range [1]. Interestingly, the $\rho(T)$ shows slope change around T_c which implies a close correlation between magnetism and transport behavior in SrRuO₃. Above T_c in PM region, the $\rho(T)$ increases linearly and does not show saturation even reaching the Ioffe-Regel limit, which is an indication of bad metallic nature. Below T_c in FM region, the $\rho(T)$ decreases sharply which is to attribute spin disorder effect. Further, a minima in $\rho(T)$ (indicate by circle region) has been observed around 15 K (T_K), where $\rho(T)$ increases as the temperature is lowered indicating a Kondo like behavior (will discuss later). The $\rho(T)$ does not show any major change in magnitude from 5 K (1.21 mΩ-cm) to 300 K (1.97 mΩ-cm) at zero magnetic field. By applying 8T of the magnetic field, $\rho(T)$ of SrRuO₃ decreases and the kink around T_c is suppressed (shown in Figure 6.1). The

magnetoresistance (MR) has been calculated from zero field and high field $\rho(T)$ curve using following relation $MR = \frac{\rho(8T) - \rho(0T)}{\rho(0T)}$. The inset of Figure 6.1 shows negative MR dip around T_c and at low temperature (detail will discuss later).

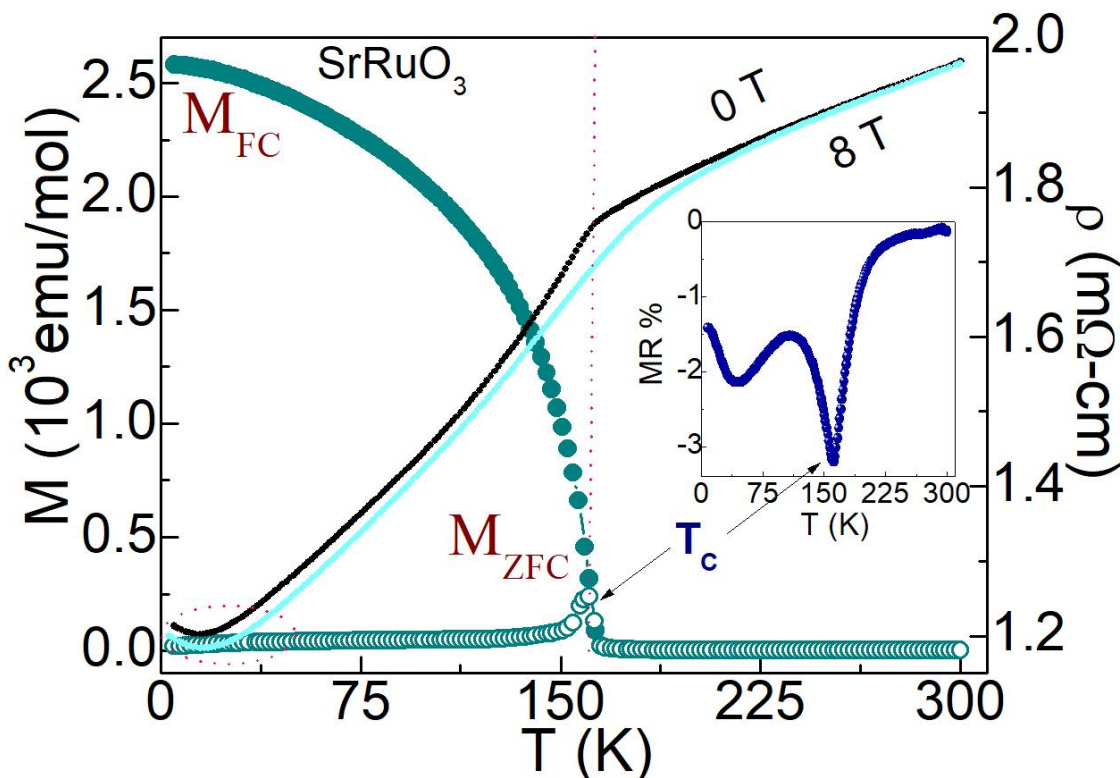


Figure 6.1 The left axis shows temperature dependent dc magnetization of SrRuO₃ in the form of ZFC and FC from 5 K to 300 K and the right axis shows temperature dependent electrical resistivity $\rho(T)$ from 5 K to 300 K at 0 T and 8 T of the magnetic field and the inset shows magnetoresistance (MR) of SrRuO₃ from 5 K to 300 K.

The $\rho(T)$ data of SrRu_{1-x}Ti_xO₃ series with $x = 0.0, 0.1, 0.2, 0.3, 0.4$ and $x = 0.5, 0.7$ are shown in Figure 6.2 (a) and Figure 6.2 (b) respectively. It is clear from Figure 6.2 (a) that with an increase in the percentage of Ti doping in SrRu_{1-x}Ti_xO₃ series, the $\rho(T)$ increases and near about identical behavior of SrRuO₃ is observed till $x \sim 0.4$. The materials till $x \sim 0.3$ show a metallic behavior. However, figure 6.2 (a) show temperature driven metal to insulator transition (MIT) is observed around ~ 74 K (T_{MIT}) for $x = 0.4$ sample. The insulating behavior of SrRu_{1-x}Ti_xO₃ series increases as the Ti doping

percentage increases for $x = 0.5$ and 0.7 , as shown in Figure 6.2. It may be noted that for higher doped samples the increases magnitude of resistivity probably arises due to the less number of Ru–O–Ru type conducting paths in SrRu_{1-x}Ti_xO₃ series as Ti⁴⁺ acts Ru site dilution. The magnitude of ρ (T) at low temperature (5K) of SrRuO₃ and SrRu_{1-x}Ti_xO₃ ($x = 0.7$) is 1.21 m Ω -cm and 62.88 m Ω -cm, respectively indicating a substantial change towards the insulating behavior. The ρ (T) does not saturate at high temperature for metallic samples ($x = 0.0, 0.1, 0.2, 0.3$ and 0.4) and the derivative $d\rho/dT$ (not shown here) remains finite down to the lowest temperatures. The ground state of $\rho(T)$ switches from metallic FM with insulating FM with Ti doping which is because of the collective effect of hole doping, the electron correlation effect and the disorder effect.

The residual resistivity ratios ($\text{RRR} = \rho(300 \text{ K})/\rho(5 \text{ K})$) for SrRuO₃ is ~ 1.62 which decreases with Ti doping to 0.2769 for $x = 0.7$ in zero field. Such low value of RRR is typically observed in doped Mott insulators close to a metal-insulator transition which exhibit a correlated metal type behavior.

Here we attempt to bring out the exact functional dependence of ρ (T) in different temperature ranges to identify the dominant factors responsible for transport mechanism in the specified temperature ranges. In order to study the magnetic contribution, the field dependent $\rho(T)$ has been studied in detail as a function of temperature as well as composition.

Table 6.1 The table presents the values of ρ_{0M} and T_M by the variation of Ti doping.

Quantity	Field	x = 0.0	x = 0.1	x = 0.2	x = 0.3	x = 0.4	x = 0.5	x = 0.7
ρ_{0M} (m Ω -cm K ^{-1/2})	0 T	0.037	0.071	0.052	0.097	0.076	0.063	0.070
	8 T	0.038	0.077	0.053	0.106	0.086	0.064	0.074
T_M (K)	0 T	466	122	583	145	646	12642	14561
	8 T	439	078	552	093	426	12458	13449

6.3.2 Electrical Transport in PM State

In this section, we discuss about the charge transport mechanism in high temperature paramagnetic (PM) state for SrRu_{1-x}Ti_xO₃ series. Figure 6.2 (a) shows $\rho(T)$ in PM state continuously increases almost linearly up to room temperature till $x = 0.4$. On the other hand, figure 6.2 (b) shows $\rho(T)$ continuous decrease till room temperature showing an insulating behavior [14]. In insulator usually electronic transport occur to thermally activated hopping of charge carriers. In most case charge conduction follow Mott VRH model which consider hopping of charge carriers in disorder metal, this Mott VRH has been further modified by Greaves to include high temperature disorder state [15-18]. According to Greaves, the modified Mott VRH was given by [19]

$$\rho(T) = \rho_o \sqrt{T} \exp \left[\left(\frac{T_M}{T} \right)^{1/4} \right] \quad (6.1)$$

Where ρ_o is the pre-exponential constant and due to the electron-phonon interaction and T_M is the characteristic Mott temperature coefficient and depends on the density of state (DOS) at the Fermi level (E_F).

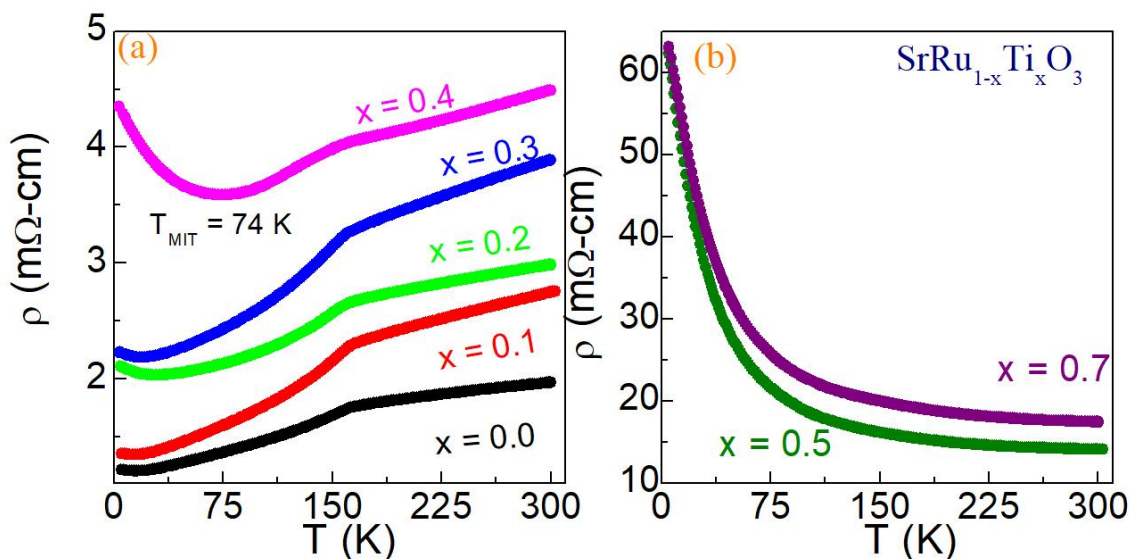


Figure 6.2 (a) The temperature dependent resistivity $\rho(T)$ of SrRu_{1-x}Ti_xO₃ series with $x = 0.0, 0.1, 0.2, 0.3$ and 0.4 from 5 K to 300 K (b) The temperature dependent resistivity of SrRu_{1-x}Ti_xO₃ series with $x = 0.5$ and 0.7 from 5 K to 300 K.

The T_M measures the degree of disorder and the relation of ρ_0 and T_M at Fermi level has given below in equation (6.2 and 6.3),

$$\rho_{0M} = \frac{1}{3v_{ph}} \left[\frac{8\pi\alpha k_B}{N(E_F)} \right]^{1/2} \quad (6.2)$$

and

$$T_M = \frac{19.4 \alpha^3}{N(E_F) k_B} \quad (6.3)$$

Where v_{ph} is the optical phonon frequency, k_B is the Boltzmann constant, e is the electronic charge and ($\alpha = 1/\xi$) is the inverse localization length of the localized states, and ξ is the localization length. The $\rho(T)$ data in high temperature regime have fitted with equation (6.1) in figure 6.3 and the obtained fitting parameters such as ρ_0 and T_M have been given in Table 6.1 for present series. The equation fitted above T_c have samples with $x < 0.4$ while the equation can be following in whole temperature range for $x = 0.5$ and 0.7.

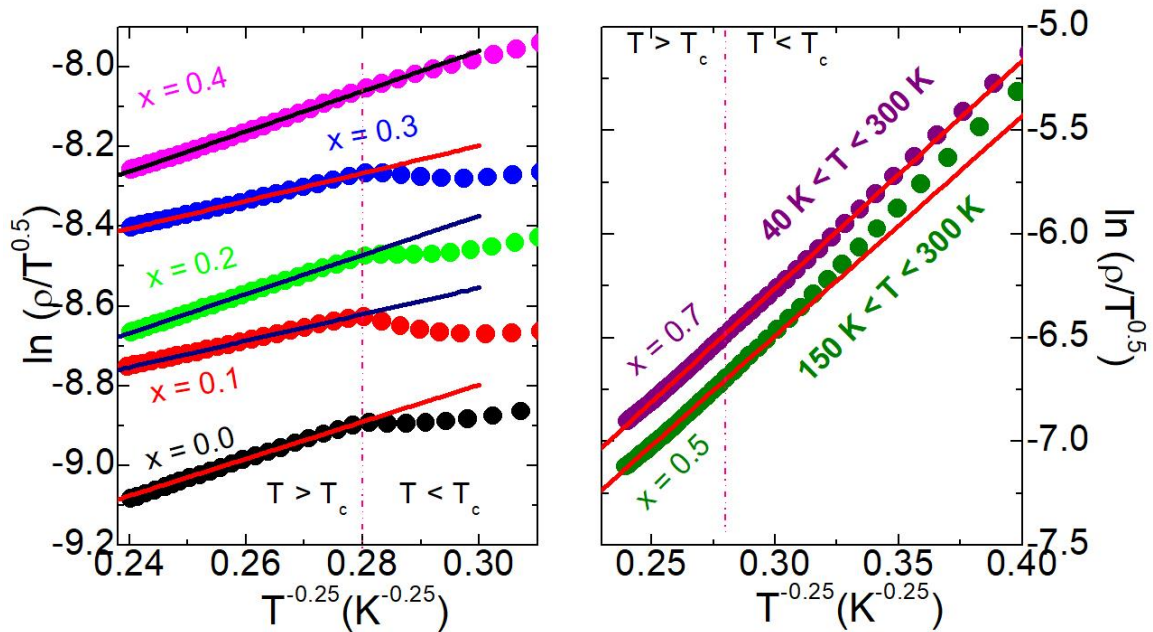


Figure 6.3 The modified form of Mott VRH fitting of resistivity $\rho(T)$ in the high temperature range of SrRu_{1-x}Ti_xO₃ series with compositions of (a) $x = 0.0, 0.1, 0.2, 0.3$ and 0.4 (b) 0.5 and 0.7 .

6.3.3 Electrical Transport in FM state

Previously we have seen that electronic transport behavior in low temperature ferromagnetic (FM) state below T_c for parent compound SrRuO_3 follows metallic behavior, however, we observed $\rho(T)$ exhibits change in slope below T_c , compared to that in high temperature paramagnetic (PM) state. This clearly implies that magnetic ordering has a profound influence on the charge conduction mechanism through electron scattering. The earlier reports have shown charge conduction in SrRuO_3 at low temperature follow Fermi liquid (FL) behavior with functional form [20, 21],

$$\rho(T) = \rho_0 + A_{FL}T^2 \quad (6.4)$$

Here ρ_0 is the residual resistivity due to impurity scattering and A_{FL} is the FL coefficient. The fermi liquid behavior for electron transport has been proposed by Landau which considers a dominant electron- electron interactions which effectively gives different temperature dependence of resistivity compared to simple metal.

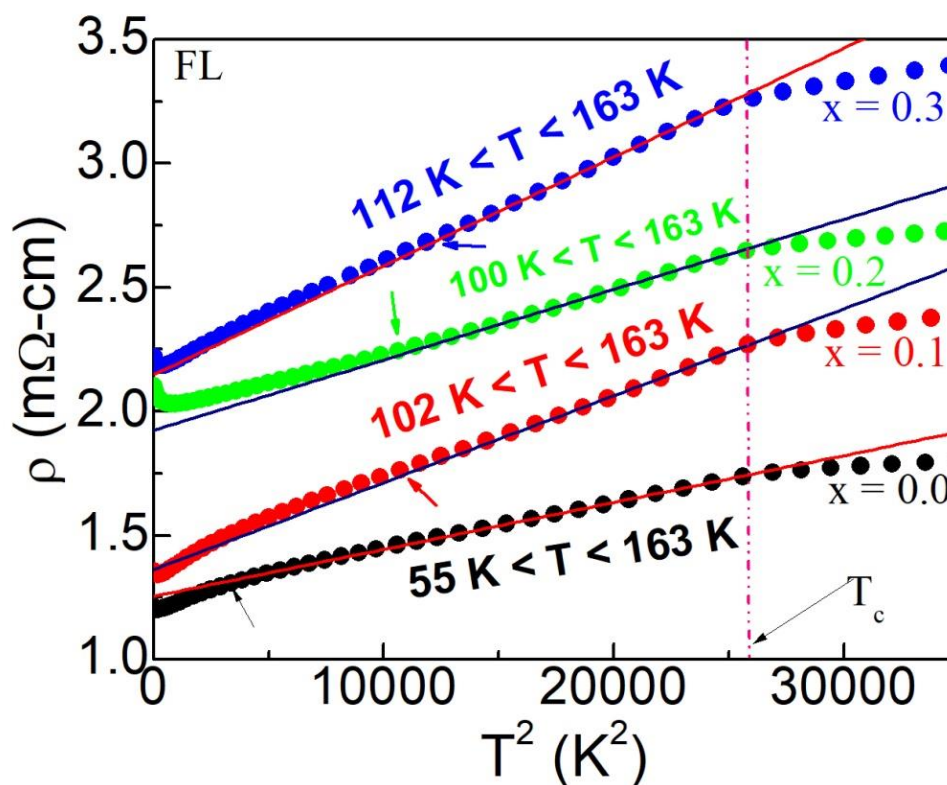


Figure 6.4 The Fermi liquid (FL) behavior fitting of $\text{SrRu}_{1-x}\text{Ti}_x\text{O}_3$ series of $x = 0.0, 0.1, 0.2,$ and 0.3 with different temperature range below T_c .

It is interesting to note that in the isoelectronic doped system, i.e., $\text{Sr}_{1-x}\text{Ca}_x\text{RuO}_3$, where the calcium substitution causes suppression of ferromagnetism in SrRuO_3 showing a quantum phase transition around $x \sim 0.7$ [22, 23]. In this series ($\text{Sr}_{1-x}\text{Ca}_x\text{RuO}_3$) the Fermi liquid type behavior has only been observed in ferromagnetic region and composition ($x \leq 0.7$), and the system exhibits a different non-Fermi liquid type behavior for non-ferromagnetic compositions towards CaRuO_3 . This clearly shows Fermi-liquid behavior in SrRuO_3 is deeply connected with the magnetism in this material. Following this, we have plotted the resistivity as a function of T^2 which have been shown in figure 6.4. The figure 6.4 clearly shows that the resistivity of SrRuO_3 follows a quadric dependence on temperature below T_c , however, we observed that T^2 dependence deviates at low temperature which is marked by vertical arrow in figure 6.4. For the doped material in $\text{SrRu}_{1-x}\text{Ti}_x\text{O}_3$ series, we also observed similar quadric dependence of temperature, however, range of Fermi liquid behavior modifies with Ti substitution. The temperature ranges for the validity of the Fermi liquid behavior (equation 6.4) along with the value of ρ_0 and FL coefficient have been shown in table 6.2 for present $\text{SrRu}_{1-x}\text{Ti}_x\text{O}_3$ series. Table 6.2 clearly shows the range of FL behavior of SrRuO_3 observes till 55 K and below which deviation occurs. This behavior also follows of all metallic samples $x < 0.4$ which shows FL range decreases by Ti substitution without change towards T_c . Given that the electron correlation is the origin for the Fermi liquid behavior and the Ti substitution in present SrRuO_3 , which modifies the electron correlation (U) as well as the electron density with this $3d^0$ character, will have a significant influence on electron transport behavior hence on the Fermi liquid behavior.

Here we mention that in previous studies the Fermi liquid behavior has been observed in low temperature region [24], however, in the present study we observed the Fermi liquid behavior at high temperature close to T_c for all the samples. The breakdown of the Fermi liquid behavior for this series in low temperature remains surprising. To understand the transport in low temperature we have tried to plot the resistivity within the prescription of non-Fermi liquid behavior which naturally arises in the breakdown of Fermi liquid behavior with following temperature dependence.

$$\rho(T) = \rho_0 + B_{\text{NFL}}T^{3/2} \quad (6.5)$$

Here ρ_0 is the temperature independent value of residual resistivity from the electron-impurity scattering caused by defects and B_{NFL} is the NFL coefficient. The appearance of non-Fermi liquid behavior in case of breakdown of Fermi liquid behavior is usually understood due to quantum phase transition, 1D transport, etc.

The switching of Fermi liquid to non-Fermi liquid with doping in $\text{Sr}_{1-x}\text{Ca}_x\text{RuO}_3$ series is clear evidence of a quantum phase transition across $x = 0.7$. The NFL behavior has been previously reported in SrRuO_3 through optical conductivity/reflectivity measurement by Kostic et al. [20], which has been further theoretically explained by Laad et al. [21], considering a nearly cubic structure where the peculiar orientation of t_{2g} orbitals gives the peculiar structure of hybridization which essentially results in non-Fermi Liquid behavior. Figure 6.5 present plotting of $\rho(T)$ vs. $T^{3/2}$ which shows a linear dependence at low temperature region below after the temperature where the Fermi liquid behavior breaks down.

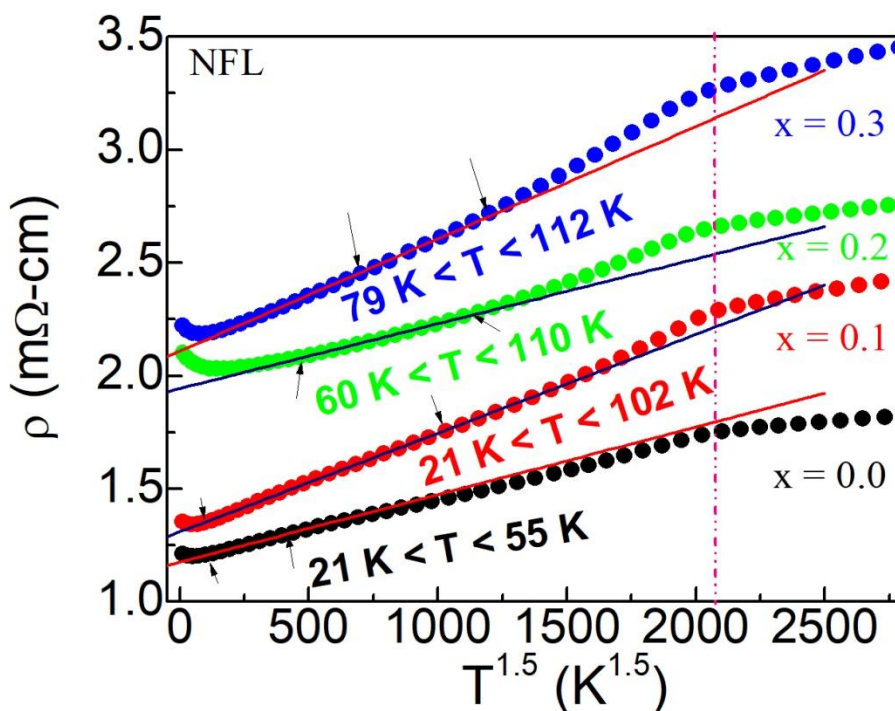


Figure 6.5 The non-Fermi liquid (NFL) fitting of $\text{SrRu}_{1-x}\text{Ti}_x\text{O}_3$ series of $x = 0.0, 0.1, 0.2,$ and 0.3 with different temperature range below T_c .

For parent SrRuO₃, we observed non Fermi liquid (NFL) behavior is followed down to temperature around 21 K, however, lower range for validity of non-Fermi liquid increases towards high temperature for instance, for $x = 0.4$ sample we observed that non Fermi liquid behavior is down to only 100 K (table 6.2). Similarly, we have noted the temperature range as well as the coefficients ρ_0 and B_{NFL} , in table 6.2 for the whole series. However, by applying 8 T of magnetic field, FL behavior changes in NFL behavior without changing NFL behavior.

The observation of Fermi liquid and non-Fermi liquid behavior and their variation with temperature and composition in the present series is quite noteworthy. With the present data set, it is difficult to understand this evolution in electronic transport behavior and may be theoretical investigations need to be involved for this purpose. Nonetheless, based on other experimental results we speculate that the change in electron correlation and site network through Ti substitution would likely cause this effect.

Table 6.2 This presents the values of FL, NFL and Kondo coefficients and temperature range by the variation of Ti doping.

Field	Property	Quantity	x = 0.0	x = 0.1	x = 0.2	x = 0.3	x = 0.4
0 T	FL	ρ_0 (m Ω cm)	1.25	1.36	1.92	2.15	3.61
		A_{FL} (m Ω cm K ²) $\times 10^{-5}$	1.89	3.50	2.83	4.38	1.66
		Range (K)	55 < T < 163	102 < T < 163	110 < T < 163	112 < T < 163	133 < T < 163
0 T	NFL	ρ_0 (m Ω cm)	1.18	1.31	1.94	2.11	3.20
		B_{NFL} (m Ω cm K ²) $\times 10^{-4}$	2.98	4.36	2.86	4.96	4.40
		Range (K)	21 <	21 < T < 102	60 < T < 110	79 < T < 112	100 <

			T<55				T<133
8 T	NFL	ρ_0 (mΩ cm)	1.17	1.25	1.84	1.96	3.20
		B_{NFL} (mΩ cm K ²) × 10 ⁻⁴	2.53	4.43	3.50	5.70	4.40
		Range (K)	58< T<163	68< T<163	95< T<163	97< T<163	134< T<163
8 T	NFL	ρ_0 (mΩ cm)	1.15	1.24	1.90	2.01	3.15
		B_{NFL} (mΩ cm K ²) × 10 ⁻⁴	2.97	4.66	2.92	5.20	4.02
		Range (K)	27< T<58	33< T<68	60< T<95	61< T<97	111< T<134
0 T	Kondo	ρ_0 (mΩcm)	1.23	1.38	2.17	2.27	
		A_{Kondo} (mΩ cm) × 10 ⁻²	1.19	1.52	3.93	2.96	
8 T	Kondo	ρ_0 (mΩ cm)	1.21	1.34	2.12	2.20	
		A_{Kondo} (mΩ cm) × 10 ⁻²	1.12	1.50	3.56	2.83	

6.3.4 Kondo Behavior

The resistivity data in figure 6.1 for SrRuO₃ shows a small upturn in ρ (T) at low temperature below $T_K \sim 20$ K. Usually, this upturn in ρ (T) where resistivity increases with decreasing temperature at low temperature is considered as Kondo like behavior.

The Kondo effect arises due to scattering of conduction electrons with magnetic impurities resulting in continuous increase in resistivity at low temperature. In case of Kondo behavior resistivity follows logarithmic of temperature dependence with following functional form

$$\rho(T) = \rho_0 - C \ln T \quad (6.6)$$

where ρ_0 is the Kondo residual resistivity (i.e., sample impurity) and C is the Kondo coefficient. Following equation (6.6), we have plotted this Kondo behavior as shown in figure 6.6 and it has been observed that the samples show Kondo behavior till Ti doping concentration $x = 0.3$. As we increase the Ti doping level ($x \geq 0.3$), $\rho(T)$ shows insulating behavior and Kondo effect disappears.

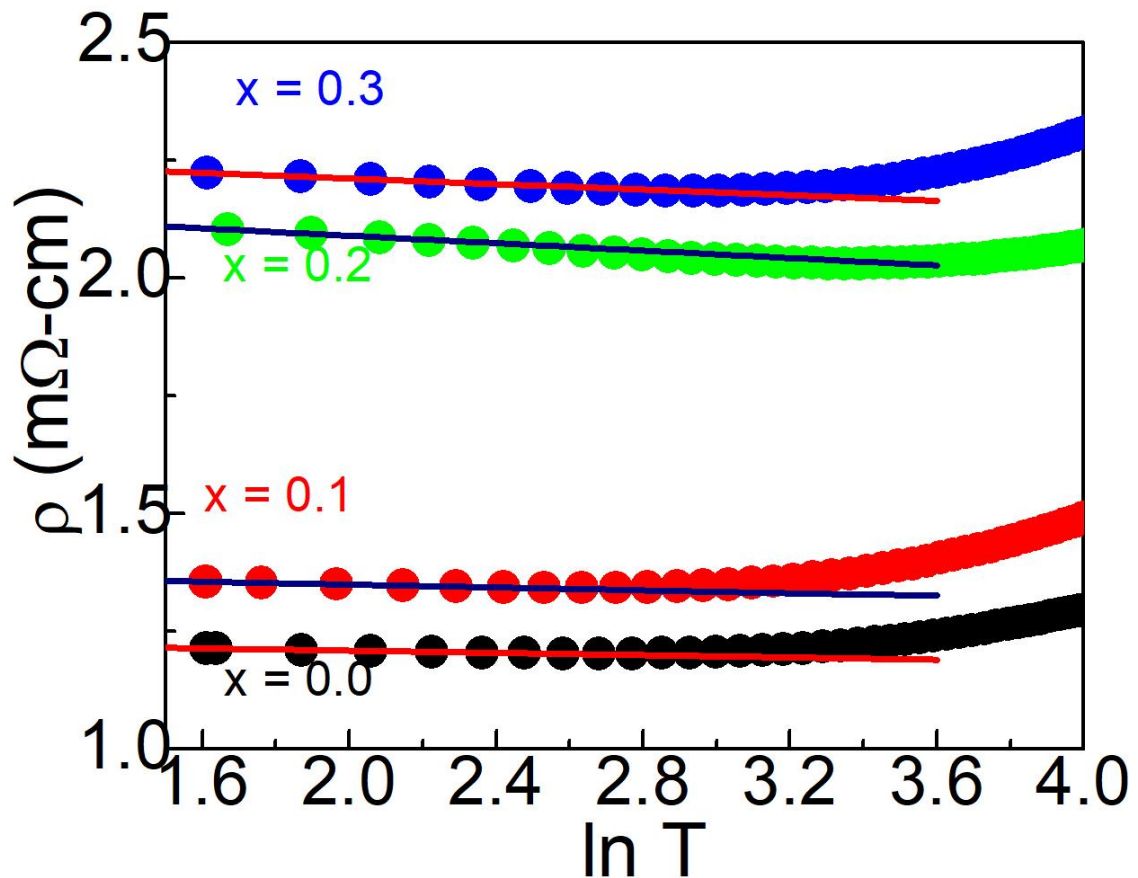


Figure 6.6 The Kondo effect fitting $\rho(T)$ with logarithmic temperature of $\text{SrRu}_{1-x}\text{Ti}_x\text{O}_3$ series with $x = 0.0, 0.1, 0.2,$ and 0.3 from 5 K to 21 K.

6.3.5 Magnetoresistance (MR)

In order to study the magnetic contribution, temperature dependent magnetoresistance (MR) has been evaluated from figure 6.1, for SrRuO_3 , as shown in the inset of figure 6.1, by following the equation (6.7)

$$MR\% = \frac{\Delta\rho}{\rho(0)} \times 100 = \left[\frac{\rho(8T) - \rho(0T)}{\rho(0T)} \right] \times 100 \quad (6.7)$$

where $\rho(8T)$ is the resistivity recorded in the presence of 8 T of magnetic field and $\rho(0)$ is the resistivity recorded in zero magnetic field.

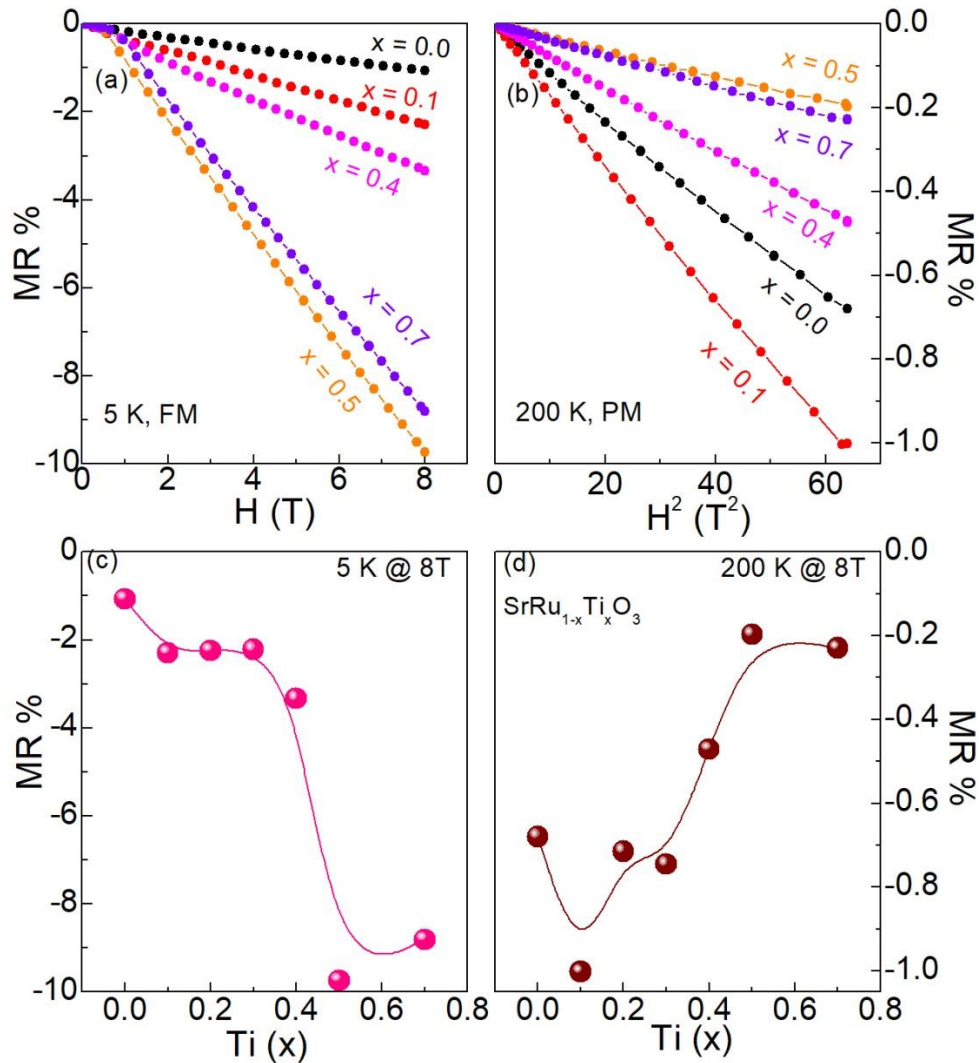


Figure 6.7 (a) The MR at 5 K with variation of H and (b) shows MR at 200 K with variation of H^2 of composition of $\text{SrRu}_{1-x}\text{Ti}_x\text{O}_3$ series ($x = 0.0, 0.1, 0.4, 0.5$ and 0.7) (c) shows MR at 8T of field with variation of composition of $\text{SrRu}_{1-x}\text{Ti}_x\text{O}_3$ series at 5 K and (d) 200 K.

Negative MR has been observed throughout the temperature range and maximum change in MR of 3.2% has been observed at temperature marked as T_c , below which MR

increases and another minima has been observed around 40 K [25] as shown in inset of Figure 6.1. Further, we have plotted the isothermal magnetoresistance, in the field range 0 – 8 T at two different temperatures i.e., 5 K and 200 K, which represent Ferromagnetic (FM) and Paramagnetic (PM) regions, respectively for the $\text{SrRu}_{1-x}\text{Ti}_x\text{O}_3$ series. The MR data are shown in Figures 6.7(a) and 6.7(b).

A negative magnetoresistance at both the temperatures (5 K and 200 K) have been observed where the MR varies linearly with the applied magnetic field in ferromagnetic regime at 5 K. However, in high temperature paramagnetic region at 200 K, MR varies quadratically with the applied magnetic field. Figure 6.8 found to be maximum for $x = 0.5$ at 5K, of the order of 9%. Figure 6.7(c) shows the MR observed at 8 T magnetic field, for different Ti concentration in ferromagnetic region at 5 K. The MR value increases non-monotonically with an increase in Ti doping, till $x = 0.4$, above which a sharp increase in MR has been observed. Interestingly, MR does not change much for Ti doping concentration $x = 0.2$ to 0.4, and a flat region in observed in figure 6.7 (c), which is related to metal to insulator transition. Figure 6.7 (d) shows MR ratio at 8 T magnetic field for different Ti doping concentration at 200 K in the paramagnetic region, as evaluated from figure 6.7 (b). It is evident from the data that in PM region MR does not have a significant change in magnitude as compared to FM regime. In PM, maximum MR of 1% is observed for $x = 0.1$ and MR value decreases with increase in Ti doping concentration to 0.2 % for $x = 0.7$.

Further to study the variation of magnetoresistance (MR) with positive and negative field sweeping, the MR has been recorded for $\text{SrRu}_{1-x}\text{Ti}_x\text{O}_3$ series, with magnetic field sweeping of $\pm 8\text{T}$ at 5 K for the whole series of samples. The MR data are shown in Figure 6.8 (a)–(f). Interestingly, we can notice that MR is negative and a hysteresis which has been observed for all the samples with field sweeping from 0 T to +8 T to 0 T and to -8 T to 0 T and 8 T (indicated by arrow). In this whole cycle, we observed that the variation in positive MR, remanent MR, coercive field and hysteresis for all the samples of the series. The coercive field and positive MR is symmetric for both positive and negative field which indicates hysteresis in MR. The opening of hysteresis decreases with

Ti concentration and for $x = 0.5$ very small hysteresis is obtained. However, with further increasing the doping concentration, the opening of hysteresis increases for $x = 0.7$ as shown in figure 6.8 (f).

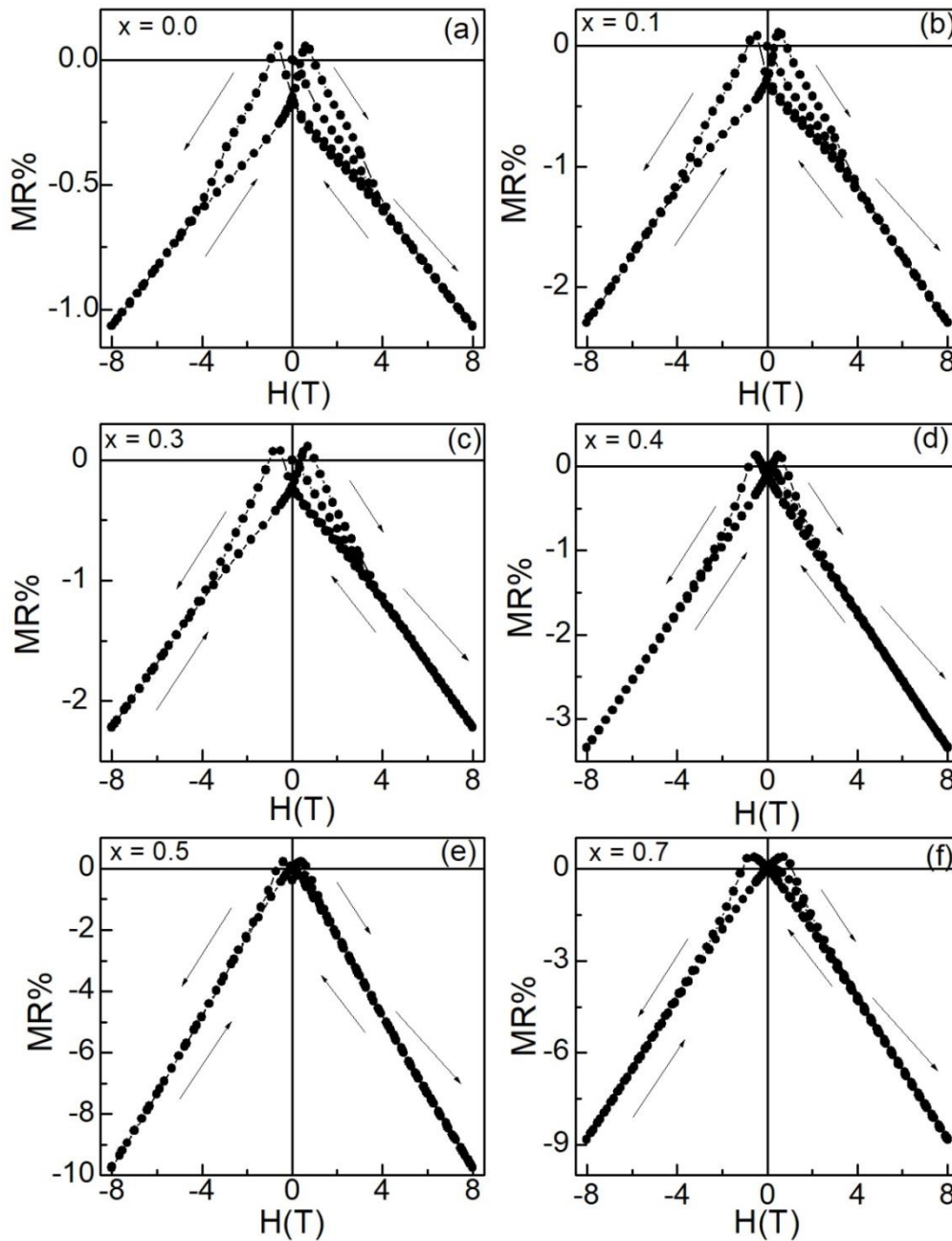


Figure 6.8 The MR at 5 K of $\text{SrRu}_{1-x}\text{Ti}_x\text{O}_3$ series with (a) $x = 0.0$, (b) $x = 0.1$, (c) $x = 0.3$, (d) $x = 0.4$, (e) $x = 0.5$ and (f) $x = 0.7$.

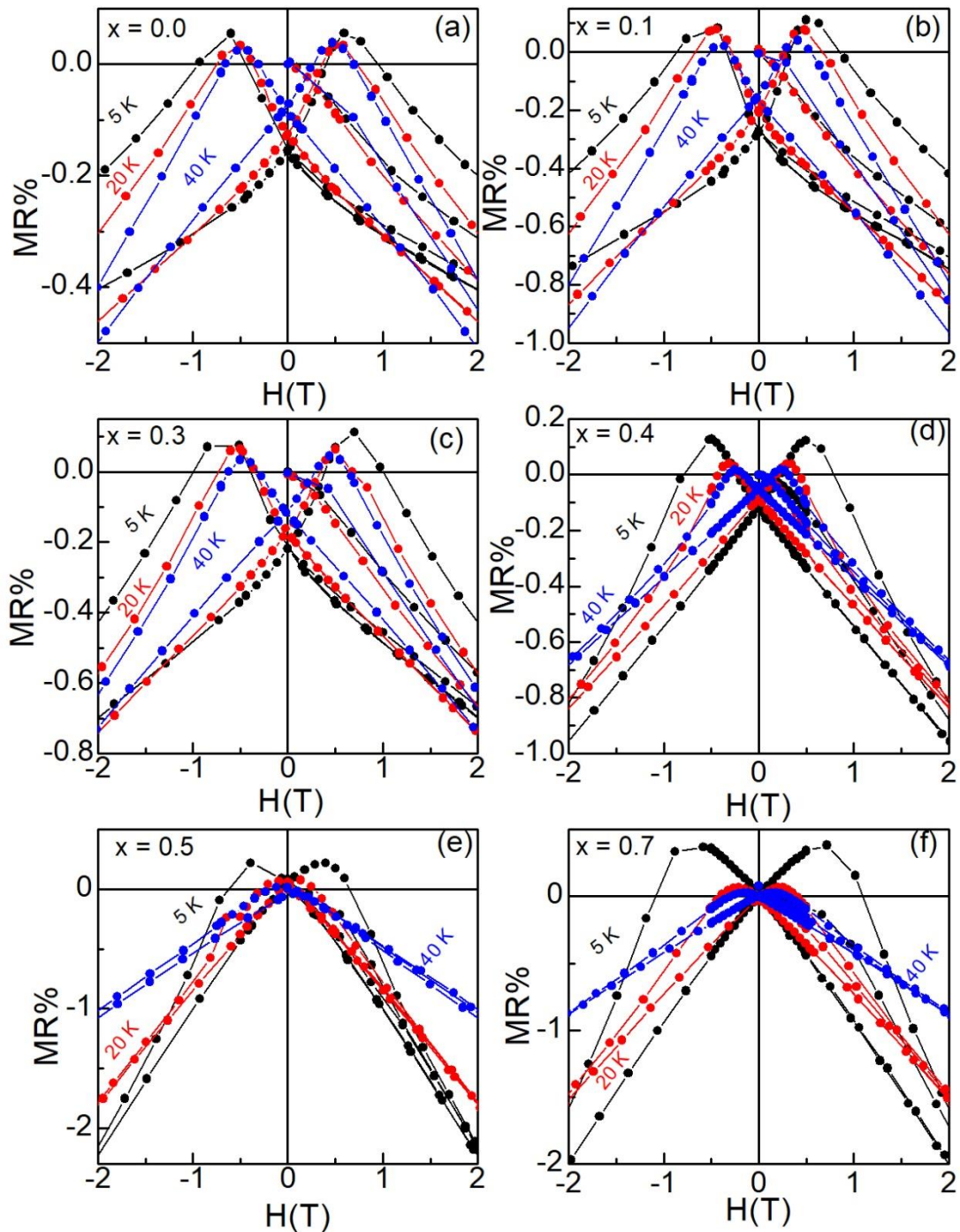


Figure 6.9 The MR at 5 K, 20 K and 40 K of $\text{SrRu}_{1-x}\text{Ti}_x\text{O}_3$ series with (a) $x = 0.0$, (b) $x = 0.1$, (c) $x = 0.3$, (d) $x = 0.4$, (e) $x = 0.5$ and (f) $x = 0.7$.

We have observed a maximum MR at 8 T for $x = 0.5$ as shown in figure 6.7 (c). The maximum MR at $x = 0.5$ may be related to the MIT in this series around $x = 0.4$ (Figure 6.2). For SrRuO_3 , we observe positive MR of amount $\sim 0.05\%$ at 0.5977 T which shows symmetric nature and remanent negative MR at zero field is around 0.1553% with large area of hysteresis. By Ti doping, the positive value of MR increases and maximum positive MR value is 0.33% at 0.88 T for $x = 0.7$. The remanent MR decreases with Ti doping and $x = 0.5$ and 0.7; the remanent MR become invisible. The cohesive field appears below 1 T.

To study the evolution of MR at different temperature has been recorded for $\text{SrRu}_{1-x}\text{Ti}_x\text{O}_3$ series, at 5 K, 20 K and 40 K as shown in figure 6.9 (a–f). In all the samples, we observed that remnant MR and coercive field decreases with increasing temperature, however, this decrement is very small for $x = 0.0 - 0.3$ and prominent decrease is observed for $x = 0.4$. MR behavior with temperature is intriguing.

6.3.6 Specific Heat

The specific heat is widely used experimental tool to understand the thermoelectric properties in a material, particularly across the phase transition. In figure 6.10 (a) we have presented the temperature dependence specific heat for two representative samples with $x = 0$ and 0.2. It is clear in figure 6.10, that at low temperature $C_p(T)$ shows saturation till around 20 K however above this temperature $C_p(T)$ increases almost linearly. Interestingly, for $x = 0$ parent compound $C_p(T)$ exhibits a jump around T_c which is shown as a magnified view in upper inset of figure 6.10 (a). For doped $x = 0.2$ compounds, $C_p(T)$ does not exhibit any jump across T_c however, the data show a change in a slope across T_c . This implies with Ti substitution magnetic phase transition has been broadened. Similar signature of broadening of magnetic transition has also been observed in temperature dependence magnetization data which has been shown in lower inset of figure 6.10 (a). Here it can be mentioned that similar broadening in C_p data has been observed in other doped material in present $\text{SrRu}_{1-x}\text{Ti}_x\text{O}_3$ series. The specific heat has

mainly two contributions namely, electronic and lattice contribution. The temperature dependence specific heat can be expressed with the following functional form.

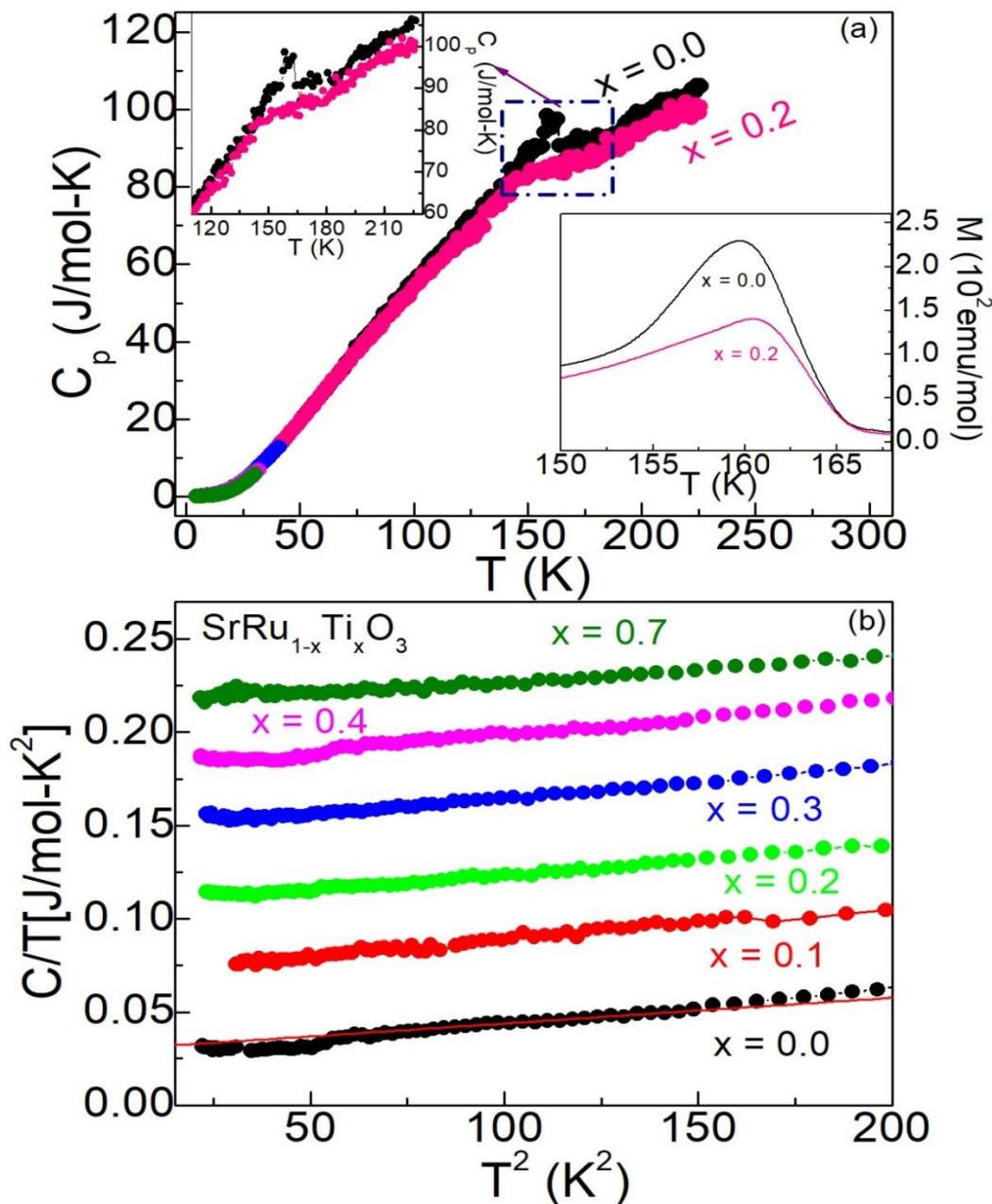


Figure 6.10 (a) The temperature dependent specific heat $C_p(T)$ of $\text{SrRu}_{1-x}\text{Ti}_x\text{O}_3$ series with $x = 0.0$ and 0.2 , and the upper and lower inset shows zoomed view of $C_p(T)$ and $M(T)$. (b) The straight line fitting of $C_p(T)$ in the form of equation (6.9) for $x = 0.0, 0.1, 0.2, 0.3, 0.4$ and 0.7 of $\text{SrRu}_{1-x}\text{Ti}_x\text{O}_3$ series. For clarity, the $C_p(T)/T$ data has been shifted by the rate of amount 0.02 upside for $x = 0.1, 0.2, 0.3, 0.4$, and 0.7 of $\text{SrRu}_{1-x}\text{Ti}_x\text{O}_3$ series.

$$C_p = \gamma T + \beta T^3 \quad (6.8)$$

where γ and β are the electronic (C_e) and lattice coefficients (phonon contribution, C_l) respectively.

To identify the individual contribution of electronic and lattice part, the specific heat data has been plotted as C/T versus T^2 , as following

$$C_p/T = \gamma + \beta T^2 \quad (6.9)$$

The $C_p(T)$ data has been plotted following equation 6.8 as shown in figure 6.10 (b). From the straight line fitting, the intercept and slope will give gamma and beta respectively. The fitting of equation 6.9, gives $\gamma = 30 \text{ mJ mol}^{-1} \text{ K}^{-2}$ and $\beta = 0.138 \text{ mJ mol}^{-1} \text{ K}^{-4}$ for parent compound SrRuO₃, where the values closely match with the reported value for this material [22]. This high value of γ also suggests that there is strong electronic correlation in SrRuO₃. The γ and β provides vital information of material for instance; the electronic coefficient gamma is directly related to density of states (DOS) following

$$\gamma = \frac{1}{3} \pi^2 k_B^2 N D(E_F) \quad (6.10)$$

Similarly, the lattice contribution β gives Debye temperature (θ_D) of material following equation 6.11

$$\theta_D = \left[\frac{12 \pi^4 n R}{5 \beta} \right]^{1/3} \quad (6.11)$$

where $R = 8.314 \text{ J K}^{-1} \text{ mol}^{-1}$ is the universal molar gas constant and $n = 5$ (for SrRuO₃) is the number of atoms per formula unit (f.u.).

The γ estimated using equation 6.10 has been shown in figure 6.11 (a), which shows γ continuously decreases with progressive doping of Ti. This implies that corresponding DOS also decreases as we dope Ti in SrRuO₃. The decrease in DOS is also reflected in an increase in resistivity with x in SrRu_{1-x}Ti_xO₃ series as shown in figure 6.2 a similar decrease of DOS with Ti doping has also been shown using XPS measurements [26]. Decreasing γ implies that DOS decreases with x . Using equation 6.11 we have calculated Debye temperature (θ_D) from estimated 413 K.

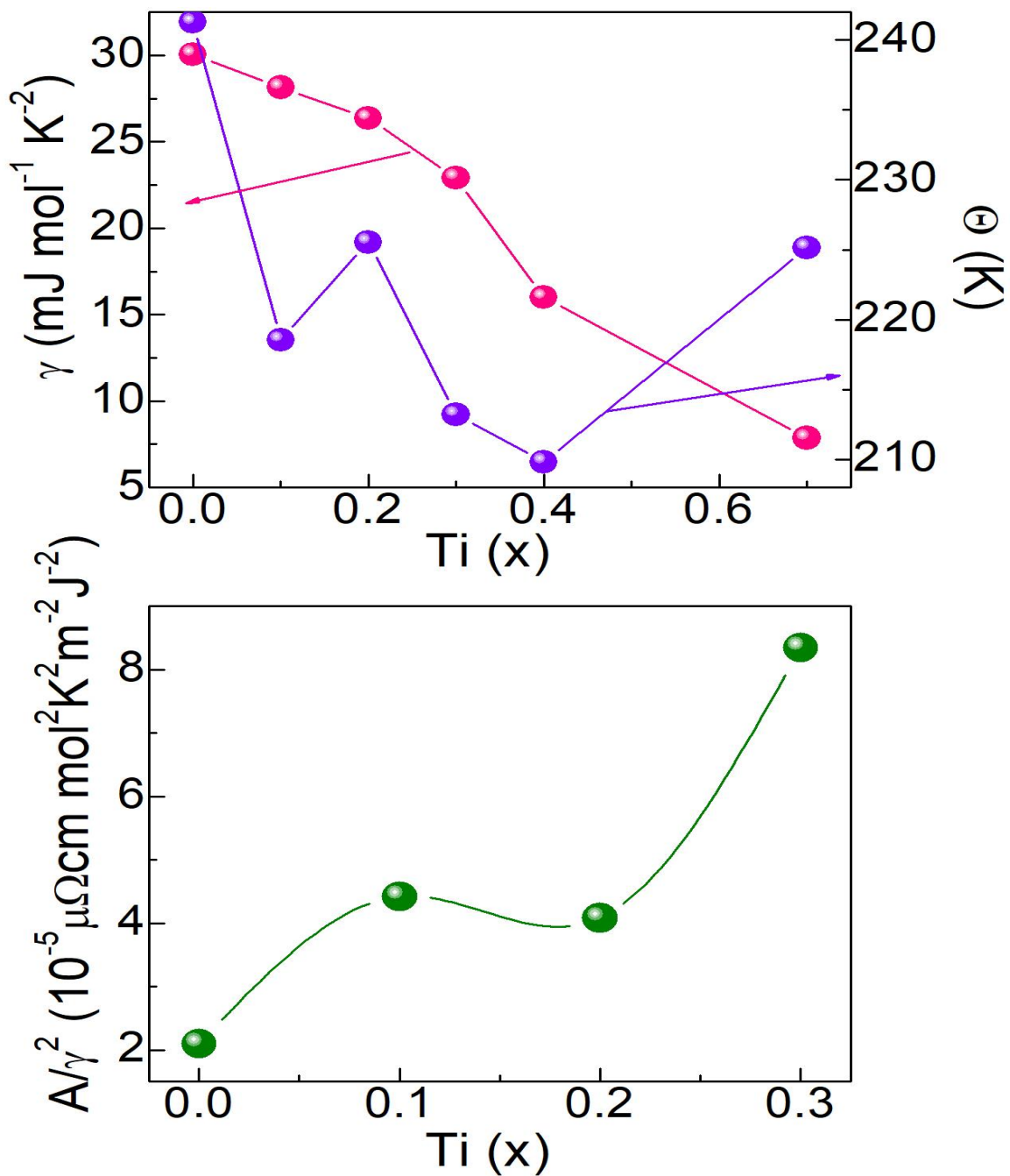


Figure 6.11 The electronic specific heat coefficient (γ) on left axis and right axis shows Debye temperature (Θ_D) with the variation of Ti substitution in $\text{SrRu}_{1-x}\text{Ti}_x\text{O}_3$ series (b) The Kadowaki-Woods ratio with the variation of Ti substitution in $\text{SrRu}_{1-x}\text{Ti}_x\text{O}_3$ series.

6.3.7 Kadowaki Woods Ratio (KWR)

The Kadowaki-Woods ratio ($KWR = R_{KW} = A/\gamma^2$) is the comparison of Fermi liquid (FL) coefficient (A) and specific heat electronic coefficient (γ). This ratio has found to be constant or near in constant range for any transition metal compounds and or heavy fermion compounds [27]. Here for SrRuO₃, we found the FL coefficient at 0 T of magnetic field $1.89 \times 10^{-5} \text{ m}\Omega \text{ cm K}^{-2}$ and electronic coefficient is $\gamma = 30 \text{ mJ mol}^{-1} \text{ K}^{-2}$ so the KWR would be $2 \times 10^{-5} \mu\Omega \text{ cm mol}^2 \text{ K}^2 \text{ m}^{-2} \text{ J}^{-2}$ which is good agreement for other d electron system [28, 29]. The comparison of value KW ratio of SrRuO₃ to the heavy-fermions (f electron) system we found that SrRuO₃ is two times larger than f electron system which shows strong electron correlation effect present in the system.

Figure 6.11 (b) shows the variation of KW ratio with Ti doping which shows almost linear increasing behavior also reveals that electron correlation effect increases. However here we point out that the FL coefficient does not show at low temperature, but as the temperature increase, this behavior comes so in this condition the validity of KWR analysis is questionable.

6.4 Conclusion

The SrRuO₃ shows metallic behavior throughout the temperature range and shows correlation with magnetization at T_c . The electrical resistivity of SrRu_{1-x}Ti_xO₃ series increases by Ti substitution and around $x = 0.4$ shows MIT and further insulating behavior increases by higher Ti substitution up to $x = 0.7$. The electrical resistivity in PM disorder state shows linear fitting with modified equation of Mott VRH for all series of samples. In FM metallic region, the FL and NFL behavior has observed in different temperature range. At low temperature, Kondo like behavior found for up to $x < 0.4$. The MR shows linear increasing behavior with increasing field in FM region while in PM region shows linear behavior in terms of quadratic field. The low temperature MR shows hysteresis which decreases by Ti substitution. Similar to magnetization, the electronic specific heat shows broadening of peak at T_c by Ti substitution. The DOS and Debye temperature shows decreasing and increasing value by Ti substitution respectively. The KWR shows electron correlation effect increases by Ti substitution.

Bibliography

- [1]. P. B. Allen, H. Berger, O. Chauvet, L. Forro, T. Jarlborg, A. Junod, B. Revaz, G. Santi, *Phys. Rev. B*, **53** 4393 (1996).
- [2]. K. Yoshimura, T. Imai, T. Kiyama, K. R. Thurber, A. W. Hunt, and K. Kosuge, *Phys. Rev. Lett.* **83**, 4397 (1999).
- [3]. L. Klein, J. S. Dodge, C. H. Ahn, G. J. Snyder, T. H. Geballe, M. R. Beasley, and A. Kapitulnik, *Phys. Rev. Lett.* **77**, 2774 (1996).
- [4]. G. Cao, S. McCall, M. Shepard, J. E. Crow, and R. P. Guertin, *Phys. Rev. B* **56**, 321 (1997); G. Cao, S. McCall, J. Bolivar, M. Shepard, F. Freibert, P. Henning, J. E. Crow, and T. Yuen, *ibid.* **54**, 15144 (1996).
- [5]. I. I. Mazin and D. J. Singh, *Phys. Rev. B* **56**, 2556 (1997).
- [6]. J. S. Dodge, E. Kulatov, L. Klein, C. H. Ahn, J. W. Reiner, L. Mieville, T. H. Geballe, M. R. Beasley, A. Kapitulnik, H. Ohta, Y. Uspenskii, and S. Halilov, *Phys. Rev. B* **60**, R6987 (1999).
- [7]. J. M. Longo, P. M. Raccah, and J. B. Goodenough, *J. Appl. Phys.* **39**, 1327 (1968).
- [8]. P. T. Barton, R. Seshadri, and M. J. Rosseinsky, *Phys. Rev. B* **83**, 064417 (2011).
- [9]. M. Kim and B. I. Min, *Phys. Rev. B* **91**, 205116 (2015).
- [10]. M. Takizawa, D. Toyota, H. Wadati, A. Chikamatsu, H. Kumigashira, A. Fujimori, M. Oshima, Z. Fang, M. Lippmaa, M. Kawasaki and H. Koinuma, *Phys. Rev. B*, **72**, 060404 (2005).
- [11]. J. Kim, J. Y. Kim, B. G. Park and S. J. Oh Kim, *Physical Review B* **73**, 235109 (2006).

- [12]. Pao-An Lin, Horng-Tay Jeng and Chen-Shiung Hsue, *Phys. Rev. B*, **77**, 085118 (2008).
- [13]. R. Gupta and A. K. Pramanik, *J. Phys.: Condens. Matter*, **29**, 115801 (2017).
- [14]. K. W. Kim, J. S. Lee, T. W. Noh, S. R. Lee and K. Char, *Phys. Rev. B*, **71**, 125104 (2005).
- [15]. N. F. Mott, *Proc. Phys. Soc. London Sect. A* **62**, 416 (1949).
- [16]. N. F. Mott, *Metal-Insulator Transitions (Taylor and Francis, London, 1990)*.
- [17]. N. F. Mott and E. A. Davis, *Electronic Processes in Non-Crystalline Materials (Oxford University Press, Oxford, 1979)*.
- [18]. N. F. Mott, *Philos. Mag.* **19**, 835 (1969).
- [19]. G. N. Greaves, *J. Non-Cryst. Solids* **11**, 427 (1973).
- [20]. P. Kostic, Y. Okada, N. C. Collins, Z. Schlesinger, J. W. Reiner, L. Klein, A. Kapitulnik, T. H. Geballe, and M. R. Beasley, *Phys. Rev. Lett.* **81**, 2498 (1998).
- [21]. M. S. Laad and E. Müller-Hartmann, *Phys. Rev. Lett.*, **87**, 246402, 2001.
- [22]. G. Cao, S. McCall, M. Shepard, J. E. Crow and R. P. Guertin, *Phys. Rev. B*, **56**, 321 (1997).
- [23]. D. Fuchs, M. Wissinger, J. Schmalian, C. L. Huang, R. Fromknecht, R. Schneider and H. V. Lohneysen, *Phys. Rev. B*, **89**, 174405 (2014).
- [24]. A. P. Mackenzie, J. W. Reiner, A. W. Tyler, L. M. Galvin, S. R. Julian, M. R. Beasley, T. H. Geballe, and A. Kapitulnik, *Phys. Rev. B* **58**, R13318 (1998).
- [25]. C. Sow, D. Samal, and P. S. Anil Kumar, *J. Appl. Phys.*, **111**, 07E121 (2012).
- [26]. K. Maiti and R. S. Singh, *Phys. Rev. B*, **71**, 161102 (2005).
- [27]. K. Kadowaki and S.B. Woods, *Solid State Commun.* **58**, 507 (1986).
- [28]. R. Jin, J. He, S. McCall, C. S. Alexander, F. Drymiotis, and D. Mandrus, *Phys. Rev. B*, **64**, 180503(R).
- [29]. M. Schneider, D. Geiger, S. Esser, U. S. Pracht, C. Stingl, Y. Tokiwa, and V. Moshnyaga, *Phys. Rev. Lett.* **112**, 206403 (2014).

Chapter 7

Conclusion and future plan

The $4d$ based Ru has central behavior of electron correlation effect (U) and spin orbit coupling effect (SOC). By considering the above effect, we choose SrRuO_3 which shows itinerant ferromagnetic nature at T_c and is the rare example of $4d$ based oxides with highest ordered moment. The main intension of this thesis is to figure out the innovative physics of magnetic and transport behavior in SrRuO_3 by non-magnetic substitution. Here we sum up the whole thesis work, result and future scope.

7.1 Conclusions

In the whole conclusions of this thesis work is understand the nature of magnetism of SrRuO_3 by the non-magnetic substitution of $\text{Ti}^{4+}(3d^0)$ and $\text{Ga}^{3+}(3d^{10})$ by studying the magnetic and transport behavior. The whole results of the thesis contained in chapter from 3 to 6 have the amplifying the knowledge of present explanation of magnetic and electrical transport study of the infinite layered ruthenates.

SrRuO_3 has good metallic conductivity, chemical stability and easy epitaxial growth on various perovskite structures which attract for multilayer device application and technological application. After the discovery of superconductivity in ruthenium based layer perovskite structure Sr_2RuO_4 , the study of SrRuO_3 has come in interest. SrRuO_3 is the end member of ruthenium based ruddlesden popper series ($\text{Sr}_{n+1}\text{Ru}_n\text{O}_{3n+1}$,

where n is the number of corner sharing of RuO_6 octahedra layers which is separated by Sr–O layers) series of infinite layer. Due to extended nature of $4d$ than $3d$ it shows more hybridization and because of large crystal field effect come in low spin state (t_{2g}^4) which gives the effective spin $S = 1$. The low temperature ordered moment observed $1.4 \mu_B/\text{f.u}$ which is less than theoretical calculated value of $2 \mu_B$ by $\mu_H = gS\mu_B$, where $S = 1$, which has considered due to itinerant ferromagnetic (FM) nature.

Chapter 3 shows polycrystalline samples of $\text{SrRu}_{1-x}\text{Ti}_x\text{O}_3$ series with x up to 0.7 have been prepared to understand the effect of site dilution on structural and magnetic properties. The parent material SrRuO_3 crystallizes in orthorhombic- $Pbnm$ structure having GdFeO_3 type crystallographic distortion where RuO_6 octahedra exhibit both tilt and rotation. With progressive Ti substitution, structural symmetry is retained though evolution of structural parameters has been observed. Magnetic moment and Curie temperature (θ_p) are observed to decrease with this dilution work. However, long-range magnetic ordering temperature T_c remains unchanged which is understood from the opposite tuning of electron correlation effect and DOS with Ti substitution within model of itinerant magnetism. The estimated critical exponent β (0.48) shows nature of magnetism in SrRuO_3 is of mean-field type, and an increase of β with x has been ascribed to development of FM clusters with Ti substitution. Interestingly, similar to isovalent doped $\text{Sr}_{1-x}\text{Ca}_x\text{RuO}_3$, these materials exhibit Griffiths phase like behavior in higher doped samples which is again believed to arise from clustering effect above T_c and represents the local moment picture of magnetism in SrRuO_3 . Analysis of low temperature thermal demagnetization data is in favor of dual presence of itinerant and local moment in SrRuO_3 in conformity with recent theoretical calculation.

Chapter 4 studied the critical behavior in perovskite based $\text{SrRu}_{1-x}\text{Ti}_x\text{O}_3$ as a function of Ti substitution using the standard methods such as modified Arrott plot, Kouvel-Fisher plot and critical isotherm analysis. We have estimated critical exponents β , γ , and δ where β increases and both γ and δ decreases with Ti substitution. The transition temperature T_c , however, remains almost unchanged with site dilution by Ti doping. The estimated exponents do not match with the values of any universality classes known for

spin interaction models. Nonetheless, the exponents nicely obey the Widom relation as well as scaling behavior which attests to the fact that estimated exponents and T_c are consistent and accurate. The evolution of exponents of similar nature has been observed in isoelectronic doped $\text{Sr}_{1-x}\text{Ca}_x\text{RuO}_3$. This specific change of exponents is likely caused by disorders arising from magnetic clusters which originate due to site dilution with Ti substitution. The evolution of the Griffiths phase like behavior in present series as evidenced in our earlier study substantiates the formation of magnetic clusters and its influences on the magnetic behavior.

Chapter 5 discuss the polycrystalline samples of $\text{SrRu}_{1-x}\text{Ga}_x\text{O}_3$ series with compositions ($x = 0.0, 0.05, 0.1$ and 0.2) have been prepared by the solid-state reaction method. All samples show single phase orthorhombic structure of $Pbnm$ space group. The lattice parameters decrease by Ga substitution due to lower ionic radii of Ru^{5+} which is generated through of Ru^{4+} charge state of by Ga^{3+} doping. Both the dc magnetization decreases and the bifurcation between M_{ZFC} and M_{FC} magnetization decreases with Ga^{3+} substitution. The analysis of thermal demagnetization at low temperature shows coexistence of both itinerant and localized model of magnetization. The magnetic critical exponent (β) of SrRuO_3 close to T_c indicates a mean field type behavior where the value of β increases with Ga substitution. In high temperature region, χ^{-1} follows Curie-Weiss behavior and both the μ_{eff} and θ_p decreases with Ga doping, a GP like behavior is observed at higher doping concentration. A transition from metallic to insulating state is observed between $x = 0.05$ to 0.1 , while the charge transport behavior in high temperature PM region is explained by modified Mott VRH model but in FM state below T_c , the charge transport mechanism mainly follow FL behavior where the temperature range for FL behavior increases with Ga doping.

Chapter 6 present the metallic behavior of SrRuO_3 throughout the temperature range and shows correlation with magnetization at T_c . The electrical resistivity of $\text{SrRu}_{1-x}\text{Ti}_x\text{O}_3$ series increases by Ti substitution and around $x = 0.4$ shows MIT and further insulating behavior increases by higher Ti substitution upto $x = 0.7$. The electrical resistivity in PM disorder state shows linear fitting with modified equation of Mott VRH

for all series of samples. In FM metallic region, the FL and NFL behavior has observed in different temperature range. At low temperature, Kondo like behavior found for upto $x < 0.4$. The MR shows linear increasing behavior with increasing field in FM region while in PM region shows linear behavior in terms of quadratic field. The low temperature MR shows hysteresis which decreases by Ti substitution. Similar to magnetization, the electronic specific heat shows broadening of peak at T_c by Ti substitution. The DOS and Debye temperature shows decreasing and increasing value by Ti substitution respectively. The KWR shows electron correlation effect increases by Ti substitution.

7.2 Future plan

In the past few decades, the ruthenium based oxides have been studied and explored for their intermediate effect of electron correlation and spin-orbit coupling in many exotic properties such as p-wave superconductivity, colossal magnetoresistance, FM-PM phase transition, AFM insulator, anomalous Hall Effect and more have been observed in ruthenates. However, various theoretical predictions have already been seen with the comparable results of experimental studies. The recent theoretical prediction shows that Weyl fermions play a vital role in temperature dependent spin wave behavior in SrRuO₃. Our magnetic and transport behavior results also match with the theoretical predictions and experimental results.

However, many other predictions are yet to be observed and the research is on way so we can say that the understanding of ruthenates has to go beyond the limits. For further understanding of physical properties and understanding physics in ruthenates detailed experimental studies are needed such as neutron diffraction, muon spin rotation (μ SR), ac susceptibility. Following the above direction, we are aim to study the ruthenates further and other related phases by using local probing methods. We will also study the effect of other nonmagnetic dopants like Al³⁺/Zr⁴⁺ to understand the physical properties in SrRuO₃. Similar effect will also be taken to trivalent or monovalent substitution at Sr²⁺ site to manipulate the Ru valence state. Further, isoelectronic divalent

(Ca²⁺ or Ba²⁺) substitution can also be employed to observe the effect on the physical properties of ruthenates. Magnetic anisotropic is intrinsic property since it depends on crystal structure and its understanding is quite important since it will provide vital information about physical properties like magnetization, specific heat etc. To understand the anisotropic behavior of physical properties, single crystal is required so we are planning to grow single crystals. Further to understand how the physical properties can evolve with reducing dimension, thin films will be grown and nanoparticles will be prepared. Efforts will also be taken to grow the multilayer heterostructures of ARuO₃ and other ferromagnet or superconducting materials. Further, to explore our understanding and observe the variation between $3d$ to $5d$, we will also study the Ru based double perovskite (DP, A₂BB'O₆), where B and B' both are different TM and good point is that B and B' can be selectively choose. With this belief that this thesis work has significant contribution to the understanding in the physics of ruthenates, we conclude with an aim to understand and excel the physics of ruthenates in future.

Author's Profile

Renu Gupta

121- Low Temperature Lab

School of Physical Sciences

Jawaharlal Nehru University

New Delhi, India 110067

Email: renugpt21@gmail.com

Education

2012 **Pre. Ph. D Physical Sciences**

School of Physical Sciences

Jawaharlal Nehru University, New Delhi

2010 **M. Sc. Physics (Specialization: Electronics)**

(1st Division)

Dr. Ram Manohar Lohia Avadh University, Faizabad, Uttar Pradesh

Research Interest

- Transition metal oxides
- Ruthenium based perovskite structure
- Thin film
- Experimental condensed matter physics, Material synthesis & Structural analysis, Transition metal oxides, Magnetic phase transition, Electronic transport behavior.
- Nano materials.

Achievements and Awards

**December
2014**

**Junior Research Fellowship (JRF) physics with
AIR131**

Council for Scientific and Industrial Research –
University Grant Commission (CSIR–UGC)

- December 2014 Basic Scientific Research (BSR) fellowship**
By University Grant Commission (UGC)
- July 2012 Joint Entrance Screening Test (JEST) with AIR104**
- June 2012 CSIR- National Eligibility Test (NET) in physics**
with AIR50
- February 2012 Graduate Aptitude Test in Engineering (GATE)**
in physical sciences with AIR39

Poster and Oral Presentations

1. Workshop on Current Trends in Frustrated Magnetism, School of Physical Sciences, Jawaharlal Nehru University, New Delhi, India (09 – 13 February, 2015).
2. 8th India Singapore Symposium in Condensed Matter Physics, Indian Institute of Technology Kanpur, India (25- 27 February, 2015).
3. 60th DAE- Solid State Physics Symposium, Amity University, Noida, Uttar Pradesh, India (21 – 25 December, 2015).
4. Quantum Optics and Optics of Quantum Systems, School of Physical Sciences, Jawaharlal Nehru University, New Delhi, India (18 – 19 March, 2016).
5. Science Day 2016, Jawaharlal Nehru University, New Delhi, India, 26 February, 2016.
6. 61st DAE- Solid State Physics Symposium, KIIT University, Bhubaneswar, Odisha, India (26 – 30 December, 2016).
7. International Conference on magnetic materials and applications (ICMAGMA-2017), Hyderabad, India (01 -03 February, 2017).
8. SPS March Meeting 2017 on the Theme: Perspectives in Graphene and Graphene like 2D materials, Jawaharlal Nehru University, New Delhi, India (17 – 18 March, 2017).

9. 2nd International Conference on Condensed Matter and Applied Physics, Govt. Engineering College, Bikaner, Rajasthan, India (24-25, 2017, November).
10. International Workshop on Advanced Materials, National Institute of Science and Technology (NIST), Berhampur, Odisha, India (19 – 21 December, 2017).
11. Intermag2018, Marina Bay Sands Convention Center, Singapore (23rd to 27th April, 2018).

Workshops

1. Nanosceince & Condensed Matter Interface (March Meeting- 2013), School of Physical Sciences, Jawaharlal Nehru University, New Delhi-110067, India, 07-08 March, 2013.
2. Computational Material Science Workshop, School of Physical Sciences, Jawaharlal Nehru University, New Delhi-110067, India, 03 – 05 March, 2014.
3. Workshop on Physical Property Measurement System, Advanced Instrumentation Research Facility, Jawaharlal Nehru University, New Delhi-110067, India, 15-16 September, 2014.
4. Workshop on Current Trends in Frustrated Magnetism, School of Physical Sciences, Jawaharlal Nehru University, New Delhi, India (09 – 13 February, 2015).
5. 8th India Singapore Symposium in Condensed Matter Physics, Indian Institute of Technology Kanpur, India (25- 27 February, 2015).
6. International Workshop on Advanced Materials, National Institute of Science and Technology (NIST), Berhampur, Odisha, India (19 – 21 December, 2017).